EXPERIMENTAL STUDIES OF THE MECHANICAL BEHAVIOR OF A PVA DUAL-CROSSLINK HYDROGEL

A Dissertation

Presented to the Faculty of the Graduate School

of Cornell University

in Partial Fulfillment of the Requirements for the Degree of

Doctor of Philosophy

by

Mincong Liu

August, 2019

EXPERIMENTAL STUDIES OF THE MECHANICAL BEHAVIOR OF A PVA DUAL-CROSSLINK HYDROGEL

Mincong Liu, P.h.D

Cornell University 2019

This study aims to understand the mechanical behavior of a PVA dual-crosslink hydrogel using both experimental and theoretical tools, with more focus on the experimental aspects. This PVA hydrogel is crosslinked by both chemical (permanent) and physical (transient) crosslinks. The chemical crosslinks remain attached during loading while the physical crosslinks can break and reform, leading to the viscoelasticity. This material serves as a model system for understanding the behavior of such materials.

Firstly, we studied the effects of temperature and loading rates on the mechanical response of this material. The breaking and reforming rates of the physical crosslinks are sensitive to the temperature change. Both large strain uniaxial tension tests and small strain torsional rheometry tests were performed at different rates in a temperature range of 13 ^{o}C to 50 ^{o}C. The rheometry data show that time-temperature superposition can be used to condense the data to a master curve. It is found that by allowing the model parameters to be temperature dependent a previously developed constitutive model fits the tension and rheometry data well. Horizontal (time) and

vertical (amplitude) shift factors calculated directly from the rheometer test data and from tension test data agree well with each other, establishing the connection between the effects of temperature on different types of experiments.

Secondly, we developed a 2D digital image correlation (DIC) system to measure the deformation near the crack tip of a cracked specimen. Experimental details such as how to prepare a durable speckle pattern on a material that is 90% water are discussed. DIC is used to measure the strain field in tension loaded samples containing a central hole, a circular edge notch and a sharp crack. These experiments are modeled using the finite element method (FEM). Excellent agreement between FEM and DIC results for all three geometries suggests that the DIC measurements are accurate up to strains of over 10, even in the presence of very high strain gradients near a crack tip. The method is then applied to verify a theoretical prediction that the deformation field in a cracked sample under relaxation loading, i.e. constant applied boundary displacement, is stationary in time even as the stress relaxes by a factor of three. We further utilized DIC to study the crack propagation of this PVA gel. We show that the crack propagates in steady state. The moving crack induces a very high strain rate (10^{-1}) ahead of the moving crack tip, which leads to a high stress that causes the fracture of the material.

Thirdly, we developed a predictive fracture criterion for this material. We loaded the specimen with an edge crack to fracture under two loading conditions: constant applied stress (creep) and constant stretch rate. The stress fields near the crack tip

were simulated using finite element method (FEM) and a stress-intensity-factor-like crack tip parameter was obtained. Using this parameter in a kinetic fracture model in which the rate of bond breaking depends exponentially on the stress level, results from creep fracture tests are used to develop a fracture criterion that is then applied to predict failure under constant stretch rate loading.

BIOGRAPHICAL SKETCH

Mincong Liu was born in Dalian, a coastal city in Northeastern China. In 2008, after graduating from Dalian No.24 High School, he was admitted to Dalian University of Technology to pursue a bachelor's degree in Automotive Engineering. In 2012, He moved to Pittsburgh, PA for his master study and received the master degree in Mechanical Engineering from Carnegie Mellon University in 2013. In 2014, he began his Ph.D. study in the Department of Mechanical and Aerospace Engineering at Cornell University. His major concentration is Solid Mechanics & Materials.

To my families

ACKNOWLEDGEMENTS

This work would not have been possible without the help of many people.

First, I would like to thank my adviser, Prof. Alan Zehnder. I have been getting valuable guidance and support from him. He is a phenomenal adviser. He is able to convey the knowledge to me in a very effective way. He is always ready to help whenever I need. I remember the days he spent in the lab with me setting up experiments. And I also remember his prompt email response. His help makes my learning very efficient. He is also very nice in person. He gives me enough freedom for my research and always treats me with kindness.

I would also like to thank Prof. Chung-Yuen Hui and Prof. Derek Warner for serving as my special committee members. Prof. Hui and I worked closely on the hydrogel project. And we had a lot of inspiring discussions together, which are reflected in this work. I'm always inspired by his energy and passion in the research. Prof. Warner provided useful guidance for my minor in computational science and engineering, which I do benefit a lot.

Finally, I'd like to express my special gratitude to my families, including my parents, and my wife, Wenxiu. Their unconditional support is the best thing I could have ever had.

TABLE OF CONTENTS

CHAPTER 1

INTRODUCTION

A hydrogel is essentially a network of polymer chains swollen in water. Some hydrogels can exhibit desirable properties, such as high compliance, low friction and good compatibility with biological tissues. Those properties make hydrogels a good candidate for some biomedical engineering applications, such as cell scaffolds in tissue engineering [1] [2], as artificial cartilage [3] and as vehicles for drug delivery [4]. However, some applications require a good load-carrying capabilities, such as high stretchability and high toughness, which were not met by conventional hydrogels. Researchers have been able to overcome this limitation using different toughening mechanisms [5]. One of the toughening mechanisms is to build highly stretchable polymer network by introducing a non-organic component to the network. For example, Haraguchi et al. [6] prepared nanocomposite hydrogel by polymer intercalating into disk-shaped nanoclay sheets. The resulting gels exhibited high structural homogeneity, superior elongation with near-complete recovery. Another toughening mechanism is using the idea of double, interpenetrating polymer networks [7] [8]. One example is the tough

hydrogel developed by Gong et al.[7]. There are two types of networks in this gel. The first network is stiff and serves as a sacrificial network; it breaks under load and dissipates energy. The second network is highly extensible, which prevents the growth of macro cracks during loading. The toughness of this hydrogel can match that of synthetic rubber (approximately 10,000 J/m^2). A drawback of this type of hydrogel is that the damage in the sacrificial network is irreversible. Damage accumulates after cycles of loading, leading to a lower fatigue resistance. To overcome this, researchers have introduced non-covalent, transient crosslinks in the sacrificial network [9] [10] [11]. These transient bonds can break and reform. Upon unloading and resting, some or all of the broken transient bonds can self-heal. As a result, this type of hydrogel is able to sustain large deformation and partially or fully recover to its original state after unloading. For example, J. Sun et al. [10] synthesized tough hydrogels by mixing ionically crosslinked alginate and covalently crosslinked polyacrylamide. The covalent crosslinks preserve the memory of the initial state, allowing the material to recover upon removal of the load. The ionic crosslinks unzip, causing internal hysteresis, dissipating energy, but they heal by re-zipping. The resulting gel can be stretched 20 times their initial length, and have a fracture energy of about 9,000 J/m^2, despite its high water content of about 90%. T. Sun et al. [11] reported the synthesis of a tough polyampholytes (PA) hydrogel with only ionic bonds. The ionic bonds have a wide distribution of strength. The strong bonds serve as permanent crosslinks, imparting elasticity, whereas the weak bonds can break and re-form, dissipating energy. This

PA gel has a toughness of 9,000 J/m^2, 100% self-recovery and high fatigue resistance. Despite the ability to create highly extensible and tough hydrogels, the mechanical properties of such materials have not yet been well understood. In order to facilitate the practical application of those hydrogels, a thorough investigation of their mechanical behavior is required. Those materials often exhibit rate-dependent viscoelastic behavior. One important aspect is to establish the relation between the breaking-reforming bond kinetics at micro-level and the material's response at macro-level. Understanding this will provide insights into the material behavior at different conditions, such as different loading rates and temperatures. The failure mechanism of such gels needs further study still. One way to study this is in the scope of fracture mechanics. There are two major challenges when studying the fracture of hydrogels. Firstly, the existence of the complex viscoelastic behavior and large deformation makes it challenging to obtain the detailed stress distribution near the crack tip. Secondly, due to the high viscoelasticity, it is difficult to keep track of the energy flow in the system and determine the energy that drives the crack growth. This makes the energy release rate based fracture characterization problematic. As a result, there has not been an effective criterion to predict the failure of such materials.

The overall goal of this study is to understand the rate-dependent, large deformation mechanical response of such hydrogels, with more focus on the experimental aspects. The study is focused on a specific type of hydrogel, the poly(vinyl alcohol) (PVA) dual-crosslink hydrogel developed by Mayumi et al.[12]. This hydrogel

contains only one network, crosslinked by both covalent (permanent) and physical (transient) bonds. During the loading process, the covalent bonds remain attached while the physical bonds can break and reattach. Due to this breaking and reattaching process, this PVA gel shows rate-dependent behavior. Long et al. [13] and Guo et al. [14] were able to build a constitutive model that captures the kinetics of the physical crosslinks and to relate this to the material's response at macro-scale. This model is able to give a good prediction of the PVA gel's response in uniaxial tension [13] [14] and rheology tests [15]. A numerical scheme developed by Guo et al. [16] allows the application of this constitutive model in finite element (FE) to simulate tests with more complicated geometry and loading history. The accuracy of this numerical application has been checked by comparing the simulation results with experimental results [16] [17]. Both the constitutive model and the numerical scheme provide effective tools to further study this material.

This thesis is organized as follows. In Chapter 2, the details of the experimental methodology are provided, including material synthesis and the information of a custom-built tensile tester with load and temperature control. The effects of temperature on the mechanical response of the PVA gel is studied in Chapter 3. Temperature affects the breaking and healing kinetics of the transient crosslinks and thus the macro-scale material response. Since time dependent gels have only recently been introduced, there are few studies on the effects of temperature and loading rate on the mechanical behavior of these gels [18]. In the current study, both large strain

uniaxial tension tests and small strain torsional rheology tests are performed under different temperatures and different loading rates. It is shown that there's a connection between those two experiments which can be captured by the constitutive model. The work in this chapter is published in Journal of Rheology [19] .In Chapter 4, the details of the application of 2D digital image correlation (DIC) to the measurement of deformation of PVA hydrogel with high strain gradient is provided. DIC is a non-contact, optical deformation measurement tool. There has been an increasing interest in applying this technique to measure the deformation of soft materials such as gels [20] [21] [22] [23] [24] [25]. However, the quantitative accuracy of this method in measuring the high strain gradient in the existence of large deformation has not been well-established yet. In this study, the accuracy was established by comparing the DIC measurement with the FE simulation. After the accuracy has been established, DIC is utilized to measure the strain field near the crack tip and study the time dependence of deformation fields in a cracked sample during a stress relaxation test. This work is published in Experimental Mechanics [26]. In Chapter 5, we further utilize DIC to study the crack propagation of this PVA gel. The specimens are immersed in mineral during the test to keep hydration. Practical issues such as the durability of the speckle pattern in the oil and the possible optical distortion when imaging through the oil are discussed. The strain fields induced by a propagating crack are obtained. We show that the crack propagates in steady state. Although the strain level near a propagating crack is significantly lower compared to a static crack,

the strain rate is much higher (10 s^{-1}). This high strain rate leads to a high stress which drives the crack propagation. The fracture mechanics of this material is further discussed in Chapter 6. Although there have been a lot of studies on the fracture of hydrogels [27] [28] [29] [30] [31] [32] [33], there has not been an effective failure criterion for such materials. One major challenge is to obtain the stress field near crack the tip of such viscoelastic materials and relate the stress to the fracture of the material. In this study, finite element simulation is utilized to obtain the stress distribution near the crack tip. Then the crack tip stress is incorporated in a thermally activated, kinetic fracture model. This failure model is able to predict the onset of fracture of this material under both constant nominal stress tests and constant stretch rate tests. This work is published in Extreme Mechanics Letters [34].

CHAPTER 2

EXPERIMENTAL SETUP

2.1 Introduction

In this study, experimental tools were utilized to study the mechanical properties of PVA dual-crosslink hydrogel. The basic experimental setups are introduced in this chapter, including material preparation and the design of a custom-built tensile tester. These setups are the fundamentals for most of the studies presented in this thesis, although some adjustments were made for certain tests.

2.2 Material Preparation

The dual-crosslink poly(vinyl alcohol) (PVA) hydrogels were prepared by incorporating borate ions in a chemically cross-linked PVA gel. The original system was introduced by Mayumi et al. in [12]. The whole synthesis process is explained in details in the following paragraphs.

PVA solution

The PVA 16% solution was made by dissolving PVA powder in distilled water at a high temperature. The PVA powder used here was from Sigma-Aldrich (Mw 89,000-98,000, 98+% hydrolyzed, 341584-500G). The whole process was done in a water bath environment with active stirring. We first added ice to the water bath to achieve a low temperature ($< 5\ ^oC$). Mixing the PVA powder and water at a low temperature makes the PVA powder distribute evenly in the water. Then we heated the water bath to 90 ^oC, held the temperature and kept stirring for another 2 hours. After 2 hours stirring, we let the solution cool at room temperature.

Chemically crosslinked gel

The chemically crosslinked gel was made by crosslinking PVA using glutaraldehyde (GA) in a low-pH environment. The target concentration of the PVA is 12%. The molar ratio of GA crosslinker to PVA monomer is 1:500. The target pH is 1.7. To make 40 g of such solution, we need 30 g of PVA 16% solution, 0.872 g of GA 2.5% solution, 0.8 mL of hydrochloric acid (HCl) (1mol/L) and 8.328 g of distilled water. We first mixed PVA 16% solution with distilled water under active stirring. Then we added GA 2.5% solution to the feed and kept stirring. The GA 2.5% solution was always freshly made from GA 25% solution (Sigma-Aldrich, Grade II, G6257-10ML). After 10 minutes, we added HCl (1mol/L) to the solution and kept stirring for another 10 minutes. After the solution was mixed evenly, the solution was injected into a custom-built mold using a syringe. The mold was made by acrylic plates spaced by silicone rubber with acetate sheets between the rubber and acrylic sheets.

A schematic view of this mold is shown in Figure 2.1. We let the solution sit in the mold for 36 hours. A good seal of the mold is required. After 36 hours, the gel needed to be washed to neutral pH. We peeled the chemical gel from the mold and place the gel into a bottle with distilled water. Water was changed regularly during a 12-hour period. After washing, the chemically crosslinked gel was in a swollen state and was very brittle. Thus it was handled with care.

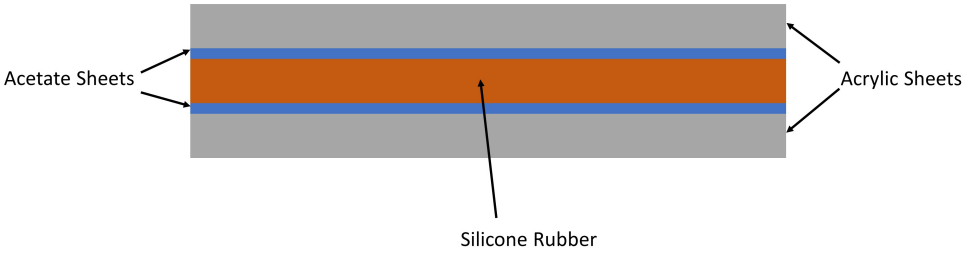

Figure 2.1: Acrylic mold used for shaping chemical gel

Physical crosslinking

After washing the chemically crosslinked gel, we soaked the gel in a fresh made Borax/NaCl solution in order to form the physical bonds and reduce the degree of swelling. The concentration of borax and NaCl in the solution was 1 mM/L and 90 mM/L respectively. Borax and NaCl used were from Sigma-Aldrich (Borax: Sodium tetraborate decahydrate, ACS reagent, $\geq$ 99.5%, S9640-500G; NaCl: Sodium chloride, puriss. pa., $\geq$ 99.5%, 71380-1 KG). To make the process consistent, for a swollen chemical gel of weight W, we soaked it in solution weighing 20W. The gel and solution were stored in a sealed plastic bottle for at least 3 days to reach equilibrium.

Specimen preparation

Small hydrogel specimen was cut from the as-prepared dual-crosslink hydrogel sheets using an X-ACTO knife. We used an aluminum plate of a fixed width to guide the cutting so that the width of the specimen is consistent from cut to cut. The width of the specimen was measured using a digital caliper. As the material is soft, it is challenging to accurately measure the thickness of the specimen with a caliper. To overcome this challenge, we utilized a custom-built measurement tool, as shown in Figure 2.2. We mounted a GAERTNER modular microscope on a Newport translational stage. Looking at the thickness of the specimen through the microscope, we first aligned the center of the microscope crosshair with one edge of the specimen. Then we moved the microscope with the translational stage until the crosshair center was aligned with the other edge. The displacement of the stage was thus equal to the thickness of the specimen.

2.3 Tensile Tester

Most of the experiments in this study were performed using a custom-built tensile tester, as shown in Figure 2.3. Details of the setup are explained in the following sections.

Translational motion

The translational motion was provided by a Zaber X-LSM200A-E03 translational stage. The stage was mounted on a Newport optical stand and connected to the

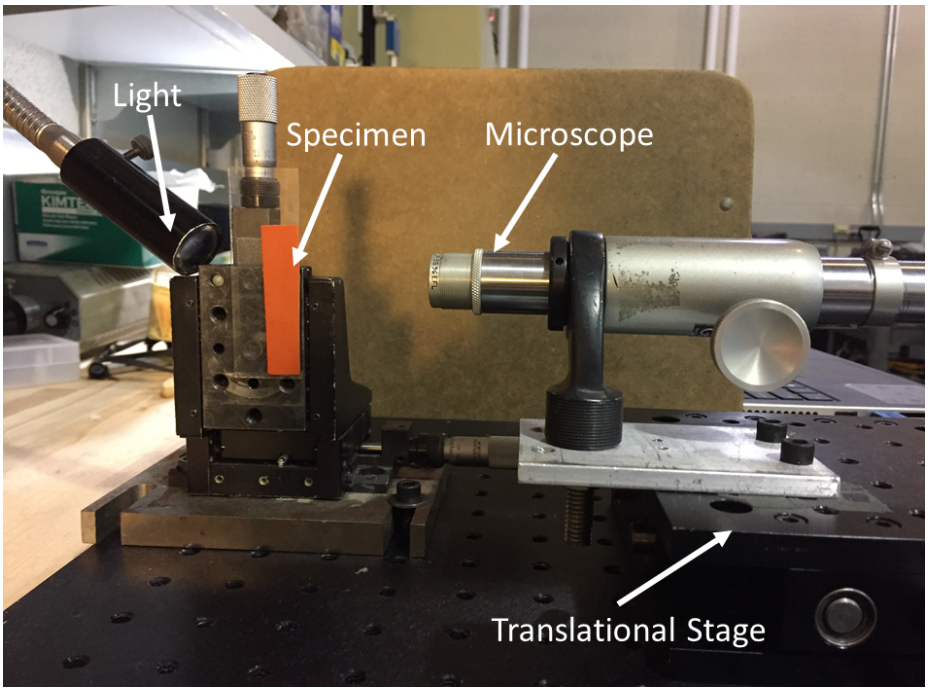

Figure 2.2: The tool to measure the thickness of the gel

hydrogel specimen via a load cell, an aluminum rod and aluminum grips, as shown in Figure 2.3. The stage was controlled by Zaber Console Software.

Gripping

The hydrogel samples were held by two aluminum grips. On each individual grip, the hydrogel specimen was held by two parallel aluminum plates. The two plates were connected by two screws. Sandpaper sheets were glued on both of the plates to prevent the slippage of the specimen. Figure 2.4 is a close-up view of the grip. Because the gel is soft and brittle, the screw should not be tightened too much. However, enough pressure is required in order to prevent the specimen from slipping. A certain amount of trial and error is required in order to apply the appropriate amount of pressure.

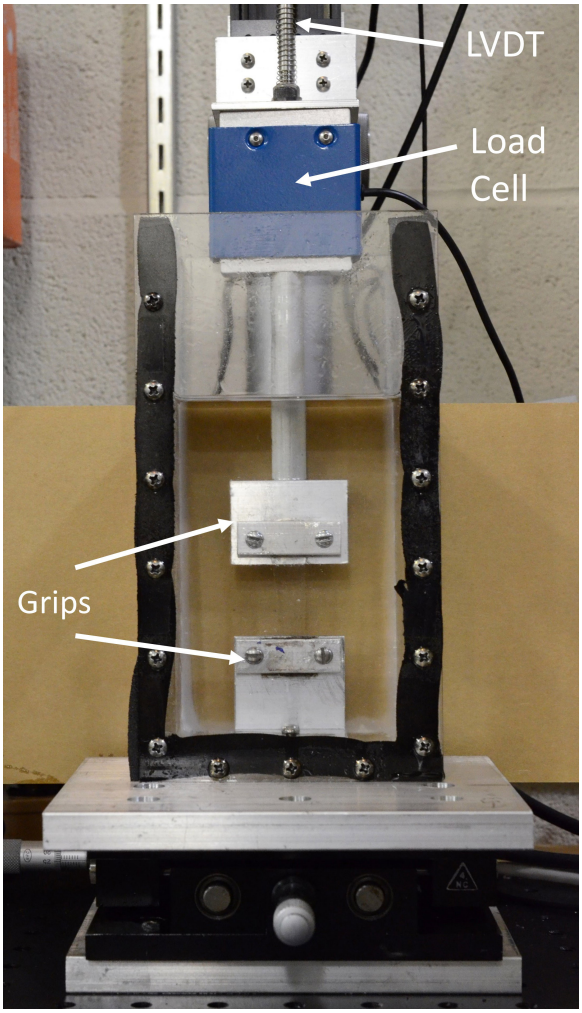

Figure 2.3: Custom-built tensile tester

Oil container

For most experiments, the hydrogel specimen was immersed in mineral oil to prevent drying. The oil was contained in a custom-built oil container made by acrylic plates. The container has a removable front door so that we can mount the specimen before filling the container with oil. The door is attached to the container using screws, with rubber foam placed between the door and the body of the container to improve sealing. It should be noticed that the oil exerts a buoyant force on the grips and this

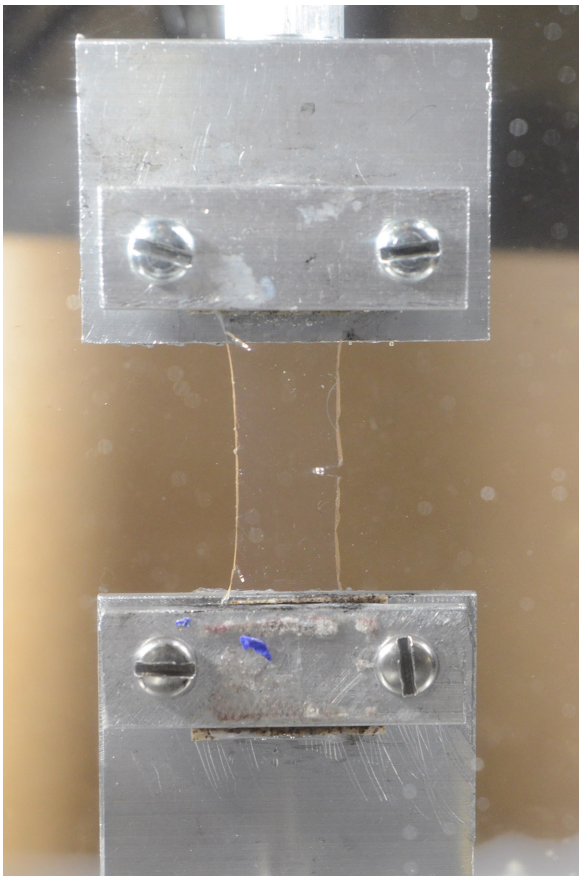

Figure 2.4: A close-up view of grips and the specimen

force needs to be subtracted from the measured load. Details will be discussed in the data processing section.

Data collection

The force signal was measured by an Interface SMT 1-1.1 load cell (1.1 lbf capacity). The force signal was passed to a CALEX 163MK signal conditioner where the signal was amplified and filtered, and then to a Keithley Model 2701 data logger. The load cell was calibrated by hanging dead weights (from 0 g to 20 g, which is consistent with the applied load range in the experiment) on the grips, recording the corresponding

force data and then performing a linear fitting on the data. The slope was obtained as the conversion factor to convert voltage into force (unit: N/V). Then the force can be determined just by multiplying the voltage by the conversion factor. We used the maximum possible gain setting of the signal conditioner and the corresponding conversion factor was 0.499 N/V. We performed the calibration every one or two months and the conversion factor remained constant. The displacement was measured using an OMEGA LD 620 LVDT. The LVDT was pre-calibrated, with a conversion factor 20 mm/V. We calibrated the LVDT under our set up and obtained a conversion factor of 19.9 mm/V, which is quite consistent with the factory calibration. The signal of the LVDT was passed directly to the data logger. When sampling data at two channels, the Keithley data logger can record data at a maximum speed of 25 data pairs/ second. The connection of load cell, LVDT and data logger was shown schematically in Figure 2.5.

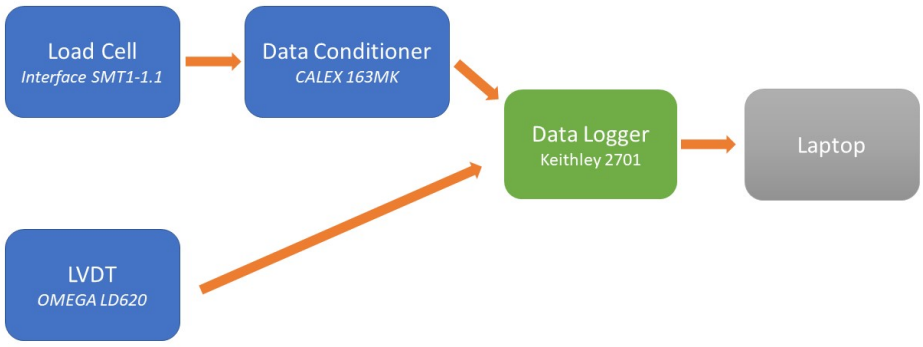

Figure 2.5: Connection of the data collection devices

Data processing

We interacted with the Keithley data logger via Kickstart software [35] on a Windows PC. For a typical tension test, we recorded the time, force signal from the load cell and the displacement signal from the LVDT. The data were written to a .txt file along with the sample dimensions. We wrote a MATLAB code to convert the force vs. displacement data to stress vs. stretch data. Here we define the nominal stress σ as force F divided by original area A_0, $\sigma = F/A_0$, stretch λ as one plus displacement u divided gauge length (the initial length between two grips before loading, L_0), $\lambda = 1 + u/L_0$. As mentioned in the early section, the buoyant force of the oil needs to be calibrated. We did this by immersing the top grip in oil, translating it without the specimen and recording the corresponding force vs. displacement signals. We noticed that the force signal always varies linearly with the displacement, as shown in Figure 2.6. We did a linear fitting on the data and define the slope of the fitted line as the calibration factor k (unit:V/mm). Then we obtained the calibrated force signal V_c using the following formula:

$$V_c = V_m - ku \tag{2.1}$$

Here V_m is the force signal directly from the load cell in Volt, u is the displacement in mm. The oil calibration factor k depends on the load cell and the dimension of the rod connecting the load cell and the grips. For the 0.5 inch diameter aluminum rod we used with the SMT 1-1.1 load cell, the calibration factor k was 0.0023 V/mm.

After getting the calibration factor, we converted force to stress using this calibrated force data.

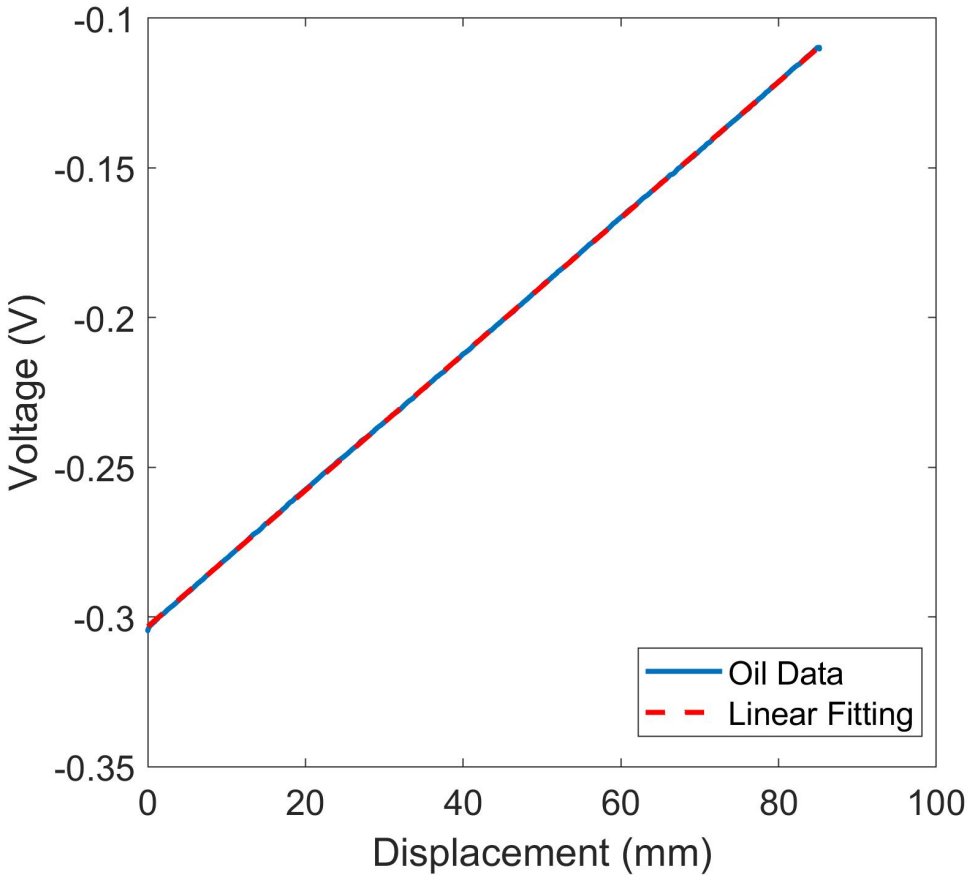

Figure 2.6: Oil calibration data and linear fitting

2.4 Feedback Load Control

The previous setup was only able to achieve a open-loop control: the translational stage controls the motion of the top grip, which stretches the specimen and thus induces force within the specimen. A closed-loop force control scheme is required for

certain experiments, such as creep tests, when the hydrogel specimen is subject to a constant applied force. In order to achieve this, a PID control scheme was developed using MATLAB. For every discrete time step, the current force signal $V_{current}$ is read from the Keithley data logger into MATLAB. Then that signal is compared to the target force signal V_{target}. The difference $V_{current} - V_{target}$ is incorporated in a PID algorithm to compute a velocity correction term. Then the this velocity correction term is sent to the Zaber translational stage and the loading rate is adjusted. As the material is rate dependent, adjusting the loading rate will also change the induced force. A pseudo code of this control scheme is provided in Algorithm 1.

Some trial and error are necessary when determining the control parameters K_P,K_I and K_D. With the current setup, we found that we were able to get a good force control with K_P = 1,500,000, K_I = 5,000 and $K_D = 0$. The control system was able to ramp up the load to the target value within 10 seconds and the load was then held within $\pm$ 0.2% of the target load.

2.5 Temperature Control

To perform experiments under different temperatures, we built a temperature-control system as an add-on to our original tensile tester. The system is shown schematically in Figure 2.7. The details are discussed in the following sections.

set target force signal V_{target}
set PID parameters K_P, K_I,K_D
error(1) = 0, errorIntegral = 0, currentTime(1) = 0
for *i = 2: n* **do**
  currentTime(i) = readCurrentTime()
  dt = currentTime(i) - currentTime(i-1)
  $V_{current}$(i) = readForceSignal()
  error(i) = V_{target} - $V_{current}$(i)
  % Compute velocity correction using PID
  duP = Kp * error(i)
  errorIntegral = errorIntegral + 0.5 * (error(i) + error(i-1))*dt
  duI = K_I * errorIntegral
  errorDifferential = (error(i)-error(i-1))/dt
  duD = K_D * errorDifferential
  du = duP + duI + duD
  % Adust Zaber speed based on du, and also set a upper and bottom limit for du
  if *abs(du) > 2 mm/s* **then**
    du = du/(abs(du)) * 2mm/s ;
  else if *abs(error(i)) / V_{target} < 0.01* **then**
    du = 0.001mm/s ;
  setZaberSpeed(du)
end

Algorithm 1: A pseudo code for PID force control scheme

2.5.1 Equipment Setup

Heating

We used two low-power (total power of 15 Watts) flexible immersible heaters to heat the oil in order to keep the oil at a certain elevated temperature. An external power source of 15 V provides the power of the heaters and the heaters were connected to an Arduino UNO board which controls the ON/OFF of them based on the current temperature of the oil. This temperature was measured by an immersible digital thermometer (Dallas Semiconductor DS18B20). The details of the temperature control

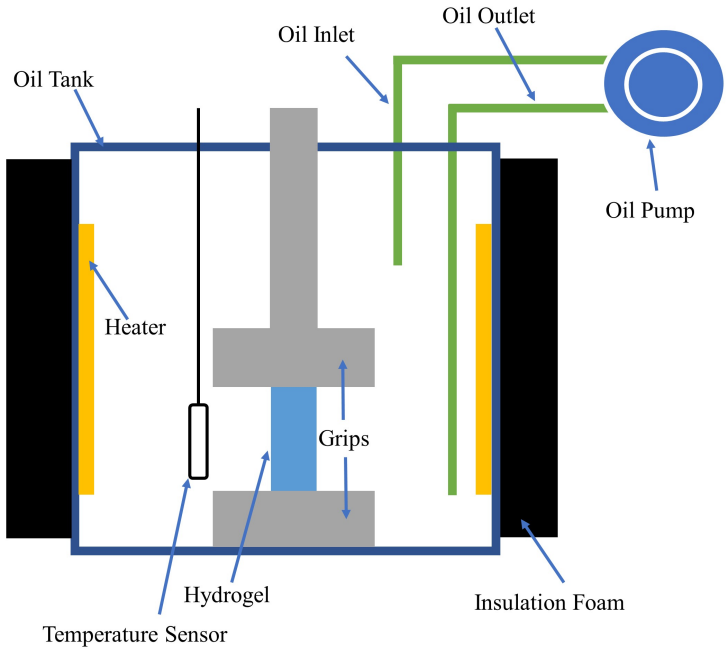

Figure 2.7: Schematic view of the temperature control system

method will be discussed in later sections.

Thermal insulation

In order to reduce the heat loss of the system, we insulated the system by gluing insulation foam (K-Flex 6RSX3X4048) to the outer surfaces of the acrylic oil container.

Oil circulation

We noticed that if we did not stir the oil, there was some variation in oil temperature in the vertical direction. The temperature difference between the top and the bottom of the specimen could be as large as 3 ^{o}C. To reduce the temperature difference, we implemented an oil circulation system. The oil was circulated using a peristaltic pump driven by a 12V DC motor. The pump extracted the oil from the top of

the tank (warmer side) and then injected the oil to the bottom of the tank (cooler side). The oil was circulated at a rate of 100 mL/min. By using this oil circulation system, we verified that the temperature difference between the top and bottom of the specimen was less than 1 ^{o}C. The circulation does not cause any significant noise to the measured load signal.

2.5.2 Temperature Control Method

The temperature was controlled by turning the heaters ON/OFF based on the current temperature of the oil. The control was achieved by the an Arduino UNO board. For a target temperature T, we programmed the Arduino controller so that if the temperature was below T + 0.1 ^{o}C, the heater would turn on. If the temperature was above T + 0.3 ^{o}C, the heater would turn off. Using this method, we were able to hold the temperature within to $\pm$ 0.5 ^{o}C of the target temperature T.

CHAPTER 3

TIME-TEMPERATURE EFFECTS ON THE MATERIAL RESPONSE

3.1 Introduction

For hydrogels with transient physical crosslinks, temperature can have significant effects on the mechanical response. Varying the temperature changes the breaking and reattaching rates of the physical crosslinks, which is equivalent to varying the loading rates. Understanding the effects of time and temperature on the mechanical response will facilitate the practical application of such materials under different environments. Since the time-dependent gels have only recently been introduced, there are few studies on the effects of temperature and loading rate on the mechanical behavior of these gels. Recently, Sun et al. [18] showed that it was possible to use vertical and horizontal shift factors to collapse small strain rheology data onto a master curve for polyampholyte hydrogels. Further, they measured the hysteresis from uniaxial cyclic tests carried out at moderately large strains. They found that

the hysteresis from tests with different stretch rates and temperatures can be collapsed onto a master curve using the same shift factors obtained from the rheology.

In this work, we studied the effects of temperature on the mechanical response of the PVA dual-crosslink hydrogel. We studied the quantitative relation between varying temperatures and changing loading rates. For many polymers, the relation between strain rates and temperature is found to obey the time-temperature superposition principle (TTS). Based on a constitutive model developed by Guo et al. [14], the material parameters at different temperatures can be obtained by fitting the model prediction to the experimental results. Analyzing those material parameters provides quantitative understanding of the temperature effects and the inherent relation between the material response during uniaxial tension tests and torsional rheology tests.

3.2 Experiment Overview

3.2.1 Uniaxial Tension Tests

We performed uniaxial tension tests on the hydrogel specimens at different loading rates and different temperatures. The tests were performed using a custom built tensile tester with a temperature control system. The details of the experimental setup can be found in Chapter 2.

We performed uniaxial tension tests on hydrogel specimens at five different temper-

atures, 13 ^{o}C, 22.5 ^{o}C (defined as room temperature), 30 ^{o}C, 40 ^{o}C and 50 ^{o}C. For temperatures above room temperature, we pre-heated the oil and then poured the warm oil into the oil tank. This would save a large amount of time for oil heating, as the heaters in our temperature control system had a relatively low power (15W). We've verified that the temperature could be held within $\pm 0.5^o$C of the target temperature using our temperature control system. For the tests below room temperature, we first cooled the oil below the target test temperature in a refrigerator and then filled the tank with the cooled oil. We started the test after the temperature of the oil reached the target value. As the test progressed, additional cool oil slightly below the test temperature was added to the oil tank so that the temperature could be held closely to the target temperature. We have verified that using this method, the temperature variation during a 30 minute test did not exceed 2 ^{o}C. It should be noted that for most tests, the testing time was much shorter. So the effects of the variance of temperature on the experimental accuracy should be minimal.

The specimens in the tests were 12 mm in width, 2 mm in thickness and 24 mm in gauge length. At each temperature, we loaded the specimens to a stretch ratio λ of 1.3 at five different stretch rates: 0.001/s, 0.003/s, 0.01/s, 0.03/s and 0.1/s (except for 13 ^{o}C where we tested at four loading rates excluding 0.003/s). The unloading rate for all the tests was 0.01/s. We also performed stress relaxation tests on these specimens at each temperature. In the stress relaxation tests, we loaded the specimen to a stretch ratio of 1.3 at a loading rate of 0.5/s and then held the stretch constant

for 30 minutes. The stress response over time was recorded. We repeated the tests twice at each temperature to check the consistency of the results.

At an elevated temperature, the hydrogel specimen might lose water even if it is immersed in the oil during the experiment. We performed several experiments to check this effect. The experiment was performed at 50 ^{o}C. We first loaded the specimen to a stretch ratio of 1.3 at 0.01/s (test A). Then we performed a series of uniaxial tension tests at other loading rates. The whole process was about one hour. After those tests, we loaded the same specimen to a stretch ratio of 1.3 at 0.01/s again (test B). We compared the stress vs. stretch data of test A and test B. The difference between the stress at a given stretch ratio for both test A and B was smaller than 5%. Since 50 ^{o}C was the highest temperature in the tests, for other temperatures, the effects of water loss should be even smaller. Thus it can be concluded that the effects of water loss should not be significant. The corresponding stress variance due to the water loss should be within 5%.

3.2.2 Small Strain Rheology

We performed small strain rheology tests using a TA Instruments DHR3 torsional rheometer with parallel plates. Hydrogel sheets with a thickness of 2.1 mm were cut into 20 mm diameter circular specimens using a stainless-steel punch. To eliminate slip between the specimen and the parallel plates, we applied pre-compression by setting the gap between the parallel plates to 1.6 mm. The circular specimens were

cyclically loaded to 0.3 % strain at frequencies from 0.01 Hz to 10 Hz. Three data points were taken per decade of frequency. As in the cyclic tension tests, these rheology tests were performed at 13^{o}C, 22.5^{o}C, 30^{o}C, 40^{o}C and 50^{o}C. These tests were repeated three times to check consistency. To reduce drying of the gel at elevated temperatures, we used a solvent trap to achieve a high-humidity environment. The trap holds the specimen in a small, closed space at close to 100 % relative humidity (RH) during the tests. In order to check the water loss due to elevated temperature, the specimens were weighed before and after the tests. We found that even for the 50 ^{o}C tests, the maximum weight loss was only about 5%.

For the small strain rheology tests, there are two possible issues that might have effects on the experimental accuracy. The first is specimen slippage. As mentioned before, a pre-compression was applied to the specimen in order to prevent the slippage. To demonstrate that slippage was prevented by pre-compression, we plot the axial force measured by the rheometer during the experiments, as shown in Figure 3.1. From Figure 3.1, it can be seen that at a certain temperature, the axial force did not vary significantly at different frequencies. This is a good indicator that there was no significant specimen slippage here. Further attention is needed if the axial force varies significantly with frequency at a given temperature. The other issue is the shear angle exceeding the limit of linearity. To test the limit of linearity, we performed an amplitude sweep, where we loaded the specimen at a fixed frequency, 0.1 Hz, with increasing strain amplitude. The results are shown in Figure 3.2. It can be seen

that the nonlinear behavior starts to show at about 1% strain, although there's some variation of this starting point from low temperature to high temperature. For the strain amplitude of 0.3% as we tested in this study, the material's behavior is well in the linear-viscoelastic region for all the temperatures.

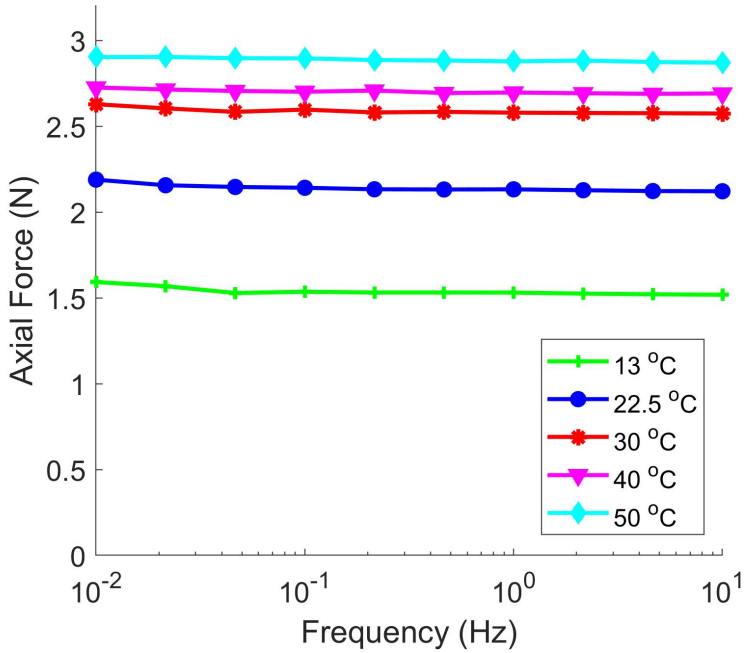

Figure 3.1: The variation of axial force during the frequency sweep

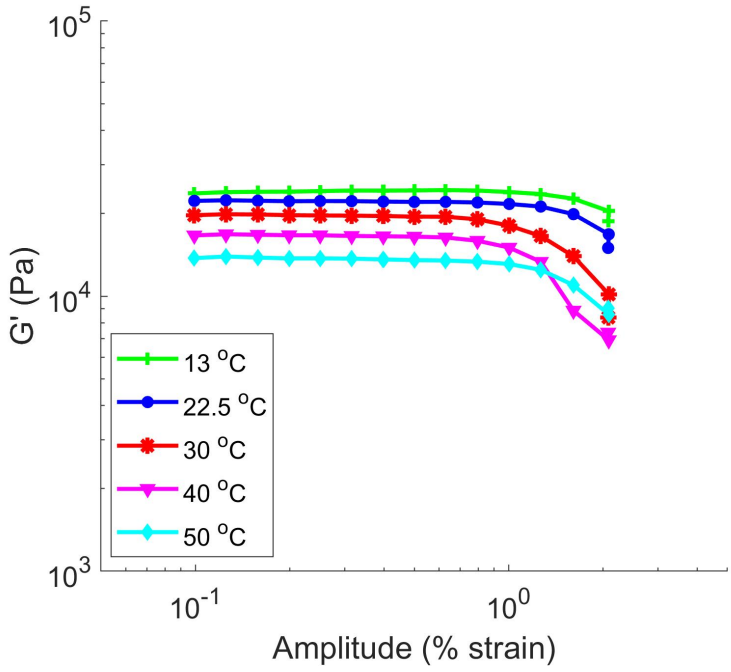

(a)

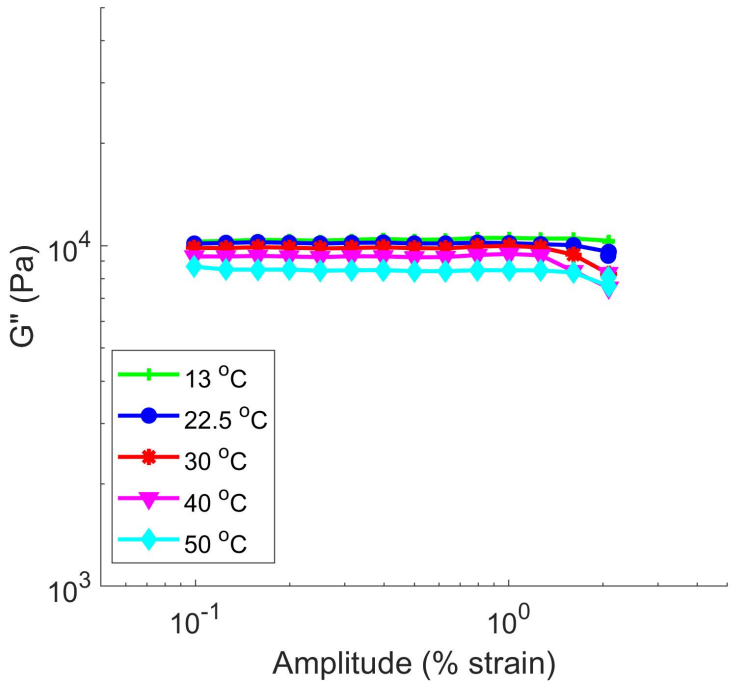

(b)

Figure 3.2: Plot of amplitude sweep at 0.1Hz of : (a) storage modulus G' (b) loss modulus G"

3.3 Results

3.3.1 Uniaxial Tension

Experimental results

The nominal stress σ, versus stretch ratio λ curves at different loading rates and temperatures are shown in Figure 3.3. In these figures, the maximum stretch ratio is 1.3, which is considerably higher than typical angular strain imposed in linear rheology. During the cyclic tests shown here, for all the temperatures and loading rates tested, we found a large hysteresis with a small residual deformation right after unloading the specimen to zero stress. At a fixed temperature, the stiffness of the gel increases with loading rate. At a higher loading rate, there are more connected physical crosslinks under a given stretch ratio, accumulating more stress. Figure 3.3 (f) shows the load versus stretch response at a stretch rate of 0.01/s at different temperatures. The gel is stiffer at a lower temperature and softer at a higher temperature. At a higher temperature, the breaking and reattaching rates are higher. This means at during a certain time period, there are more bond breaking and reattaching events occurring compared to lower temperature. This is equivalent to decreasing the loading rates. It has been shown that the material is softer at lower loading rates. Thus the results are consistent. Figure 3.4 shows results of the relaxation tests under different temperatures. It shows that the temperature affects the peak stress for the initial loading.

But the plateau stress of tests under different temperatures is about the same. This is consistent with the hypothesis of the constitutive model that, the plateau stress is determined by the chemical bonds instead of the physical bonds. The chemical bonds are much less sensitive to temperature compared to physical bonds.

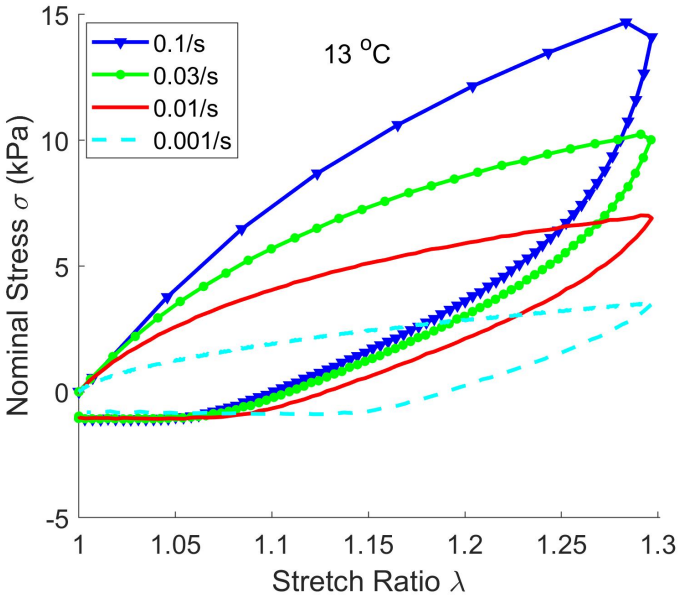
0.1/s
0.03/s
0.01/s
0.001/s
13 °C
Nominal Stress σ (kPa)
Stretch Ratio λ
15
10
5
0
-5
1
1.05
1.1
1.15
1.2
1.25
1.3

(a)

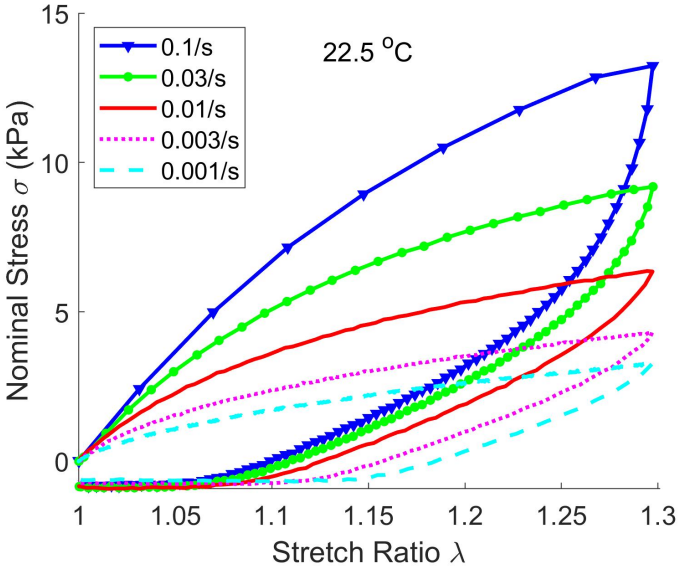
0.1/s
0.03/s
0.01/s
0.003/s
0.001/s
22.5 °C
Nominal Stress σ (kPa)
Stretch Ratio λ
15
10
5
0
1
1.05
1.1
1.15
1.2
1.25
1.3

(b)

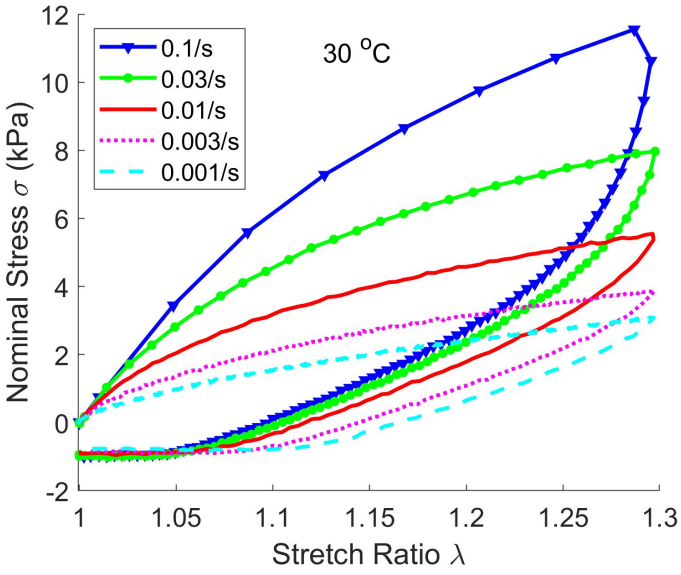
30 °C
0.1/s
0.03/s
0.01/s
0.003/s
0.001/s
Nominal Stress σ (kPa)
Stretch Ratio λ
12
10
8
6
4
2
0
-2
1
1.05
1.1
1.15
1.2
1.25
1.3

(c)

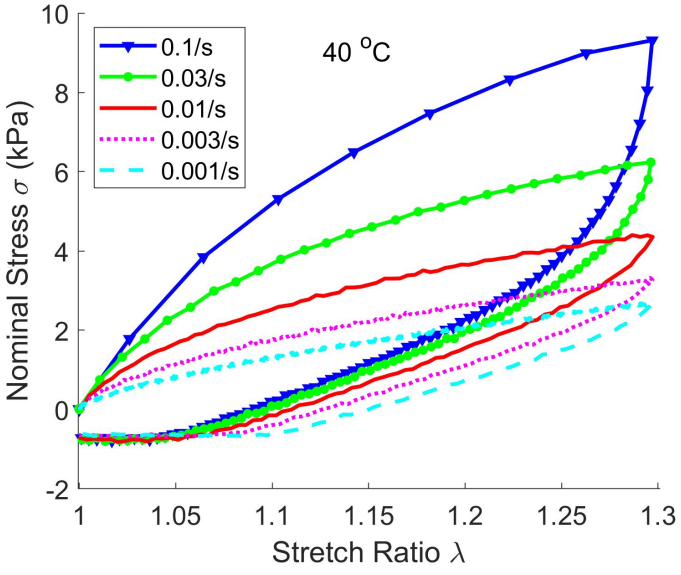
40 °C
0.1/s
0.03/s
0.01/s
0.003/s
0.001/s
Nominal Stress σ (kPa)
Stretch Ratio λ
10
8
6
4
2
0
-2
1
1.05
1.1
1.15
1.2
1.25
1.3

(d)

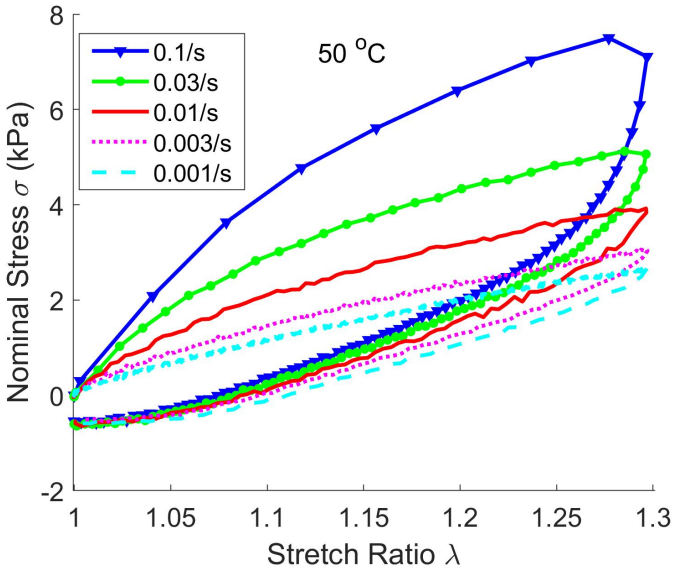

(e)

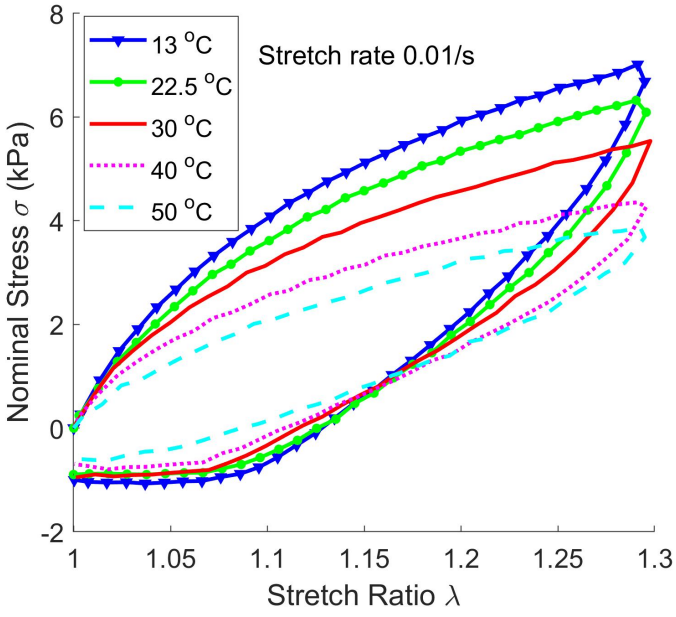

(f)

Figure 3.3: Plot of nominal stress versus stretch at different stretch rates and different temperatures: (a) 13 ^{o}C (b) 22.5 ^{o}C (c) 30 ^{o}C (d) 40 ^{o}C (e) 50 ^{o}C (f) effects of temperature on the stress-stretch curve at a fixed stretch rate of 0.01/s and varying temperature

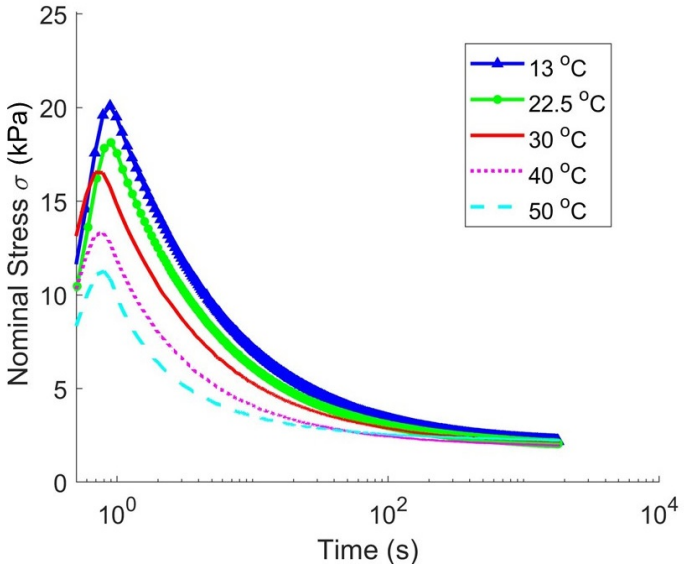

Figure 3.4: The results of the stress relaxation tests under different temperatures

Review of the constitutive model

Previously it has been shown that the constitutive model developed by Long et al.[13] and Guo et al.[14] can accurately predict the stress vs. stretch behaviors of uniaxial tension tests at room temperature. Here we briefly review the model.

The key assumptions used in this model are:

1. The elastic strands in the polymer network are connected by two types of crosslinks: chemical crosslinks and physical crosslinks. The chemical crosslinks are permanent and they don't break during the deformation. The physical crosslinks can break and reform.

2. The total strain energy in the network is equal to the sum of that carried by each individual polymer strand.

3. The breaking and reforming of the physical crosslinks reaches a dynamic equilibrium state before the hydrogel is subject to any loading. This equilibrium sates results in a constant molar fraction of connected and broken physical strands. It also implies that the breaking and reforming rates are equal and independent of time. This rate is denoted by $\bar{\gamma}_\infty$.

4. When physical crosslinks break, the stress in the strand that attaches to them is instantaneously relaxed and the strand carries no strain energy. When physical crosslinks reform at time τ, the deformation of the corresponding chain is governed by the deformation gradient $\mathbf{F}^{\tau \to t}$, where t is the current time.

5. Macroscopically the gel is assumed to be incompressible and isotropic. When subjected to the same stress, the chains between physical and chemical crosslinks deform in the same way so that the same strain energy model applies to permanent and temporary strands. The strain energy of the undamaged network W_0 is assumed to depend only on the first invariant of the right Cauchy-Green tensor, $I = tr[(\mathbf{F}^{0\to t})^T \mathbf{F}^{0\to t}]$

6. The breaking and reforming rates of the physical crosslinks are independent of the strain history.

With the previous assumptions, the nominal stress tensor $\mathbf{P}$ can be related to the deformation gradient $\mathbf{F}^{\tau\to t}$ by

$$\mathbf{P} = -p(\mathbf{F}^{0\to t})^{-T} + 2[n(t)+\rho]\frac{dW_0}{dI_1}|_{I_1=H(0,t)} \times \mathbf{F}^{0\to t} + \\ 2\bar{\gamma}_\infty \int_0^t \phi_B(\frac{t-\tau}{t_B})\frac{dW_0}{dI_1}|_{I_1=H(\tau,t)} \times \mathbf{F}^{\tau\to t}(\mathbf{F}^{0\to\tau})^{-T} d\tau \tag{3.1}$$

Where

- p is the Lagrange multiplier that enforces incompressibility.
- ρ is the molar fraction of the chemical crosslinks.
- dW_0/dI_1 is evaluated at $I_1 = H(x,\tau,t) \equiv tr[(\mathbf{F}^{\tau\to r})^T\mathbf{F}^{\tau\to t}]$. This implies that the strain energy carried by the temporary chains that reform at time τ depends only on the deformation from τ to the current time t.
- ϕ_B is the "survivability" function, characterizing the fraction of physical crosslinks that are formed at time τ and remain attached at time $t \geq \tau$.

$$\phi_B(\frac{t-\tau}{t_B}) = [1 + (\alpha_B - 1)\frac{t-\tau}{t_B}]^{\frac{1}{1-\alpha_B}} \tag{3.2}$$

  t_B is the characterstic time for bond breaking and $1 < \alpha_B < 2$ is a material parameter.

- $n(t)$ is the fraction of physical crosslinks that are attached at $t = 0$ and survive

until current time t.

$$n(t) \equiv \bar{\gamma}_\infty \int_t^\infty \phi_B(\tau/t_B)d\tau = \bar{\gamma}_\infty \frac{t_B}{2-\alpha_B}[1+(\alpha_B-1)\frac{t}{t_B}]^{\frac{2-\alpha_B}{1-\alpha_B}} \tag{3.3}$$

As $1 < \alpha_B < 2$, $n(t)$ is a decaying function

For uniaxial tension, the nominal stress in the loading direction σ has the following form:

$$\begin{aligned} \sigma = 2[\rho + n(t)]\frac{dW_0}{dI_1}|_{H(0,t)}[\lambda(t) - \frac{1}{\lambda^2(t)}]+ \\ 2\bar{\gamma}_\infty \int_0^t \phi_B(\frac{t-\tau}{t_B})\frac{dW_0}{dI_1}|_{H(\tau,t)} \times [\frac{\lambda(t)}{\lambda^2(\tau)} - \frac{\lambda(\tau)}{\lambda^2(t)}]d\tau \end{aligned} \tag{3.4}$$

Here λ is the stretch ratio in the loading direction, and

$$I_1(t) = \lambda^2(t) + \frac{2}{\lambda(t)} \tag{3.5}$$

$$H(\tau,t) = [\frac{\lambda(t)}{\lambda(\tau)}]^2 + 2\frac{\lambda(\tau)}{\lambda(t)}, \tau < t \tag{3.6}$$

In the expression for uniaxial tension (3.4), the first term on the right hand side describes the loss of stress due to breaking of the temporary crosslinks that were connected at time $t = 0$. The integral term describes the recovery of stress from the reattachment of temporary crosslinks.

For this study, we assume that all chains are Gaussian, and the energy W_0 is given by the neo-Hookean model:

$$W_0 = \frac{\mu}{2}(I_1 - 3) \tag{3.7}$$

Where μ is the small strain shear modulus of the neo-Hookean model at $t = 0$ when no load is applied and all physical chains remain intact. In this case, the constitutive model is completely specified by four independent material parameters, $\mu\rho$, $\mu\bar{\gamma}_\infty$, α_B and t_B. Here $\mu\rho$ is the long time modulus of the hydrogel in a stress relaxation test, when all the physical chains do not carry any load. It corresponds to the shear modulus of the network crosslinked only by the chemical crosslinks. $\bar{\gamma}_\infty$ is the equilibrium reformation rate of the physical crosslinks. Thus $\mu\bar{\gamma}_\infty$ can be roughly though of as a parameter measuring how stresses increase the number of re-attached physical chains per unit time. $1 < \alpha_B < 2$ controls the average survival time of a newly attached transient bond. t_B is the characteristic breaking time. Those four parameters can be obtained by fitting the constitutive model to the experimental results in a uniaxial relaxation test and a uniaxial tension test with a fixed loading rate. Details of the fitting process can be found in [14].

Model fitting

We further show here that the model can also accurately predict the uniaxial tension tests at different temperatures. The fitting was performed by Guo. For each temper-

ature, the stress relaxation test data was firstly used to estimate the four material parameters (details of the fitting method were given in [14]). These parameters were then fine-tuned to match both the cyclic tension test data and the rheology data. The obtained material parameters are summarized in Table 3.1. It can be seen that temperature has different effects on these four parameters. The parameters $\mu\rho$ and α_B are insensitive to temperature while $\mu\bar{\gamma}_\infty$ increases and t_B decreases with increasing temperature.

With the obtained material parameters, the constitutive model was used to predict the material response under uniaxial tension tests for different temperatures and loading rates. The comparison between the model prediction and experimental data for three different temperatures are shown in Figure 3.5. It can be seen that the agreement between the experiments and theory is very good.

Temperature (^{o}C)	$\mu\rho$ (kPa)	$\mu\bar{\gamma}_\infty$ (kPa/s)	α_B	$t_B(s)$
13	3.34	25.21	1.62	12.33
22.5	3.14	27.85	1.62	11.65
30	3.33	34.30	1.62	11.07
40	3.11	46.12	1.61	9.76
50	3.16	53.61	1.61	8.76

Table 3.1: The model fitting parameters for different temperatures

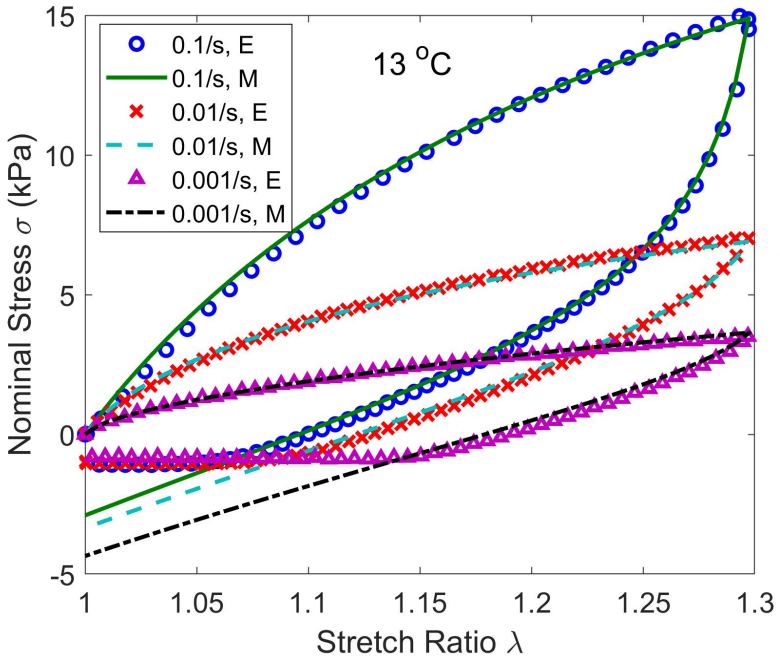
13 °C
0.1/s, E
0.1/s, M
0.01/s, E
0.01/s, M
0.001/s, E
0.001/s, M
Nominal Stress σ (kPa)
Stretch Ratio λ
15
10
5
0
-5
1
1.05
1.1
1.15
1.2
1.25
1.3

(a)

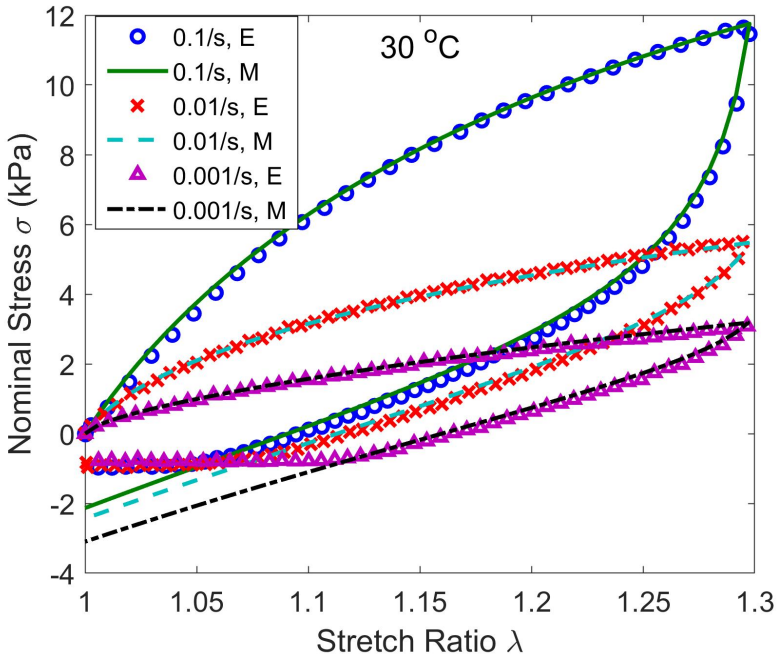
30 °C
0.1/s, E
0.1/s, M
0.01/s, E
0.01/s, M
0.001/s, E
0.001/s, M
Nominal Stress σ (kPa)
Stretch Ratio λ
12
10
8
6
4
2
0
-2
-4
1
1.05
1.1
1.15
1.2
1.25
1.3

(b)

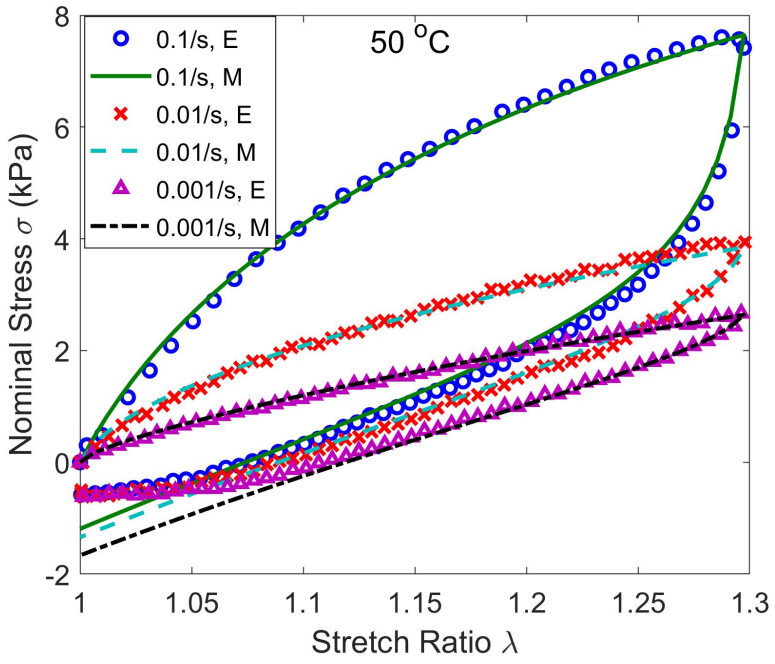

(c)

Figure 3.5: Comparison of model and experimental results at three different stretch rates and temperatures of (a) 13 ^{o}C, (b) 30 ^{o}C, and (c) 50 ^{o}C. "E" stands for experimental data, and "M" stands for model prediction using parameters from Table 3.1.

3.3.2 Rheology

Experimental data and shifting

The storage modulus G', loss modulus G'' and $tan\,\delta = G''/G'$ obtained from rheology tests at linear-viscoelastic region are shown in Figure 3.6. It can be seen that as expected the temperature has effects on those quantities. First, we investigated whether these data can be collapsed into a single master curve using time-temperature super-

position [36] defined by $b_T G'(T, \omega a_T) = G'(T_{Ref}, \omega)$, where ω is the frequency, T is temperature, and a_T and b_T are the horizontal and vertical shift factors. The same shifting is applied to G''. We used room temperature, $T_{Ref} = 22.5\ ^oC$ as the reference temperature. In conventional polymer melts where the dynamics are due to monomer friction, tan δ data at different temperatures depend only the horizontal shift factor because both G' and G'' are affected by the same vertical shift factor. Thus we first used the tan δ data to obtain the horizontal shift factors at each temperature. The shifted tan δ data are plotted in Figure 3.7 (a). We applied these horizontal shifts to G' followed by a vertical shift to collapse these data onto a master curve. The same vertical shift was then applied to G''. The results are shown in Figures 3.7 (b) and (c). The shift factors are tabulated in Table 3.2. Comparing Figures 3.7 with the pre-shifted data in Figure 3.6, we conclude that the time-temperature superposition works well for our gel for all the frequencies in the tests. The horizontal shift factors have a wide range, from 1.20 to 0.41 over the 13 to 50 ^{o}C temperature range, while the vertical shift has a smaller range, 0.96 to 1.16.

Table 3.2: Shift parameters from model fitting and rheology results

Temperature(^{o}C)	t_B	a_T tension tests	a_T rheology	b_T tension tests	b_T rheology
13	0.49	1.17	1.20	0.95	0.96
22.5	0.42	1.00	1.00	1.00	1.00
30	0.32	0.77	0.79	1.07	1.05
40	0.22	0.52	0.53	1.23	1.12
50	0.16	0.39	0.41	1.37	1.16

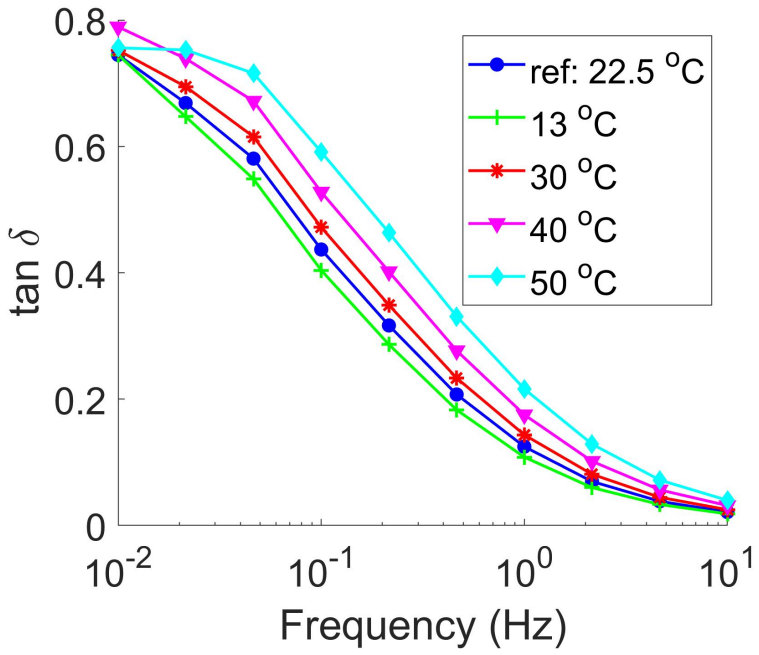
0.8
0.6
0.4
0.2
0
tan δ
ref: 22.5 °C
13 °C
30 °C
40 °C
50 °C
10-2
10-1
100
101
Frequency (Hz)

(a)

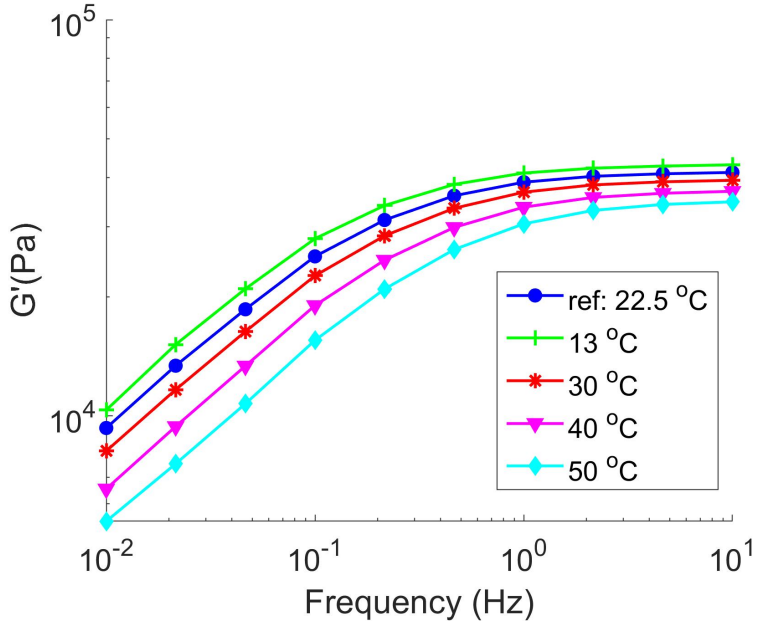
105
104
G'(Pa)
ref: 22.5 °C
13 °C
30 °C
40 °C
50 °C
10-2
10-1
100
101
Frequency (Hz)

(b)

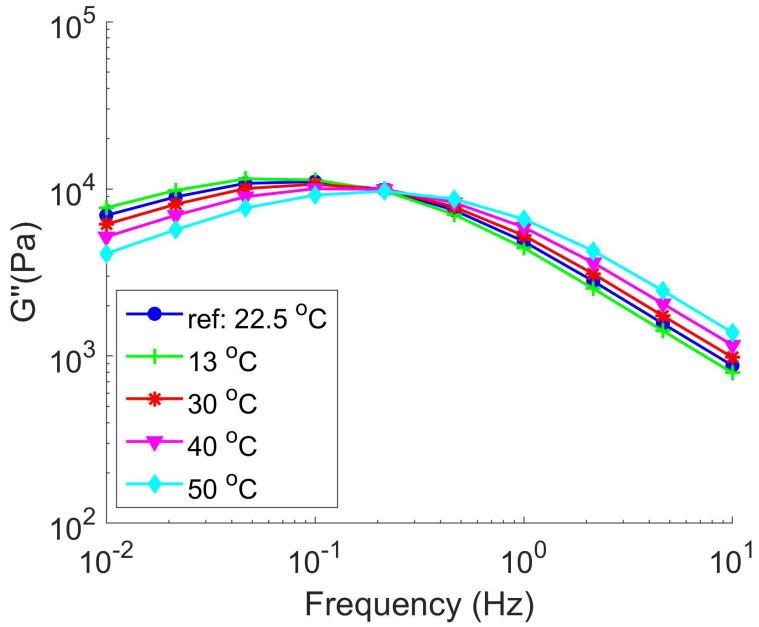

(c)

Figure 3.6: Results of the rheology tests: (a) tan δ (b) G' (c) G"

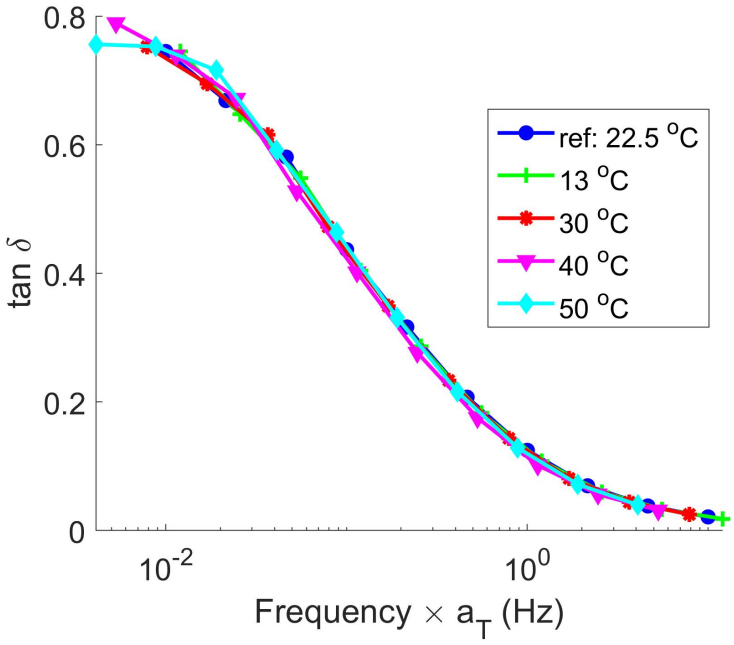
0.8
0.6
0.4
0.2
0
tan δ
10^-2
10^0
Frequency × a_T (Hz)
ref: 22.5 °C
13 °C
30 °C
40 °C
50 °C

(a)

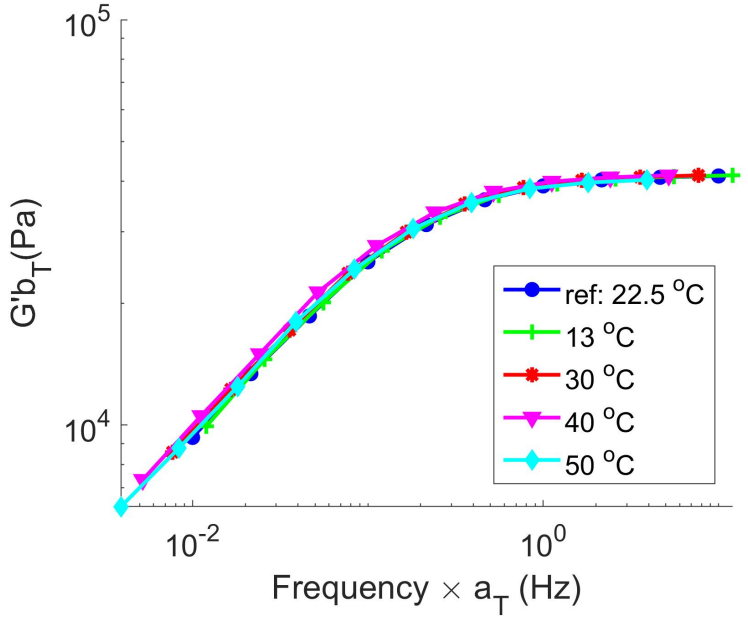

(b)

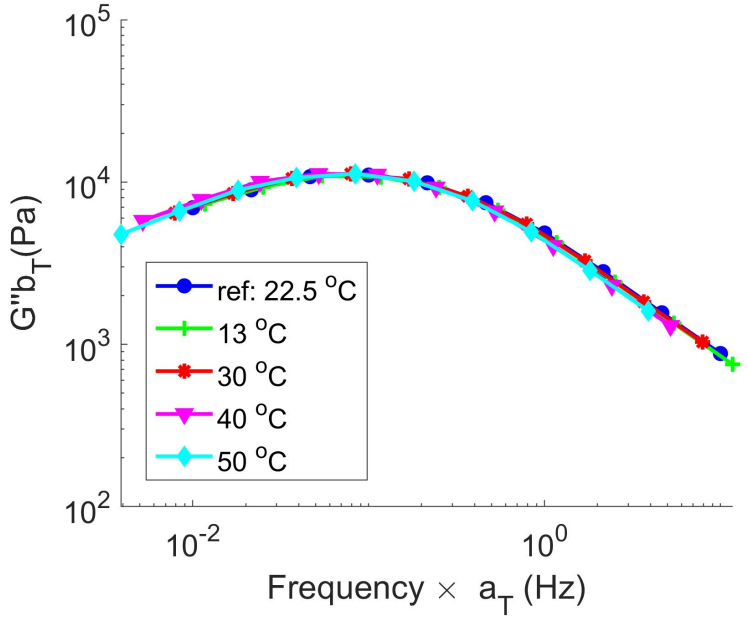

(c)

Figure 3.7: Master curves of: (a) tan δ (b) G' (c) G"

G' and G" from constitutive model

From [15], based on the previously developed constitutive model, the storage and loss moduli G' and G" have the following forms:

$$G'(\omega) = \mu\rho + \mu\rho K(T) I_1(\omega t_B, \alpha_B) \tag{3.8}$$

$$G"(\omega) = \mu\rho K(T) I_2(\omega t_B, \alpha_B) \tag{3.9}$$

where

$$I_1(\omega t_B, \alpha_B) \equiv 1 - \frac{2-\alpha_B}{\alpha_B - 1} \int_0^\infty \cos(\frac{\omega t_B}{\alpha_B - 1} x)(1+x)^{-\frac{1}{\alpha_B - 1}} dx \tag{3.10}$$

$$I_2(\omega t_B, \alpha_B) \equiv \frac{2-\alpha_B}{\alpha_B - 1} \int_0^\infty \sin(\frac{\omega t_B}{\alpha_B - 1} x)(1+x)^{-\frac{1}{\alpha_B - 1}} dx \tag{3.11}$$

$$K(T) = \frac{\bar{\gamma}_\infty t_B}{(2-\alpha_B)\rho} = \frac{(1-\rho)/\rho}{1 + (2-\alpha_B)(t_H/t_B)} \tag{3.12}$$

where ω is the frequency in radians/s. t_H is the characteristic healing time [13] [14]. Using the parameters listed in Table 3.1 we can also calculate the storage modulus G', loss modulus G" and $\tan\delta = G'/G$" in the rheology tests. Comparison between the model prediction and the experimental results at room temperature is shown in Figure 3.8. The model agrees well with the experimental data. Results for other temperatures fit equally well.

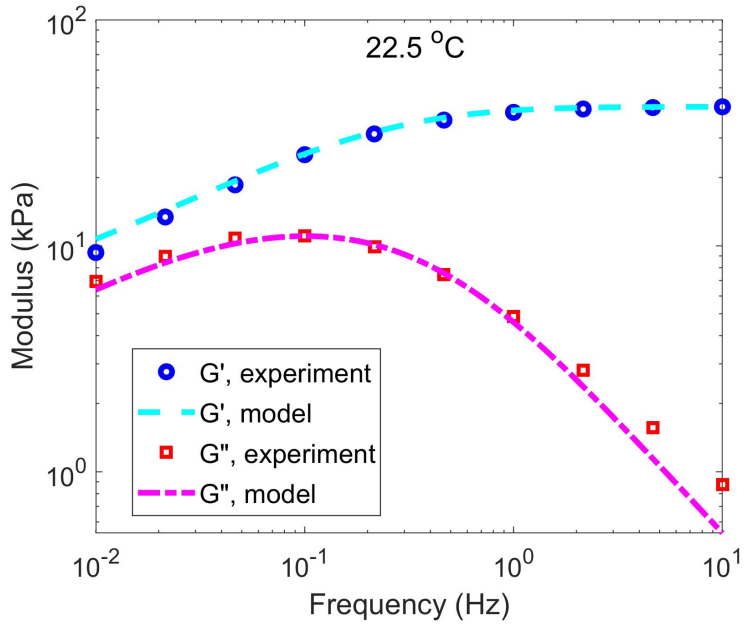

(a)

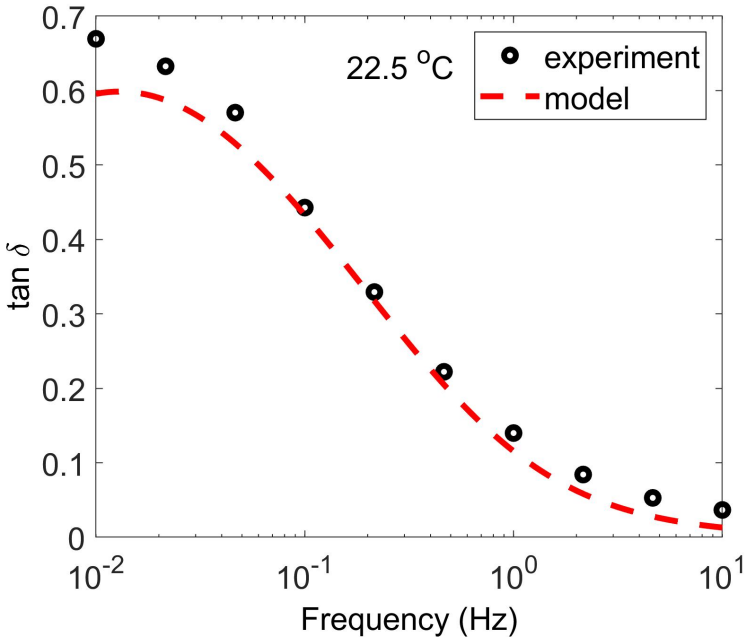

(b)

Figure 3.8: G', G'' and tan δ for room temperature. (a) G' and G'' from model and rheology data. Model results are shifted by a vertical constant to account for pre-compression, this procedure was also used in [15] (b) tan δ from model and rheology data

3.4 Discussion

In previous sections, we have shown that the temperature has effects on the mechanical response of PVA dual-crosslink hydrogel in both the uniaxial tension tests and rheology tests. In the uniaxial tension tests, the effects can be seen from the model fitting parameters. In the rheology tests, the effects of temperature can be described by the shift factors in time-temperature superposition. Here we further show that there is equivalence in the model fitting parameters from uniaxial tension tests and the shift factors from the rheology tests. To understand this relation, a careful examination of the material fitting parameters is necessary. There are four independent material parameters in the constitutive model. They are given in Table 3.1 for different temperatures. In a stress relaxation test the modulus at long time is $\mu\rho$. Here ρ is the molar fraction of chemical crosslinks, which we do not expect to have a strong temperature dependence. The small strain shear modulus μ is, according to rubber elasticity, proportional to the absolute temperature, so the fractional change of $\mu\rho$ should be very small for the range of temperature used in the experiments. This is consistent with the results of the relaxation test, which shows that the long time moduli are quite insensitive to temperature.

The other two material parameters, $\mu\bar{\gamma}_\infty$ and t_B, describe the dynamics of chain breaking and reattaching. As the temperature increases, the dynamics accelerate, resulting in a shorter average chain life, thus one would expect the characteristic time

for breaking, t_B , to decrease with temperature, which can be seen from 3.1. Finally, Table 3.1 shows that the exponent α_B of the survivability function is insensitive to temperature.

The constitutive model provides more insight into the TTS for the rheology tests. In order for TTS to work perfectly, G' and G" should have the separable form:

$$G' = b(T)\phi_S(\omega a(T)) \tag{3.13}$$

$$G\text{"} = b(T)\phi_L(\omega a(T)) \tag{3.14}$$

And this gives:

$$tan\,\delta = \phi_L(\omega a(T))/\phi_S(\omega a(T)) \tag{3.15}$$

where a(T) and b(T) are the horizontal and vertical shift factors that depend only on the temperature T. ϕ_L and ϕ_S are functions that depend only on $\omega a(T)$. We first look at tan δ =G"/G'. From (3.8) and (3.9),

$$tan\,\delta = \frac{K(T)I_2(\omega t_B)}{1 + K(T)I_1(\omega t_B)} \tag{3.16}$$

As we've shown in Table 3.1 that α_B is independent of temperature, so I_1 and I_2 depend only on ωt_B. In classical TTS, tan δ should depend only on the horizontal shift, not on the vertical shift. From (3.10), (3.11) and (3.12), the dependence of tan δ on the frequency ω is always scaled together with the characteristic breaking time

t_B. In classical TTS, the horizontal shift factor is defined as $a_T = \omega^{ref} \ / \ \omega$. Here the superscript ref indicates the reference temperature. As the dependence of ω is also inversely scaled with t_B, the horizontal shift factor can also be defined as $a_T = t_B/t_B^{ref}$. Since in theory tan δ does not depend on vertical shift factors, this is satisfied if and only if in (3.16) K(T) = K_0 is independent of temperature. If this is the case, the moduli G' and $G"$ will have the following forms:

$$G' = \mu\rho K_0[\frac{1}{K_0} + I_1(\omega t_B)] \tag{3.17}$$

$$G" = \mu\rho K_0[I_2(\omega t_B)] \tag{3.18}$$

Here the terms with ωt_B governs the horizontal shift. From (3.17) and (3.18), the vertical shift factor is in fact:

$$b(T) = \mu\rho K_0 = \frac{\mu\bar{\gamma}_\infty t_B}{2 - \alpha_B} \tag{3.19}$$

At this point, we've derived the relation between the material parameters fitted from uniaxial tension tests and the shift factors obtained from rheology tests. The shift factors from both the constitutive model and the rheology experiments are listed in Table 3.2. It can be seen that the horizontal factors computed from both sources are highly consistent. The vertical shift factors agree less well at the higher temperatures (40 and 50 ^{o}C). This is because $K(T)$ is not a constant independent of temperature. From (3.12), $K(T)$ depends on ρ and on the ratio t_H/t_B. This ratio need not be

independent of temperature since the characteristic time of healing t_H depends on the availability of binding sites, which is not the case for breaking. In addition, since the number of "free" physical crosslinks which are not bound to the network increases with temperature, the molar fraction of the chemical crosslinks ρ could increase with temperature. For this reason, we cannot expect $K(T)$ to be independent of temperature and therefore TTS is not completely satisfied by the constitutive model.

In time-temperature superposition, the dependence of shift factors on the temperatures often follow empirical equations like W-L-F or Arrhenius equation. Our data suggest that $log_{10}\ a_T$ and $log_{10}(1/(Tb_T))$ are approximately inversely linear in temperature, i.e.,

$$log_{10}(a_T) = \frac{E_a}{2.303R}(\frac{1}{T} - \frac{1}{T_0}) \tag{3.20}$$

$$log_{10}(\frac{1}{Tb_T}) = \frac{E_b}{2.303R}(\frac{1}{T} - \frac{1}{T_0}) \tag{3.21}$$

where $R = 8.314 J/(mol \cdot K)$ is the gas constant, E_a and E_b are the activation energies associated with bond breaking and the enthalpy of association respectively. Figure 3.9 compare (3.20) and (3.21) with the shift factors we obtained from rheology test and tension test data, using $E_a = 25.6$ kJ/mol and $E_b = 6.63$ kJ/mol. Within the range of temperatures considered here, the shift factors fit the Arrhenius law, (3.20) and (3.21), well with some deviation at high temperature. The value of E_a is reasonable for a PVA-borax system; for solutions (without chemical crosslinks) a value of 42

kJ/mol was previously reported [37] [38]. The value of E_b is much smaller than E_a which is to be expected since the vertical shift is much less. This is the reason why TTS works in this frequency range.

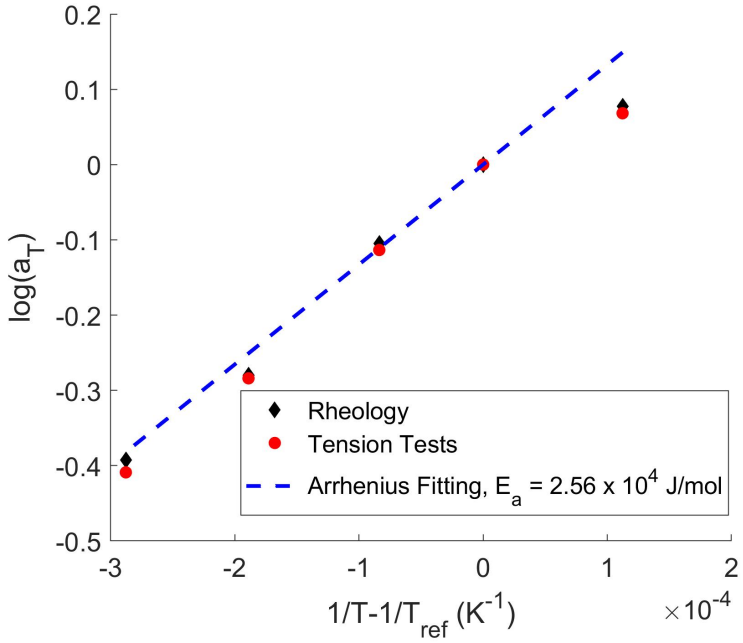

(a)

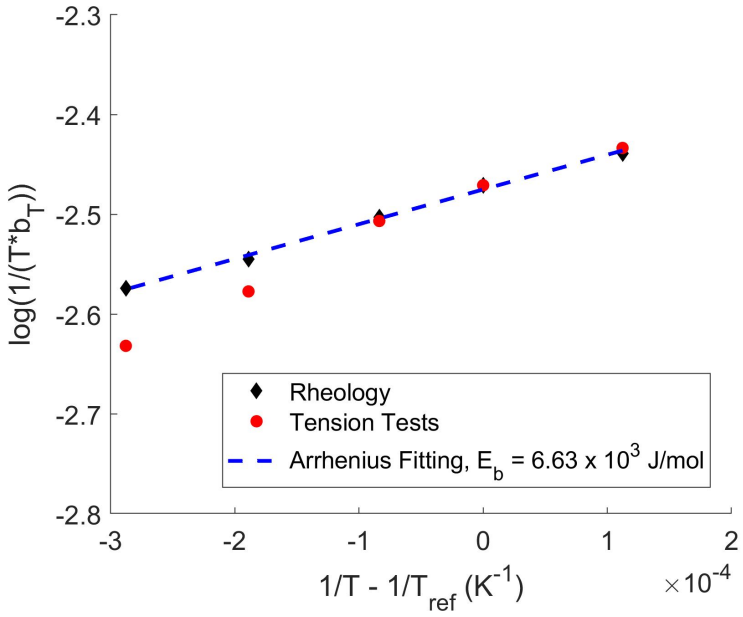

(b)

Figure 3.9: (a) Horizontal shift factors: $log_{10}\ a_T$ from the rheology tests, calculated from the tension tests and from Arrhenius fitting of the shift factors, using $E_a = 2.56 \times 10^4$ J/mol. (b) Vertical shift factors: $log_{10}\ a_T$ from the rheology tests, calculated from the tension tests and from Arrhenius fitting of the shift factors, using $E_b = 6.63 \times 10^3$ J/mol.

3.5 Conclusion

Cyclic tension and rheology tests were carried out on a PVA dual cross-link hydrogel at different temperatures. The tension tests were performed under moderately large strains while the rheology tests were performed at small strains. The storage and loss moduli from the rheology tests are found to obey time-temperature superposition (TTS).

The tension test and rheology test data at all test temperatures can be explained by a nonlinear viscoelastic constitutive model with four independent material parameters. These parameters are determined independently by performing relaxation tests at different temperatures and after a slight amount of fine-tuning, are found to match both tension and rheology data at different temperatures. Those parameters have different dependence on temperature. We find that α_B and $\mu\rho$ are approximately independent of temperature while $\mu\bar{\gamma}_\infty$ and t_B are strongly temperature dependent. It should be noted that TTS imposes very stringent requirements on the constitutive model. We find that the constitutive model approximately satisfies the stringent requirements needed for simple TTS to be valid.

CHAPTER 4

APPLICATION OF DIGITAL IMAGE CORRELATION TO THE MEASUREMENT OF STRAIN CONCENTRATION

4.1 Introduction

Experiments play an important role in determining the mechanical properties of hydrogels. Conventional methods like uniaxial tension/compression and rheology tests are relatively easy to perform and are widely used to obtain the material properties. However, they measure only homogeneous material response and cannot probe the response of the material in the presence of cracks or other stress concentrators, which is important for problems such as contact and fracture prediction. As a non-contact, full-field deformation measurement method, digital image correlation (DIC) is an ideal candidate for the measurement of inhomogeneous deformation of hydrogels. DIC measures deformation by tracking the position change of a group of pixels (subset) from the images corresponding to undeformed and deformed states. 2D DIC

measures planar motion and requires only one camera. The details of 2D DIC can be found in the comprehensive review papers published by Pan et al. [39], Khoo et al. [40] and in Sutton's book [41].

Several researchers have applied 2D DIC (referred to here as simply DIC) to study the material response involving strain concentration of soft materials like gels. The interest has been steadily increasing. For instance, Kwon et al. [20] evaluated the stress–strain relationship, strain localization and Poisson's ratio of an agarose gel using DIC. In their experiment, a small notch was made on the agarose gel specimen, and the strain close to the notch was measured with DIC. This strain was considered as the failure strain of the material. Sasson et al. [21] used DIC to measure the surface strain induced by a spherical tip indenter indenting chitosan hydrogels. The results were used to demonstrate the capability of their constitutive model. Leibinger et al. [22] used a laser-based image correlation method to measure the displacement and strain fields induced during the insertion of a needle into soft tissue phantoms. Hong et al. [23] applied DIC in their investigation of bubble cavitation damage to a tissue surrogate. Christensen et al. [24] implemented DIC to determine the local strain distribution within 3D printed hydrogel structures, observing the deformation at printed interfaces and identifying regions of increased localized deformation for samples under uniaxial tension. Wyss et al. [25] performed DIC at both macro and micro scales to measure the local strain field of a cellulose/hydrogel composite under cyclic loading. The results uncovered the effects of cyclic loading on the local strain

distribution.

Despite the above-mentioned studies, the accuracy of the DIC measurement of highly localized deformations in hydrogels has not been well established. There are still several possible sources of inaccuracy in DIC such as system alignment, quality of the optics, speckle pattern, and subset size [42] [43] [44] [45] [46] . The existence of large deformations and high strain gradients may exacerbate these issues. Thus, the accuracy of the method must be carefully examined before the measured results can be reliably applied to fracture problems. In prior works such as [22] [25] , the DIC results were explored in a qualitative way. In other studies, strain contours obtained from DIC were qualitatively compared to FEM simulations [21] or the minimum/maximum strain values were compared [47]. To establish the accuracy of the methodology, more careful comparison between the experimental results and reliable numerical simulation is necessary. This is the prerequisite to apply DIC to obtain more reliable, quantitative information, such as experimentally measuring crack tip loading parameters for fracture mechanics applications.

In this study, we applied DIC to measure the localized deformation of PVA dual-crosslink hydrogel specimens involving strain concentrations. The principal goals of this study are to establish the accuracy of the DIC measurement for our material and setup, validate the measurements in cases of large strain gradients and then to apply the results to prove a theoretical result predicted in our prior work, namely that the deformation fields in a cracked sample of the viscoelastic hydrogel are stationary

during a stress relaxation test. A secondary goal is to provide guidance on practical aspects such as the optical setup and speckle pattern.

We begin with a brief outline of the material synthesis. Details of the experimental setup are then discussed, including the preparation of the speckle pattern, the optical system, load application and validation of the test system. Details on the preparation and quality of the speckle pattern are discussed as these may be problematic for some hydrogels due to their high water content. The effects of DIC analysis parameters such as subset size and strain radius are discussed, and the method's accuracy is assessed against results from uniaxial tension and from geometries involving large strain gradients. After the accuracy of the method has been carefully validated, we apply DIC to the question of the time dependence of deformation fields in a cracked sample of the hydrogel during a stress relaxation test.

4.2 Methodology

4.2.1 Speckle Pattern Preparation

Generating a high-quality speckle pattern is challenging for this type of hydrogel due to high water content of about 90%. Several techniques to generate speckle patterns have been explored by other researchers, such as spraying ink with an airbrush [23] [47] [48], powder deposition [20] [21] [49], marking using a marker pen [50], transfer from an inkjet-printed pattern on acetate to the gel [51] and embedding fluorescent

or white light micro-beads [22] [24] [52] [53]. In some cases, the material has enough intrinsic contrast, thus no patterning is needed [54]. We explored airbrush spraying, powder deposition and using a marker pen and concluded that spraying black ink using an airbrush works best. This process can be performed in a short time period and the pattern can be consistently repeated. The primary challenge for airbrush spraying is that as the surface of the hydrogel mostly consists of water, the drying of the paint is slow and thus wet ink drops may coalesce or smear as shown in Figure 4.1 (a).

To generate a high-quality pattern using an airbrush, an ink that dries fast and has dark and opaque color is needed. In this research, after trying several different types of ink, we chose Koh-I-Noor RAPIDRAW ink. Patterns with very large speckles and a very high speckle density should be avoided, as those patterns are more likely to smear as shown in Figure 4.1 (a). Finer, moderately dense speckles dry faster and do not smear. To obtain a fine pattern, a relatively high air pressure of 80 psi was supplied to an IWATA HP-C airbrush. A low flow of ink should be used, which can be achieved by adjusting the airbrush trigger during painting. To allow the spray to start to dry in flight, the airbrush should be held relatively far from the sample, about 0.6 m. During one stroke of the airbrush only a small number of particles are painted on the surface of the specimen. The density of the speckles can be controlled by the number of strokes. An example of a pattern we generated for this study is shown in Figure 4.1 (b). The quality of the pattern will be further assessed later.

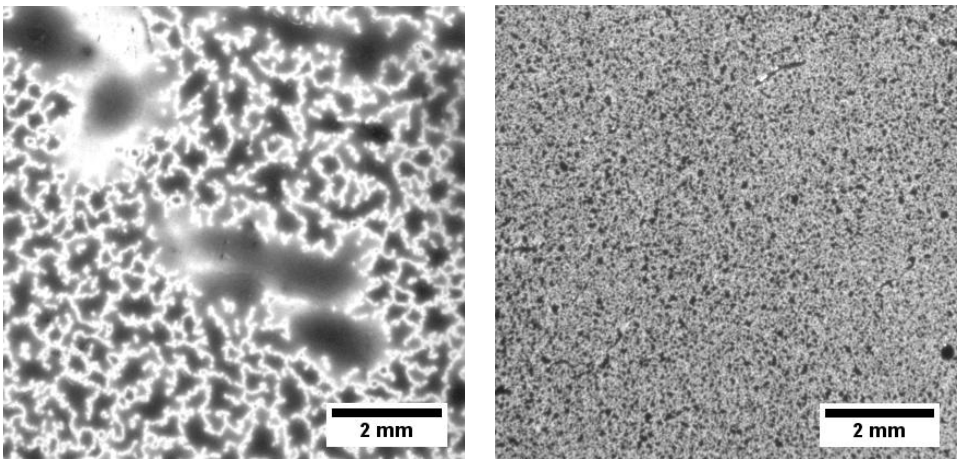

(a) (b)

Figure 4.1: Representative views of the speckle patterns (a) a low-quality pattern that smears (b) a high-quality pattern we generated in this study

4.2.2 DIC Setup

We performed DIC with an in-house built experimental setup. The mechanical loading was applied using a custom-built tensile tester. The hydrogel specimen was clamped between two aluminum grips. Sand paper sheets were glued to the inside of the grips to minimize sample slippage. The bottom grip was fixed to a base and the translational motion of the top grip was provided by a Zaber X-LSM200A-E03 translational stage. The linear motion resolution of the stage is 0.047625 μm. Load was measured by an Interface SMT1-1.1 load cell (4.9 N capacity) and displacement by an OMEGA LD620 LVDT.

Images for DIC measurements were acquired using a CCD camera (FLIR Grasshopper3 4.1 MP Mono) with a telecentric lens (Edmund Optics, SilverTL 0.16 $\times$). Two LED lights were used to provide additional illumination. The whole experimental

setup was fixed on an optical breadboard, as shown in Figure 4.2. A high-quality image acquisition system is of utmost importance in obtaining high-quality DIC results. Here we choose a telecentric lens for the following two reasons: First, it has a very small distortion ratio. Second, it helps minimize the effects of out-of-plane motion and the non-perpendicularity between the specimen and optical axis. The strain errors due to both out-of-plane motion and non-perpendicularity are proportional to Z^{-1}, the inverse of the distance between the object and the plane of the lens [44] [55]. For a telecentric lens, the distance Z is characterized by an effective distance $Z_{effective}$, which is much larger than the physical distance Z. Thus, the above-mentioned errors can be significantly reduced.

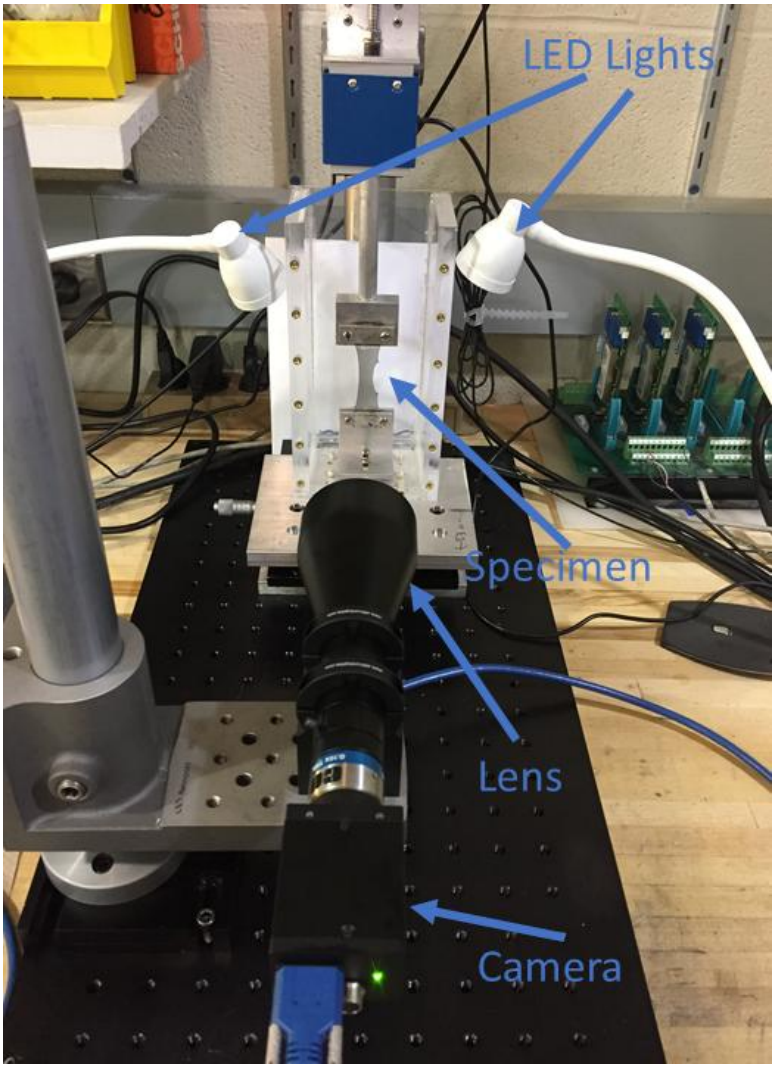

Figure 4.2: Experimental setup for large strain testing of hydrogel and deformation measurement with DIC

4.2.3 DIC Software

The DIC software used in this study was Ncorr, a freely available open source program based on MATLAB [56]. Ncorr utilizes the reliability guided DIC algorithm developed by Pan et al. [57]. To account for large deformation, Ncorr utilizes an algorithm developed also by Pan et al. [58]. Instead of using a fixed reference image,

the reference image is updated based on the correlation coefficient. During the application, there are three important parameters that will affect the DIC results: the subset radius, the radius of a circular subset used to correlate sub-images; the subset spacing, the spacing between neighboring subsets; and the strain radius. The strain radius represents the size of the region over which displacement data are fit to a plane in order to calculate the displacement gradient. The parameters used for a specific test will be provided. More details about this software are available in [56] and its website (http://www.ncorr.com/).

4.2.4 Convention of Deformation Measurement

In this study, we follow the convention used in Ncorr. The horizontal (x direction) and vertical (y direction) displacements are denoted by U and V respectively. The stretch ratio, which is the current length divided by the original length, is denoted by λ. The strain measure used in this study is Lagrangian strain $\boldsymbol{\varepsilon^{Lag}}$, which is defined as $\boldsymbol{\varepsilon^{Lag}} = \frac{1}{2}$ **(F^{T}F - I)**, with **F** being the deformation gradient and **I** the identity tensor. All the strains are viewed with respect to the reference (undeformed) configuration.

4.3 Validation under Homogeneous Deformation

As mentioned before, there are several issues that can introduce errors to DIC measurement. Some of them are inevitable. So, before applying DIC to complex geometries, it is necessary that the inherent error of the whole experimental setup is

estimated. These issues include: the quality of the speckle pattern; the effects of gel drying on the measured strain fields; the alignment of the test setup; lens distortion; and sample slippage. The above-mentioned effects can be measured using simple calibration tests such as rigid body translation and uniaxial tension tests.

4.3.1 Quality of the Speckle Pattern

A high-quality speckle pattern is critical to an accurate DIC measurement. A basic requirement is that the pattern is mechanically robust: it does not smear or debond from the surface of the specimen under large deformation. This is usually not a problem for dry materials such as rubber. However, for some hydrogels with high water content, the water might seep from the surface of specimen and interact with the generated pattern. Thus, special attention needs to be paid to patterning such materials.

To test whether the speckle pattern is mechanically robust, we tested the speckle pattern under large deformation and multiple loading cycles. We preloaded the specimen to a stretch ratio λ of 1.2 then took a reference image. Here a pre-stretch λ of 1.2 is chosen as the reference configuration in order to avoid the possible issue of buckling upon unloading. Then we loaded the specimen from $\lambda = 1.2$ to 1.6 at a stretch rate of $\dot{\lambda} = 0.05/\text{s}$ and unloaded to $\lambda = 1.2$. This loading and unloading was repeated for 8 cycles. Then a second image was taken at $\lambda = 1.2$ (current image). After this, we carefully examined the pattern in the current image to confirm that the pattern

was intact after cycles of loading. The details of the speckle pattern in a 4 × 4 mm region of interest (ROI) in the reference and current images are shown side by side in Figure 4.3. A careful examination of Figure 4.3 can confirm that the speckle does not show any visible change after the cyclic loading to large deformation. This is a first indicator of the robustness.

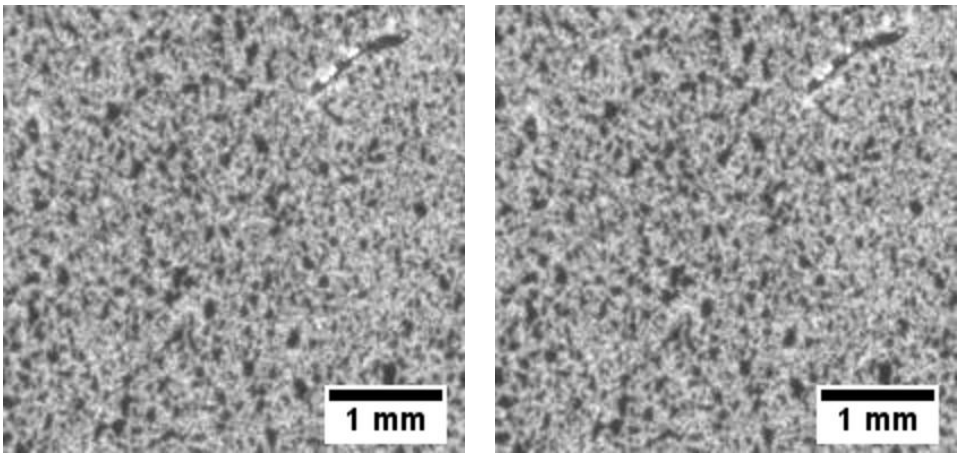

(a) (b)

Figure 4.3: The details of speckle pattern in a 4 ×4 mm region of interest. (a) reference image: taken before loading (b) current image: taken after the 8 cycles of loading from $\lambda = 1.2$ to 1.6

To make further validation, DIC was applied to the reference and current images and relative strains were obtained in a region of interest (ROI) of about 10 mm × 8 mm. A subset size of 35 pixels, a subset spacing of 2 pixels and a strain radius of 5 were used . The strain results are shown in Figure 4.4. The average and standard deviation of the strains within the ROI are summarized in Table 4.1. It can be seen that the induced strain is on the order of 10^{-3}, very small relative to the strains we will apply to this gel. Thus, we concluded that the pattern is robust enough for the purpose of

this study. Note that the shear strain ε_{xy}^{Lag} is one order of magnitude smaller than ε_{xx}^{Lag} and ε_{yy}^{Lag}. In this study, the specimen is symmetric and in most cases, we expect a very small ε_{xy}^{Lag} comparing to ε_{xx}^{Lag} and ε_{yy}^{Lag}. Thus, to make the discussion more concise, we'll focus on the normal strains ε_{xx}^{Lag} and ε_{yy}^{Lag} for the rest of this chapter.

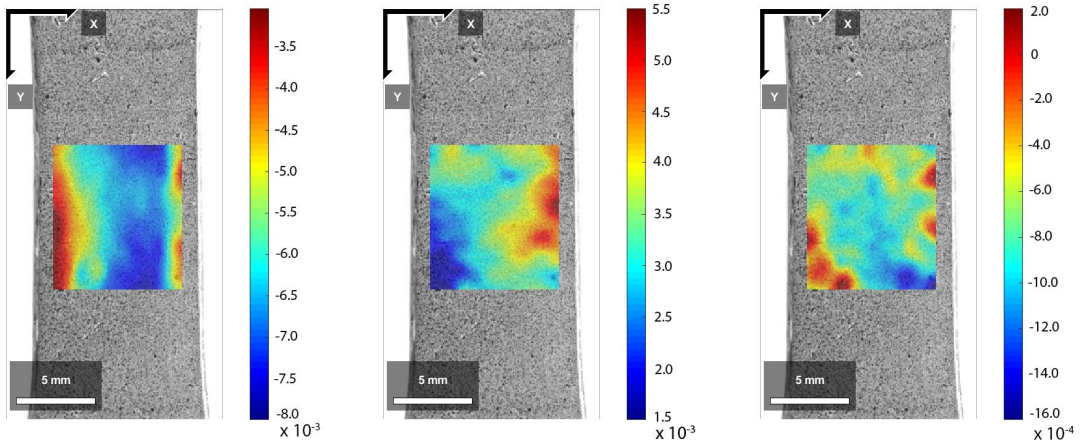

(a) (b) (c)

Figure 4.4: The strain fields for the speckle pattern durability test: (a) ε_{xx}^{Lag} (b) ε_{yy}^{Lag} (c) ε_{xy}^{Lag}

Strain Component	Expected Value	DIC Measurement
ε_{xx}^{Lag}	0	-0.0065±0.0008
ε_{yy}^{Lag}	0	-0.0030±0.0006
ε_{xy}^{Lag}	0	-0.0007±0.0003

Table 4.1: Statistical data for the strain within ROI for pattern durability test. Note that here at the reference configuration, the material is under a stretch $\lambda = 1.2$.

Once the mechanical robustness has been confirmed, the quality of a speckle pattern can also be assessed based on other criteria, as proposed in literature [59] [60] [61] [62]

[63] [64]. However, no single global quantity accurately predicts the quality of the pattern in terms of its ability to yield accurate results [59]. We checked the speckle pattern in a region of interest of about 8.5 ×8.5 mm of a typically prepared specimen. we have carefully computed the histogram, particle size distribution and the mean intensity gradient (MIG) [64].

We first checked the histogram of the speckle pattern. It gives an idea of the grayscale intensity distribution, as shown in Figure 4.5. The histogram shows a Bell-shape distribution. A relative wide spectrum of grayscale values is utilized. There is no sign of under or overexposure.

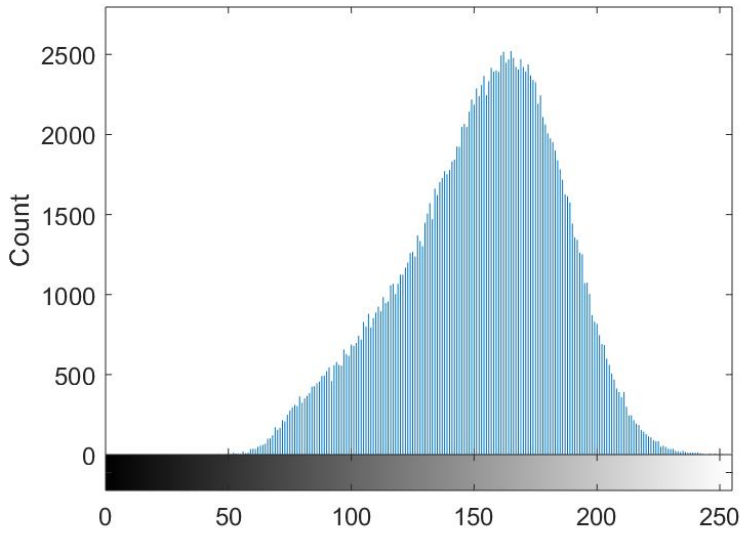

Figure 4.5: Histogram of speckle pattern in a 8.5×8.5 mm region of interest

Besides the grayscale intensity, another aspect to examine is the particle size, as this can be useful to the determination of a proper subset size. We first use the *imbinarize* function in MATLAB to convert the grayscale image into a binary image, as shown

in Figure 4.6. Then the complement image was obtained by flipping 0s and 1s in the original image. To define particles, the connected pixels were tracked by applying *bwlabel* function to this complement image. Then we used the *regionprops* to obtain the equivalent diameters of the particles. As those particles are not exactly circular, the equivalent diameter is defined as the diameter of a sphere that has the same area as the particle. That is, $D_{equiv} = (4A/\pi)^{1/2}$, where A is the area of the particle. The distribution of the equivalent diameter is shown in Figure 4.7. It can be seen that most particles have an equivalent diameter of 1-5 pixels. After averaging all the particles, we obtained an average diameter size in this ROI of 3.8 pixels, which is helpful to avoid aliased effect based on [59].

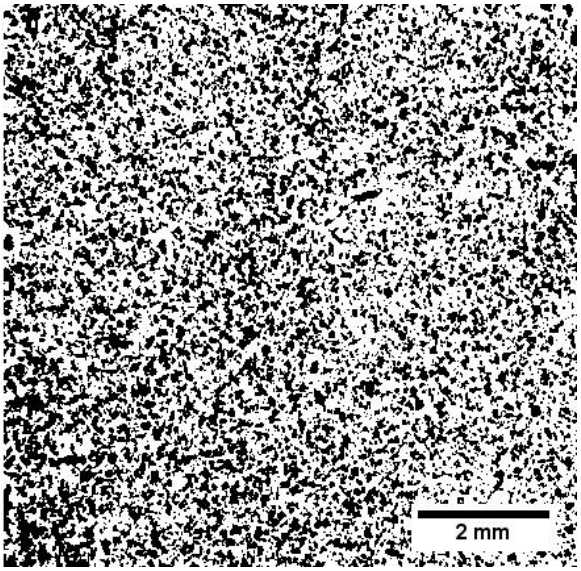

Figure 4.6: Binary image generated from speckle pattern in a 8.5×8.5 mm region of interest

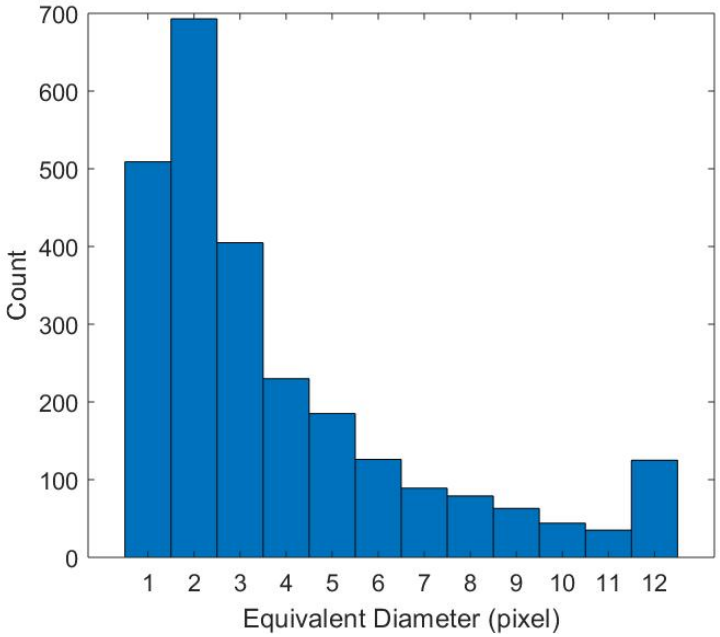

Figure 4.7: The distribution of the equivalent diameter of the particles

The mean intensity gradient (MIG) proposed by Pan et al. is considered as one of the most effective global parameters to assess the quality of the pattern [64]. It was shown that the speckle pattern with a higher MIG tends to introduce smaller standard deviation and bias error. The mean intensity gradient δ_f is defined as:

$$\delta_f = \sum_{i=1}^{W} \sum_{j=1}^{H} |\nabla f(x_{ij})| / (W \times H) \tag{4.1}$$

Where x_{ij} denotes the location of the pixels. W and H are the image width and height in pixels, and

$$|\nabla f(x_{ij})| = \sqrt{f_x(x_{ij})^2 + f_y(x_{ij})^2} \tag{4.2}$$

$f_x(x_{ij})$ and $f_y(x_{ij})$ are the directional intensity derivatives in the x and y direction.

Here we evaluated those two derivatives using a central difference scheme and the computed MIG is 22.2. In Pan's previous work, different speckle patterns from real experiments were examined [64]. The MIG for those patterns were: 34.6, 21.5, 20.0, 12.3 and 9.0. From Pan's work, a larger MIG is preferred. The value of 22.2 obtained is on the larger end of those values, indicating that our speckle pattern has a reasonably good MIG.

4.3.2 Effects of Gel Drying

Drying of the hydrogel can introduce strains. In our study, the PVA dual-crosslink hydrogel dries relatively fast: it lost about 2% of its weight within 10 minutes in our lab environment (about 50% humidity). To test the effects of drying on the strain measurement, a hydrogel specimen with speckle pattern was mounted in the grips and loaded to a stretch ratio of 1.05. A reference image was taken. Then the sample was held in place and images were taken 5, 10, 15 and 20 minutes later. We applied DIC to those images and the corresponding shrinkage strain was obtained from an ROI of about 10 mm $\times$ 8 mm. Theoretically, if the gel does not dry at all, the strain obtained in this way should be due only to the environmental fluctuation and the numerical noise of the algorithm, which should be on the order of 10^{-5} based on our preliminary tests. We calculated the average and standard deviation of the strains in ROI and the values are plotted as a function of time in Figure 4.8. It can be seen that drying induced positive strains in the y direction and negative strains in the x

direction. The magnitude of induced strains increases approximately linearly with time. At a given time, the induced strain magnitude in the y direction is larger in magnitude than in the y direction, as there is less constraint of the specimen in the x direction and the specimen has more freedom to shrink. For the DIC study in this chapter, all the tests can be completed within 10 minutes. The tests show that during this time period, the maximum induced strain due to drying is on the order of 10^{-3}. The goal of this study is to evaluate hydrogel under large deformation (a stretch ratio of $\lambda = 1.5$, corresponding to a Lagrangian strain of 0.625 for uniaxial tension). Thus, the effect of drying on measured strains is negligible relative to the measured strain level.

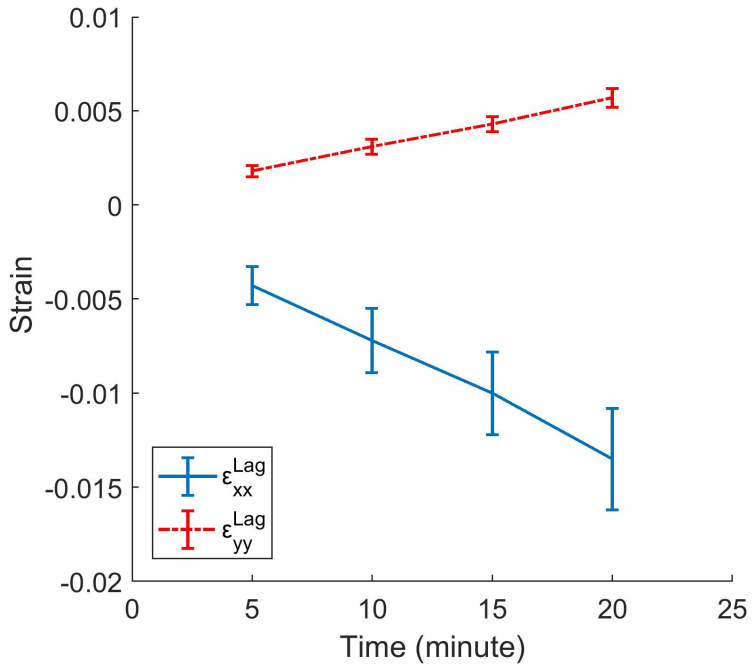

Figure 4.8: The evolution of the induced strains due to drying

4.3.3 Applying In-Plane Rigid Body Translation to Study System Alignment and Lens Distortion

Out-of-plane motion and the non-perpendicularity of the optical axis can introduce errors to the DIC results. The effects of both have been studied separately in [44] [55]. Those effects mostly come from the misalignment of the load frame and the optical system and are often coupled together. We employed in-plane rigid body translation to check the alignment. If misalignment exists, the magnification of the image will not be uniform. As a result, under in-plane rigid body translation, the measured displacement field would exhibit significant non-uniformity and there will be significant strains induced. Meanwhile, lens distortion will also cause a uniform displacement field to appear abnormally non-uniform. Thus. both system alignment and lens distortion can be studied together using in-plane rigid body translation. When applying DIC to in-plane rigid body translation, we expect that the displacement to be nearly uniform and the induced strains to be very small.

In our study, a thin aluminum sample with a speckle pattern prepared identically to the pattern on the gel was clamped to the top grip. A reference image was taken and then the sample was translated vertically (in the -y direction) in 2.5 mm steps to -20 mm. Images were taken at every step and DIC was applied to those images. The displacement fields corresponding to 20 mm translation were shown in Figure 4.9. It can be seen that the U displacements, which ideally should be zero, are within

the range of 0.02 - 0.05 mm. For the V displacement, the maximum variance is 0.04 mm. The average and standard deviation of the induced strains within a 12 × 12 mm ROI were calculated and plotted with respect to translation in Figure 4.10. It can be seen that the induced strains are on the order of 10^{-3}, which is much smaller comparing to our target strain. This error level is the same as what Haddadi and Belhabib obtained in [42]. The results indicate that a good initial alignment of the optical system was achieved, and our lens did not have any significant distortion. As mentioned before, here the effects of both alignment and lens distortion were studied together. In practice, if significant errors are observed, further tests would be needed to determine which effects contribute to the errors.

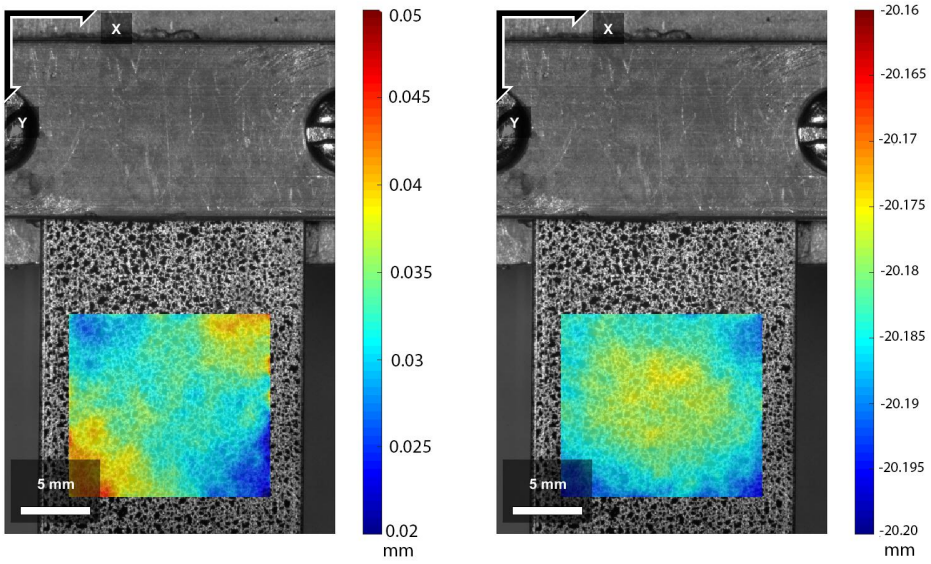

(a) (b)

Figure 4.9: Displacement fields for 20 mm vertical rigid body translation test (-y direction): (a) U (b) V

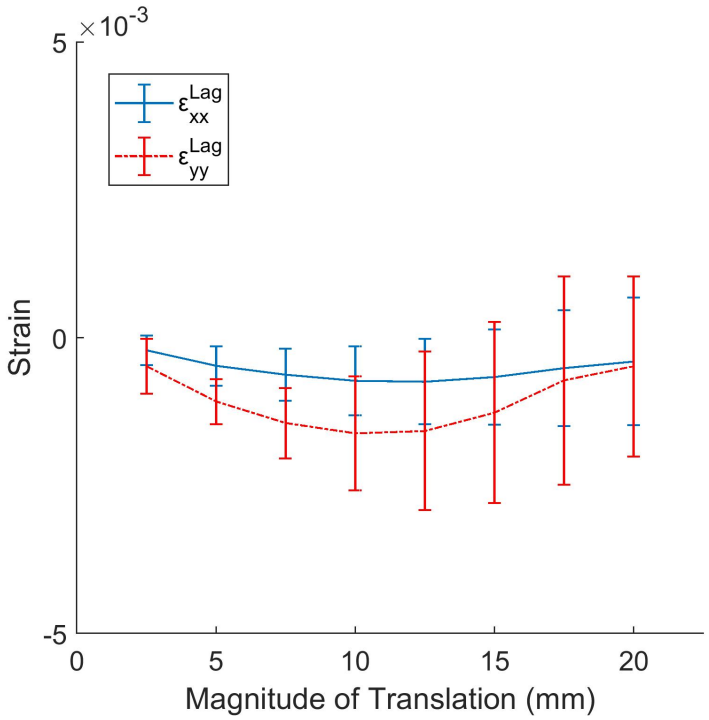

Figure 4.10: The variation of induced strains with in-plane y translation

4.3.4 Application of DIC to Hydrogel under Uniaxial Tension

The results above show that the strain errors from those sources are on the order of 10^{-3}, which is much smaller than the strain level relevant to hydrogels. To test the accuracy of our setup under relatively large deformation, we performed uniaxial tension tests on the hydrogel specimen. The speckle pattern was sprayed on a hydrogel specimen (35 mm gauge length, 12 mm width, 2 mm thickness) using the previously mentioned method. The specimen was loaded to a stretch ratio λ of 1.5 with images were taken at stretch intervals $\Delta\lambda$ of 0.05. The images were analyzed using Ncorr

(subset size: 35, subset spacing: 3, strain radius: 10).

In uniaxial tension, the non-vanishing Lagrangian strains are

$$\varepsilon_{xx}^{Lag} = \varepsilon_{zz}^{Lag} = (\lambda^{-1} - 1)/2, \varepsilon_{yy}^{Lag} = (\lambda^2 - 1)/2 \tag{4.3}$$

For $\lambda = 1.5$, the corresponding strains are $\varepsilon_{xx}^{Lag} = -0.167$ and $\varepsilon_{yy}^{Lag} = 0.625$. The strain fields from DIC are shown color contours in Figure 4.11. It can be seen that the measured strains are very close to the applied strain. From Figure 4.11, at first glance, it might seem that there's a great deal of non-uniformity in the strain distribution. But this impression is primarily due to the color scale of the plot. In order to better understand the strain distribution in the ROI, the average and standard deviation of strains are plotted in Figure 4.12 for five different stretch levels, along with the theoretical results. From Figure 4.12, it can be seen that the average strains in the ROI are very close to the theoretical values, and the strain values in the ROI have a very small deviation. The results indicate that our setup can generate accurate results at the stretch level of 1.5. From the uniaxial tension tests, we also confirmed that grip slippage was not a big problem at the current stretch level. If significant slippage existed, the measured strain in the y direction would be dramatically reduced and deviate from the theoretical value.

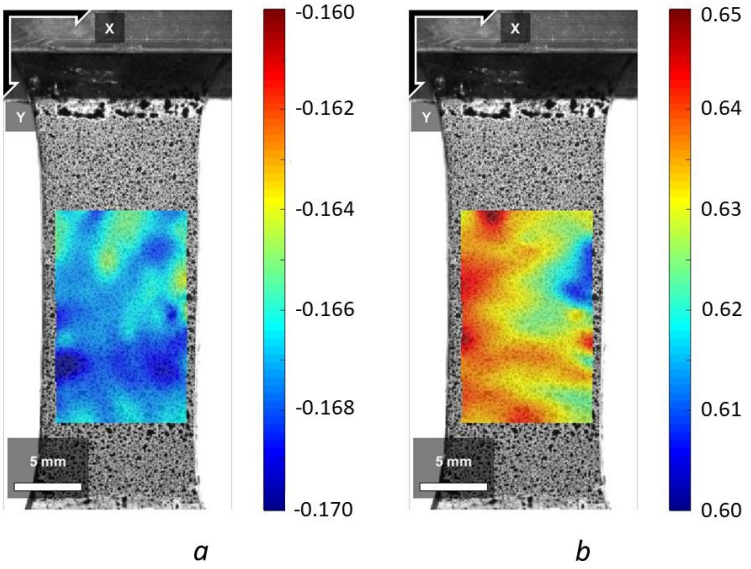

Figure 4.11: The strain fields for the uniaxial tension test: (a) ε_{xx}^{Lag} (b) ε_{yy}^{Lag}

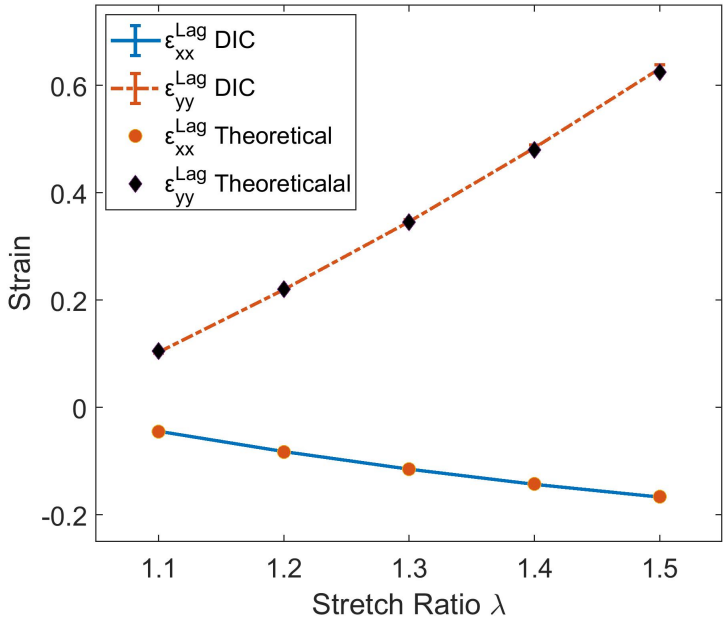

Figure 4.12: Comparison between strains obtained from DIC and theoretical values at different stretch levels. Here the standard deviation is very small, so the error bar is barely visible.

4.4 Application of DIC to Hydrogels with High Strain Concentrations

After the reliability of the experimental setup has been checked, we applied DIC to several hydrogel specimens with strain concentrators. The goal is to test whether the current setup is able to accurately measure deformation with high strain gradients. The DIC accuracy is established through quantitative comparison of DIC results to finite element simulation results. The FEM procedures and corresponding constitutive model has already been validated by detailed comparison of the FEM results to known, asymptotic stress and deformation fields for a plane-stress tensile crack in the hydrogel [16] [17].

4.4.1 Experiment

We applied DIC to hydrogel specimens with three different types of strain concentrators: a 4-mm-diameter center hole, a 5-mm-radius semi-circular edge notch and a 5-mm-horizontal edge crack. The geometries of those specimens are sketched in Figure 4.13. All the specimens are 17.5 mm in width, 2 mm in thickness and 33 mm in gauge length. Specimens of rectangular shapes were first cut from as-made hydrogel sheets using an X-ACTO blade. Then the stress concentrators were made. The center hole and the semi-circular edge notch were made using a 4-mm-diameter and a 10-mm-diameter circular rubber punch respectively. The edge crack was cut

using a single edge blade. Then the specimen was loaded to a nominal stretch ratio of 1.5 at a stretch rate of 0.02/s. Images were taken at a stretch interval $\Delta\lambda$ of 0.05. We used the following parameters: subset size: 30, subset spacing: 2, strain radius: 3. The choice of these parameters is discussed in later section.

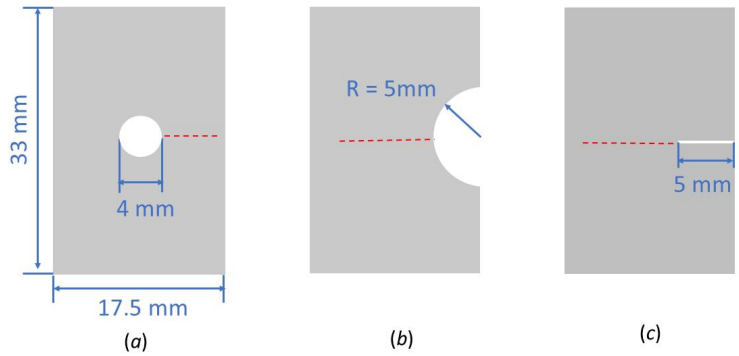

Figure 4.13: Schematic view of the geometries of specimens: (a) circular hole (b) semi-circular edge notch (c) edge crack. The red dashed lines indicate the path on which the strain values from FEM and DIC are compared.

4.4.2 Finite Element Simulation

The finite element simulation was performed by Guo, based on the constitutive model and numerical scheme developed in previous work [14] [16]. Here the procedure is briefly summarized.

The constitutive model, with the fitted material parameters, were implemented in ABAQUS using a plane stress UMAT to calculate the strain fields in the three different geometries shown in Figure 4.13. The material parameters are:

$$\mu\rho = 2.10 \text{ kPa}, \mu\bar{\gamma}_\infty = 8.80 \text{ kPa/s}, \alpha_B = 1.63, t_B = 0.95 \text{ s}$$

Details of the finite element analysis are discussed in [16]. Using the geometries' symmetry, we modeled a quarter of the specimen with geometry in Figure 4.13 (a), and half of the specimens with geometries in Figure 4.13 (b) and (c). The single edge razor blade used to cut the sharp crack in Figure 4.13 (c) has a finite thickness (about 0.1mm), thus the crack tip in this geometry will also have a finite radius of curvature. To account for this finite notch radius, the sharp crack is modeled as a notched crack with a radius of curvature 0.1 mm at the tip, as shown in Figure 4.14 below.

The element sizes are smaller near the notch/crack tip to accurately capture the stress and strain concentrations. The tip element sizes are 0.01, 0.01, and 0.001mm for the three geometries in Figures 4.13 (a) - (c), respectively. These meshes are checked against the analytical and asymptotic results of a neo-Hookean solid. All simulations are carried out using quadratic plane stress elements in static step. Each sample is loaded under constant stretch rate 0.02/s for 25 s until the nominal stretch ratio reaches 1.5.

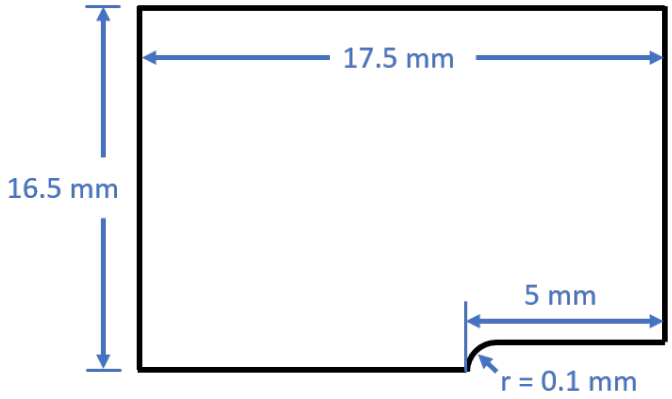

Figure 4.14: Geometry used in FEM for the sharp crack sample. The radius of the notch is exaggerated to show this feature

The nominal strains along the red dashed path defined in Figure 4.13 were extracted.

The nominal strains are defined as

$$\boldsymbol{\varepsilon^N} \equiv \mathbf{V} - \mathbf{I} \tag{4.4}$$

Here $\mathbf{I}$ is the identity tensor, $\mathbf{V}$ is the left stretch tensor, which is related to the deformation gradient $\mathbf{F}$ by $\mathbf{F} = \mathbf{V} \cdot \mathbf{R}^T$, where $\mathbf{R}$ is the rotation tensor. Because the path lies on the plane of symmetry, the x and y directions are the principal directions, so $\mathbf{R} = \mathbf{I}$ and thus $\mathbf{V} = \mathbf{F}$. Along the path of interest, the deformation gradient is related to the nominal strains by

$$\mathbf{F} = \boldsymbol{\varepsilon}^N + \mathbf{I} \tag{4.5}$$

And then the Lagrangian strains can be computed from the nominal strains as

$$\boldsymbol{\varepsilon^{Lag}} = \frac{1}{2}(\mathbf{F}^T\mathbf{F} - \mathbf{I}) = \frac{1}{2}[(\varepsilon^N + \mathbf{I})^T(\varepsilon^N + \mathbf{I}) - \mathbf{I}] \tag{4.6}$$

4.4.3 Results

Comparison between DIC and FEM

The ε_{yy}^{Lag} strain distribution obtained from DIC for three different geometries are shown as color contours in Figure 4.15. These results give a qualitative idea of the strain distribution. Clear strain concentration can be seen near the strain concentrators. To make a more quantitative comparison between strains obtained from DIC and FEM, we extract the strain values for ε_{xx}^{Lag} and ε_{yy}^{Lag} along a path extending from the strain concentrators (the red dashed lines as shown in Figure 4.13) for both FEM and DIC. The corresponding results are compared in Figures 4.16 - 4.18. Note that very near the edges of those strain concentrators, the quality of the speckle pattern is poor. Thus we cannot use DIC to measure the deformation right up to these edges. From those results, it can be seen that there is very good agreement between our FEM simulation and DIC. For the primary loading direction (y direction), DIC was able to capture the sharp change of strains near the stress concentrators and the values obtained from DIC are very close to those obtained from FEM. For the strain ε_{xx}^{Lag}, it seems that the agreement between DIC and FEM is not as good as for ε_{yy}^{Lag}. One reason is that the strains in the x direction are relatively small.

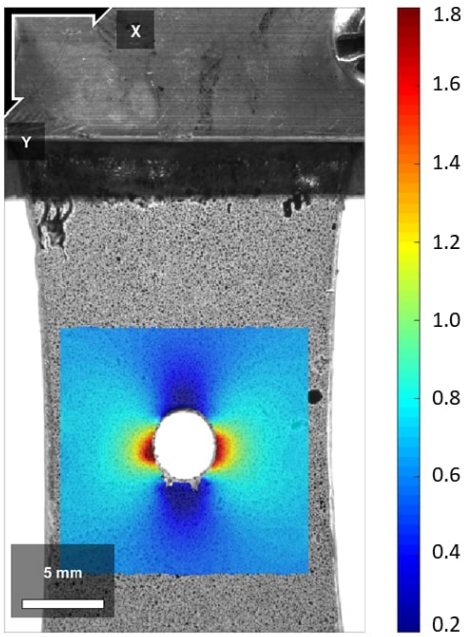

(a)

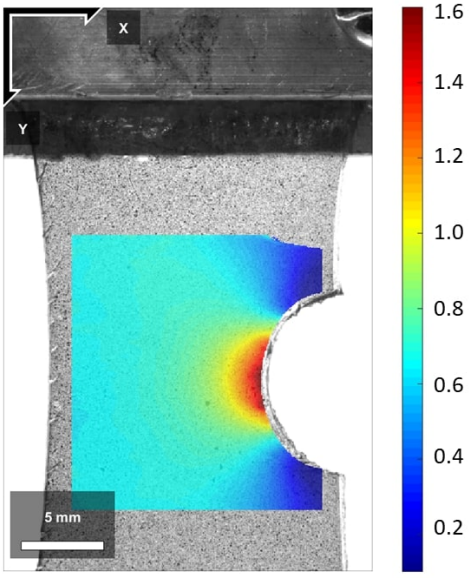

(b)

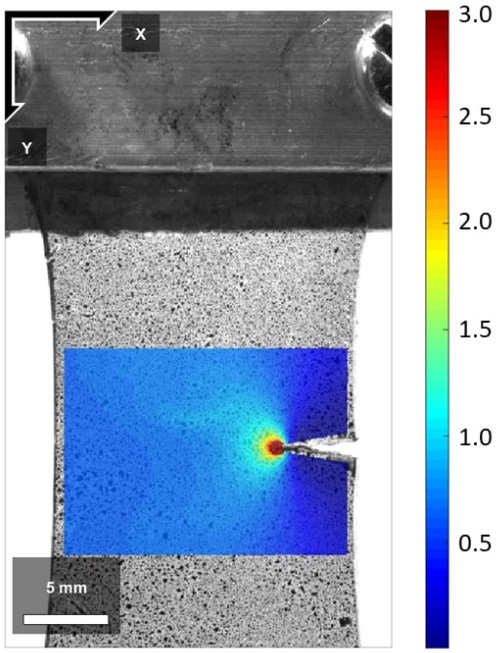

(c)

Figure 4.15: Contour plots of ε_{yy}^{Lag} distribution for different geometries: (a) circular hole (b) semi-circular edge notch (c) edge crack.

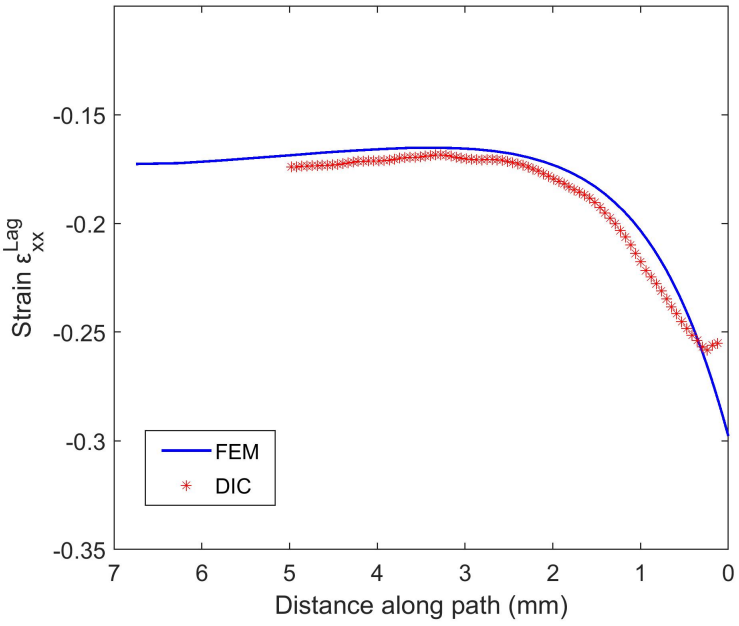

(a)

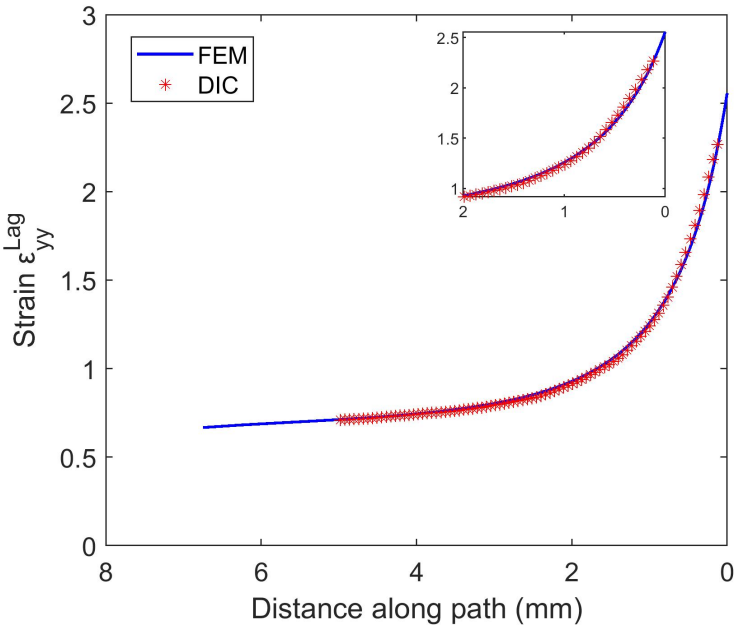

(b)

Figure 4.16: Comparison between the DIC and FEM strains along a line path for the specimen with a 4-mm-diameter circular hole: (a) ε_{xx}^{Lag} (b) ε_{yy}^{Lag}

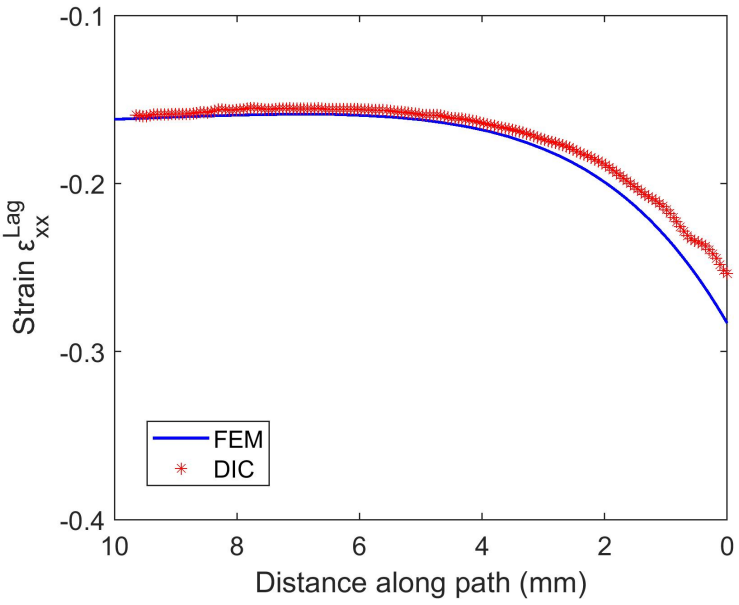

(a)

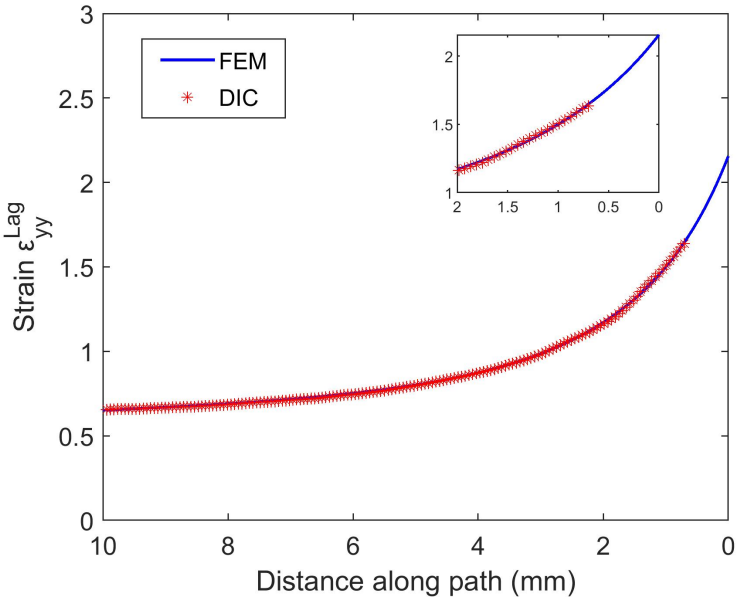

(b)

Figure 4.17: Comparison between the DIC and FEM strains along a line path for the specimen with a 5-mm-radius semi-circular edge notch: (a) ε_{xx}^{Lag} (b) ε_{yy}^{Lag}

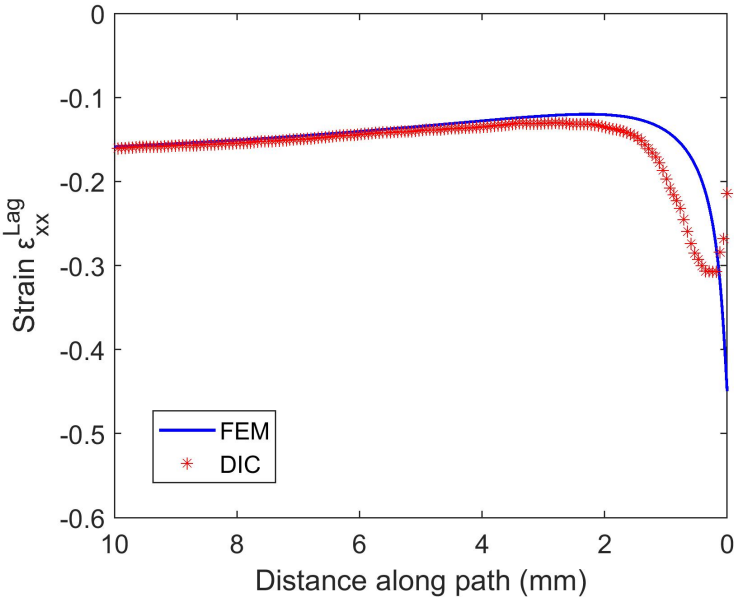

(a)

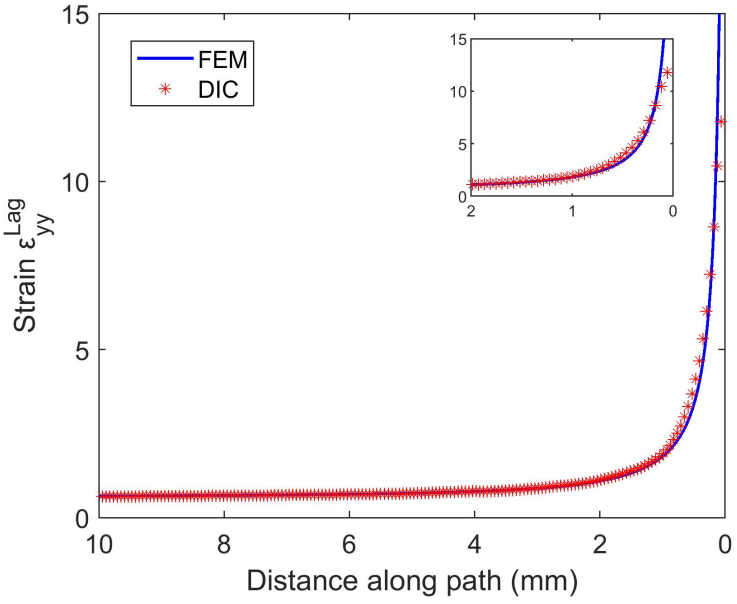

(b)

Figure 4.18: Comparison between the DIC and FEM strains along a line path for the specimen with a 5-mm edge crack: (a) ε_{xx}^{Lag} (b) ε_{yy}^{Lag}

DIC parameters for strain analysis of crack tip fields

Due to the singular nature of the crack tip fields, DIC measurements of strain in this case are particularly sensitive to the DIC parameters. Here the effects of the choice of subset size, subset spacing and strain radius on the strain results are analyzed and discussed. With the parameters used in the previous section (subset size: 30, subset spacing: 2 and strain radius: 3), we are able to obtain DIC results that agree well with the FEM simulation. However, the choice of these parameters requires some thought and analysis.

First, we look at the subset size. Prior works on this topic [62] [65] [66] generally conclude that a larger subset is beneficial to a better correlation, at the cost of losing spatial resolution. A larger subset helps reduce the random error (noise) but can increase systematic error (bias). We processed the images from the edge-cracked sample using five different subset radii: 15, 30, 45, 60 and 75 pixels (with subset spacing of 2 pixels and strain radius of 3 fixed). The resulting ε_{yy}^{Lag} values very close to the crack tip are shown in Figure 4.19 (a). Increasing the subset size decreases the strain singularity measured by DIC. The effect of subset size is significant only in the region very close to the crack tip (about 0.5 mm). Even closer to the crack tip (about 0.1 mm), the theoretical strain is very high and even the smallest subset is unable to resolve this strain. The subset size of 15 is perhaps too small, which leads to an apparent error for the data point closest to the crack tip.

Then we look at the subset spacing. Using a smaller subset spacing increases the

spatial resolution which is critical to capturing the very high localized strain gradient. We tried different subset spacing: 1, 2, 4, 8 and 16 pixels (with subset radius of 30 pixels and strain radius of 3 fixed). For the largest subset chosen, 16, Ncorr failed to generate meaningful results. Thus in Figure 4.19 (b) we compare results only for the first four subset spacings. It can be seen clearly that the measured strain singularity decreases with increasing subset spacing.

The last parameter to discuss is strain radius. Ncorr calculates the strain by computing the displacement gradient. The displacement data are first fit to a planer surface and then the gradient is computed from the fitted planes. Increasing the strain radius means using a larger plane and thus more smoothing effects. The effects of different strain radius are shown in Figure 4.19 (c) (with subset radius of 30 pixels and subset spacing of 2 pixels fixed). Larger strain radii reduce the measured crack tip strains. Based on the above analysis to best capture the singularity of the strain near a crack, small values for subset size, subset spacing, and strain radius should be used, as long as they don't cause correlation problem or produce noisy results.

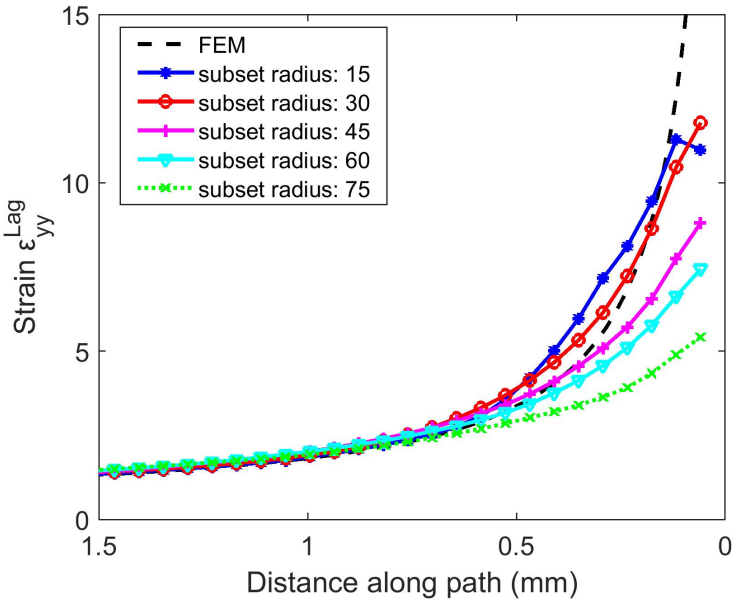
FEM
subset radius: 15
subset radius: 30
subset radius: 45
subset radius: 60
subset radius: 75
Strain ε_{yy}^{Lag}
Distance along path (mm)
15
10
5
0
1.5
1
0.5
0

(a)

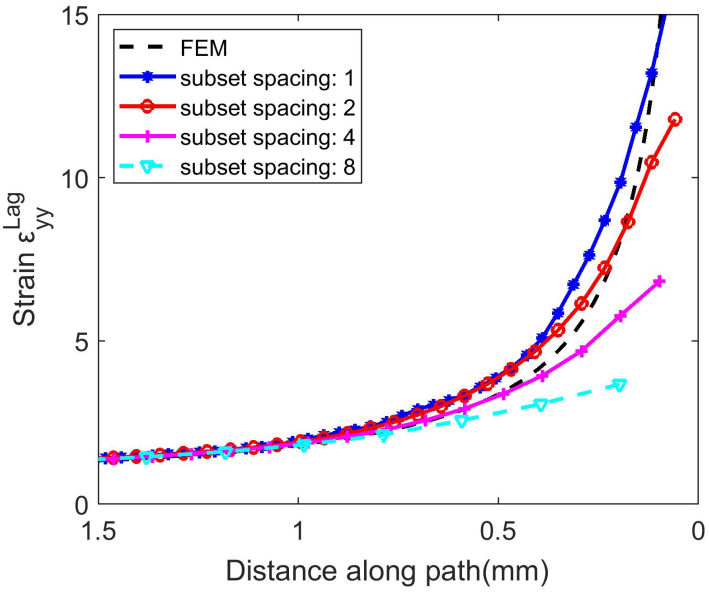
FEM
subset spacing: 1
subset spacing: 2
subset spacing: 4
subset spacing: 8
Strain ε_{yy}^{Lag}
Distance along path(mm)
15
10
5
0
1.5
1
0.5
0

(b)

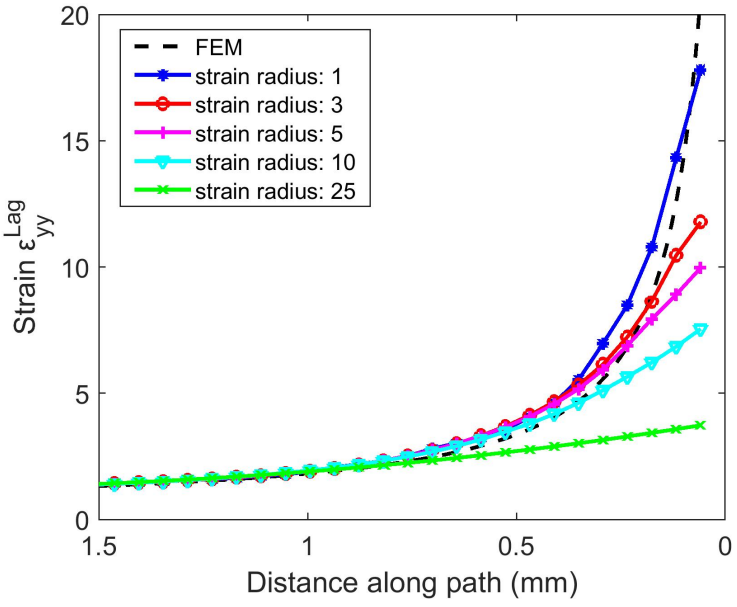

(c)

Figure 4.19: Effects of different DIC parameters on the measured on the measured strain ε_{yy}^{Lag} near the crack tip: (a) subset size (b) subset spacing (c) strain radius

4.5 Application of DIC to Stress Relaxation of Hydrogel with Edge Crack

This PVA dual-crosslink hydrogel is highly viscoelastic. When a specimen is subject to a step displacement, the stress in the specimen decreases with time (stress relaxation). However, for a specimen with an edge crack, it is not clear whether the strain near the crack will also relax with time. In our previous study [16], we argue that the deformation gradient $\mathbf{F}$ at any point is independent of time in a stress relaxation test. Based on this argument, the strain field in a stress relaxation test should also be time independent, even though material shows significant viscoelasticity. In this

section, we experimentally validate this argument, using DIC to map the strain field. A hydrogel specimen with a geometry as in Figure 4.13 (c) was loaded to a stretch ratio λ of 1.3 at a stretch rate of 0.03/s. Then the stretch was held constant at 1.3. We started the image acquisition before the loading starts and images were taken every second for 200 seconds. Then these images were processed using Ncorr, with the following parameters: subset size: 30, subset spacing: 2 and strain radius: 3. In this way the strain distribution in the specimen at different time steps can be obtained. Here we loaded the specimen at $\dot{\lambda} = 0.03$/s instead of a higher stretch rate because a higher stress will be induced at a higher rate, and the specimen might fracture before the target stretch level is reached. However, even the specimen was loaded at slower loading rate, there's still a significant stress relaxation observed. The relaxation of the far-field nominal stress is plotted in Figure 4.20. Here the far-field nominal stress is defined as the force measured divided by the uncracked cross-sectional area (17.5 mm $\times$ 2 mm). From Figure 4.20, the far field stress dropped by about 50% of its initial value after 20 seconds and about 70% after 100 seconds. Although the stress field near the crack tip can't be directly measured, based on the relaxation of the far-field stress, the stress near the crack tip will also experience significant relaxation.

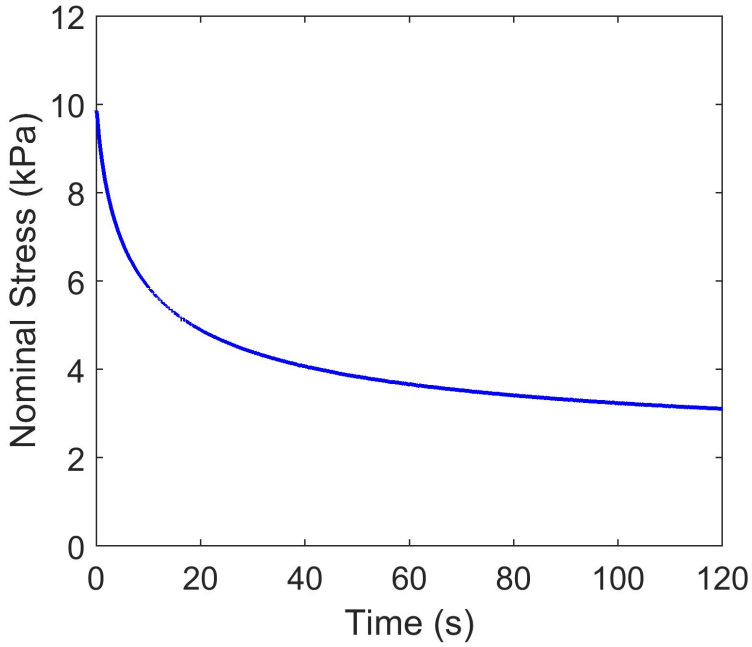

Figure 4.20: The relaxation of nominal stress. Here the starting time t = 0s is when the applied displacement stops increasing (relaxation starts).

Now we look at the evolution of the strain with respect to time during a stress relaxation test. We first look at the strain distribution. We compared the strain field ε_{yy}^{Lag} at time t = 0s (relaxation started) and t = 100s (after 100 seconds of relaxation) in Figure 4.21. From the strain contours in Figure 4.21, it can be seen that there is no perceptible change of ε_{yy}^{Lag} with respect to time. To make a more detailed comparison, we extracted ε_{yy}^{Lag} along the same path as in Figure 4.13. The strain profile at different time steps are plotted in Figure 4.22. From Figure 4.22, it can be seen that the strain remains stationary during the stress relaxation process, consistent with the argument made in [16].

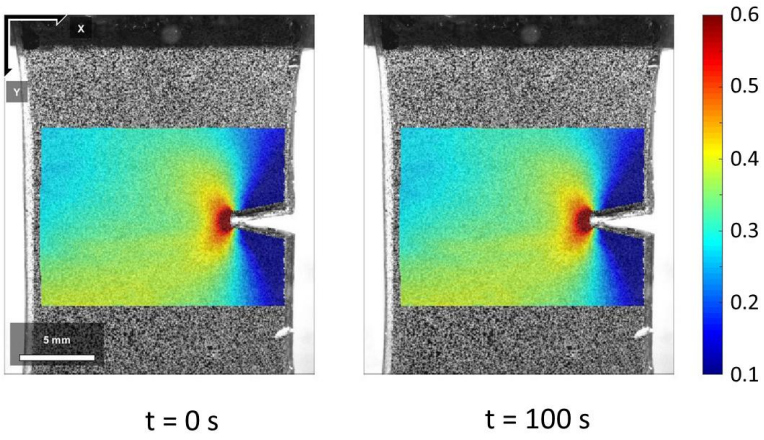

Figure 4.21: The comparison of strain field ε_{yy}^{Lag} at time t = 0s (relaxation started) and t = 100s (after 100 seconds of relaxation)

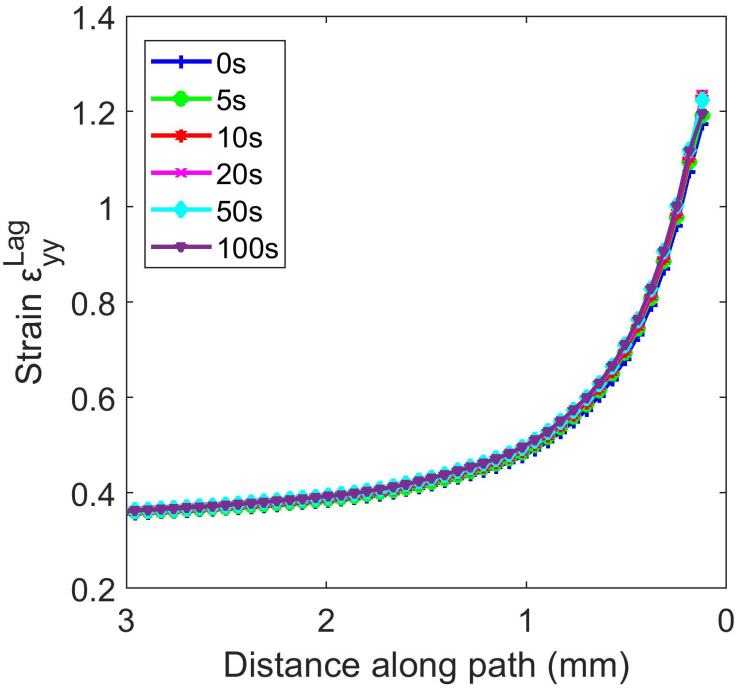

Figure 4.22: The strain along a specific path (Figure 4.13) at different time steps during a stress relaxation test.

4.6 Conclusion

In this study, we applied 2D DIC to measure the deformation of a PVA dual-crosslink hydrogel in the presence of large strain gradients. The details of the experimental setup and several practical issues were discussed. In order to quantitatively validate accuracy, the experimental results were compared with results of finite element simulations based on a large deformation viscoelastic constitutive model developed in prior work. This comparison confirms the accuracy of DIC for measuring the high strain gradient of the specimen in the presence of large deformation. This is relevant for the study of fracture mechanics of such hydrogels. We further show that with a proper selection of DIC parameters, the current method can accurately capture the strain near a crack tip in tension. To better capture the singular strain field, smaller values for subset size, subset spacing and strain radius should be selected. Once the accuracy of the method was carefully validated, we used DIC to study the evolution of the crack tip strain field during a stress relaxation test. The results show that despite the stress relaxation, the strain field remains stationary.

CHAPTER 5

STUDY OF THE CRACK PROPAGATION: CRACK TIP FIELDS MEASURED USING DIGITAL IMAGE CORRELATION

5.1 Introduction

In Chapter 4, we applied DIC to study the deformation near a static crack. To fully understand fracture both the initiation and growth of cracks should be considered [67], [68], [69]. To our knowledge, there are no detailed studies on the application of DIC to crack propagation in a hydrogel or similar material. In addition, when testing some hydrogels, specimens may be immersed in water or oil in order to maintain hydration [20], [21] [23] [49]. The liquid could interfere with the speckle pattern and the window through which the specimen is imaged could distort the optical path, causing systematic errors. In addition to the above hydrogel specific issues, the accuracy of the strain measurement in any application needs to be established.

The goal of this paper is to conduct a systematic study of the application of DIC

to crack propagation in a hydrogel, and to provide a practical guide for researchers studying similar problems. In the following, issues such as the assessment of the speckle pattern, details of the optical setup, and validation of the crack tip strain measurement will be discussed in the case of hydrogel samples immersed in oil. We then apply DIC to study the crack propagation. From the DIC results, we demonstrate that for this PVA dual-crosslink hydrogel the crack grows at a steady state. When the crack is propagating rapidly, the material ahead of the crack tip is being loaded at a high strain rate (on the order of 10 s^{-1}). We discuss the experimental methodology in Section 2. Section 3 focuses on validating the accuracy of the experimental measurements. In Section 4, we discuss the application of DIC to measure the strain induced by a propagating crack. The work is summarized in Section 5.

5.2 Experiment

5.2.1 Load Application

The way we applied load in this study was very similar to what we did in Chapter 4. The only difference is that the specimen was immersed in the oil instead of in the air. The details of the oil container was shown in Chapter 2.

5.2.2 DIC Setup

The way to prepare the speckle pattern and the software used in this study are exactly the same as Chapter 4. However, a different camera was used. We used a CMOS camera (FLIR Blackfly S 3.2MP B&W) with the same telecentric lens in Chapter 4 (Edmund Optics, SilverTL 0.16×). This camera and lens combination yields a spatial resolution of 0.0215 mm per pixel. The camera can acquire images at a maximum rate of 118 fps, which allows us to keep track of the fast crack propagation (about 50 to 100 mm/s). The complete set up is shown in Figure 5.1

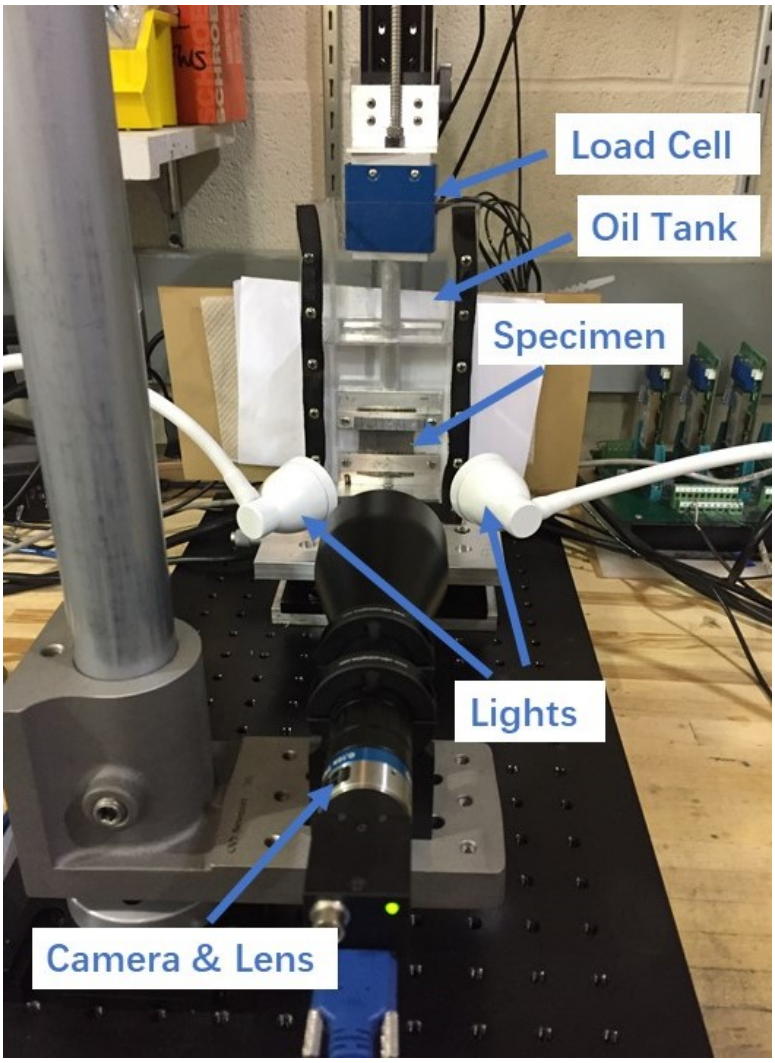

Figure 5.1: Experimental setup: the custom tensile tester and image acquisition system for DIC

5.3 Validation of the System

Before applying DIC to measure the strain field involving a propagating crack, it is important to validate the accuracy of the measurement. There are several possible issues that might affect the DIC results, including the quality of the speckle pattern,

the alignment of the test setup, lens distortion, sample slippage and the selection of DIC parameters. In Chapter 4, we systematically studied those issues when testing the hydrogel in air. However, there are additional issues introduced when the specimen is immersed in oil. As we are imaging through mineral oil and a PMMA window, it is important to verify that the oil and PMMA sheet do not distort the optical path and that the oil does not damage the speckle pattern on the specimen. In this section, we will use several simple calibration tests to validate the accuracy of measurements performed with this setup.

5.3.1 Durability of the Speckle Pattern

To validate that the speckle pattern is mechanically robust in the oil when the specimen is subject to large deformation, we preloaded a specimen to a stretch ratio $\lambda = 1.1$ and acquired a reference image. Then we loaded the specimen in oil from $\lambda = 1.1$ to $\lambda = 1.6$ at a loading rate $\dot{\lambda} = 0.05/\text{s}$ and unloaded to the stretch of 1.1. This loading and unloading was repeated for ten cycles. Then a second image was taken after the last cycle, at $\lambda = 1.1$ (current image). We carefully examined the images of the speckle pattern of the reference and current images. Figure 5.2 shows the speckle pattern of a 5×5 mm region of interest in the reference and current images. A careful examination of Figure 5.2 indicates that there is no significant change of the speckle pattern even after the specimen was subject to ten cycles of large deformation in oil.

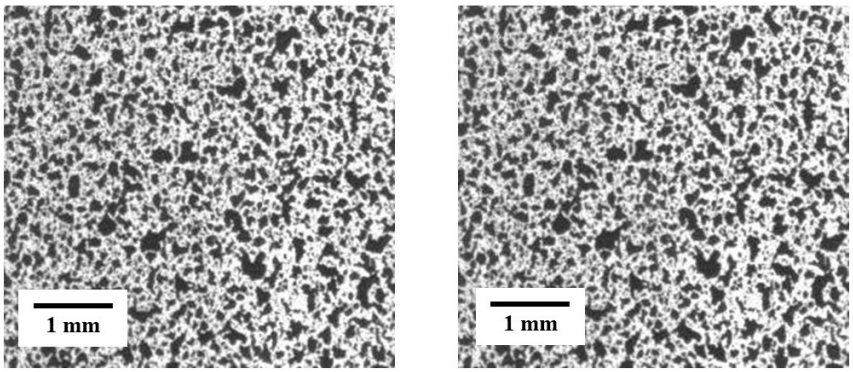

(*a*) (*b*)

Figure 5.2: A close-up view of speckle pattern in a 5 × 5 mm region of interest. (a) reference image: taken before loading (b) current image: taken after the ten cycles of loading from $\lambda = 1.1$ to 1.6.

To further validate the durability of the speckle pattern, we used DIC to analyze the apparent deformation between the reference and current images. The following parameters were used in Ncorr: subset radius: 40 pixels, subset spacing: 4 pixels and strain radius: 10. This set of parameters were also used for Section 3.2. We didn't experience any correlation issue when processing those two images. The resulting displacement and strain fields in the loading direction (y direction) are shown in Figure 5.3, where it can be seen that the induced displacement was very small, on the order of 10^{-2} mm. The displacement fields did not show any irregular pattern. The apparent strain induced by the cyclic loading is on the order of 10^{-3}, which is much smaller compared to the strain we will apply in the fracture experiments. The induced displacement and strain in the x direction are of the same magnitude as those in the y direction, which are not shown here. These results indicate that

the ink-sprayed speckle pattern is robust enough for application to the study of crack growth for immersed gels.

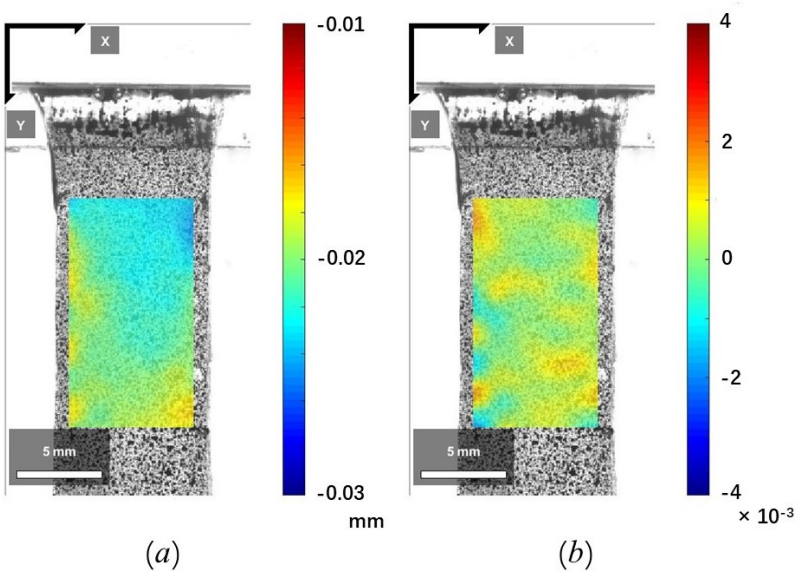

Figure 5.3: The induced displacement and strain after ten cycles of loading of the specimen in oil: (a) y - direction displacement, V (b) y - direction strain, ε_{yy}^{Lag}

5.3.2 Assessment of Optical Distortion Using Rigid Body Translation

Optical distortion can introduce artificial effects into the strain measurement. For our application, there are three possible sources of distortion: the lens, the PMMA window and the oil. The telecentric lens used here has a very small distortion and thus the effects of lens distortion should be minimal as we will show below. Careful attention needs to be paid when other lenses are used; non-negligible distortion errors may be induced and should be corrected for [43] [70] [71].

When the specimen is submerged, the mineral oil and the PMMA plate are in the optical path, deflecting the light emitted by the specimen. This effect on the strain measurements needs to be taken into account. One effect would come from random variations in the PMMA and mineral oil optical properties, for example the sheet thickness or any temperature variations in the oil which might affect its index of refraction. Another effect would be misalignment of the sample to the PMMA window. The magnitude of the apparent strain, $\Delta\varepsilon$, due to misalignment is given by [72]

$$\Delta\varepsilon = \frac{tan\,\theta sin[\theta - sin^{-1}(\frac{n_{air}}{n_{oil}} sin\,\theta)]cos\,\theta}{cos[sin^{-1}(\frac{n_{air}}{n_{oil}} sin\,\theta)]} \tag{5.1}$$

where n_{air} and n_{oil} denote the refractive index of air and oil respectively, and θ denotes the angle between the specimen plane and PMMA plate in the direction of interest. Based on 5.1 and taking $n_{oil} = 1.48$, for $\theta \leq 3$ degrees, the apparent strain $\Delta\varepsilon < 10^{-3}$. Thus although the specimen must be fairly well aligned with the PMMA window, a few degrees of misalignment will not be of concern in hydrogels where the strains that are of interest will be on the order of 10^{-1} and larger.

The above assumes that the mineral oil is optically homogeneous, i.e., the refractive index is constant for the oil in the tank. It is important that the oil is clear, contain few air bubbles and it should be at rest and at uniform temperature. If the oil is not optically homogeneous, it will distort the optical path and may introduce additional and unpredictable errors into the strain measurement.

We use in-plane rigid body translation to validate that the system is free of significant

distortion. We expect uniform displacement field and zero strain from in-plane rigid body translation. However, if significant distortion exists, the measured displacement field would be distorted, exhibiting significant non-uniformity and hence significant induced strains. To test our setup, we prepared a speckle pattern on a thin glass slide. The slide was then submerged in mineral oil. We translate the slide in the vertical (-y direction) by 15 mm. Images were acquired at 2.5 mm intervals, then analyzed using Ncorr. The measured y-direction displacement V and strain ε_{yy}^{Lag} corresponding a vertical translation of -15 mm are shown in Figure 5.4. It can be seen that the measured displacement is uniform to within ± 0.05 mm, or about 2 pixels. We found that all apparent strains are on the order of 10^{-3}, which is negligible compared to the strain levels applicable to deformation of hydrogels. The pattern of non-uniformity in the displacement is characteristic of spherical lens distortion [71] [43] suggesting that any distortion from oil and PMMA window are negligible relative to the lens. The results confirm that this system is free from optical distortions that would cause strain errors that are significant relative to the expected strains. In the case of stiff materials in which strains to failure would be on the order of 10^{-2} or smaller, the distortions should be calibrated and accounted for in the DIC analysis [70].

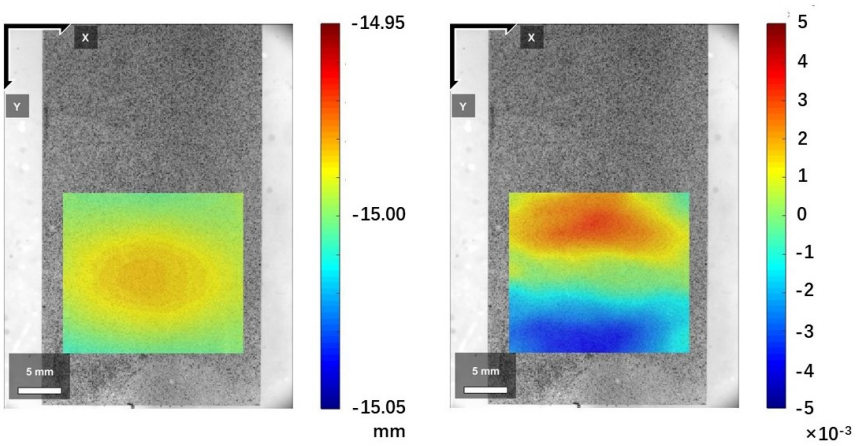

(*a*) (*b*)

Figure 5.4: The induced displacement and strain by the rigid body translation of -15 mm in the y direction: (a) y - direction displacement, V (b) y - direction strain, ε_{yy}^{Lag}

5.3.3 Validation of the Accuracy in Crack-Tip Strain Measurement

Before applying DIC to measure the deformation fields near a propagating crack, its accuracy in applications involving high strain gradient and large deformation must be established. Here we applied DIC to measure the strain field near a static crack. The geometry of the specimen is sketched in Figure 5.5 (a). The specimen was loaded to a stretch ratio of $\lambda = 1.5$ at a loading rate of $\dot{\lambda} = 0.02/\text{s}$. The specimen was immersed in mineral oil during the test and images were taken at a stretch interval of $\Delta\lambda = 0.05$. Images from each $\Delta\lambda$ interval were processed using Ncorr. From Chapter 4, in order to capture the high singularity of crack-tip strain, small values for subset size, subset spacing, and strain radius should be used, as long as this does not result in

poor correlation or produce noisy results. Thus we used the following parameters: subset radius: 25 pixels, subset spacing: 1 pixel and strain radius: 2.

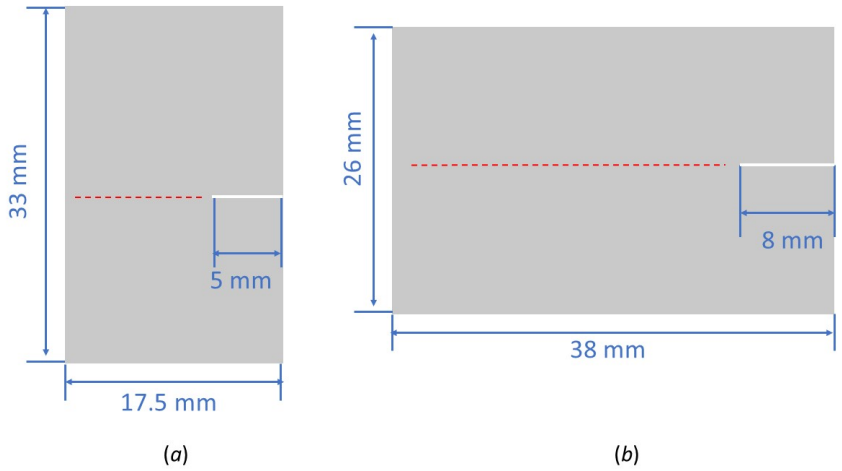

Figure 5.5: Geometry of the specimens for the DIC measurement (a) static crack (b) crack propagation. The red dashed line indicates the path where the strain values will be extracted.

As this PVA hydrogel exhibits viscoelastic behavior, an analytical solution for the crack tip strain is not available. In order to make a quantitative validation, we calculated the strain fields using FEM in ABAQUS, with a constitutive model and a numerical scheme developed in prior work [14] [16] [17]. Prior work has shown that the simulation accurately predicts the crack profile under large deformation, and that the calculated stress is consistent with the corresponding asymptotic fields.

The ε_{yy}^{Lag} field obtained from DIC is shown in Figure 5.6 (a). It can clearly be seen that the strain is highly concentrated near the crack tip. To make a more detailed comparison, we examined the strain along a line extending from the crack tip, as indicated by the red dashed line in Figure 5.5 (a). We extracted the strain from

both FEM and DIC. The comparison is shown in Figure Figure 5.6 (b). From Figure Figure 5.6 (b), there is a good agreement between DIC and FEM. DIC was able to capture the strain behavior in the region as close as 0.1 mm to the crack tip, where the strain is about 800%.

5.4 Study of the Crack Propagation Using DIC

After validating the DIC setup in measuring the deformation near a static crack, we applied DIC to study crack propagation of this PVA dual-crosslink hydrogel. We use DIC to show that at a slow stretch rate of 0.005/s, crack propagation occurs in a nearly steady state meaning that the crack opening, stress and strain fields near the crack are invariant with respect to an observer moving with the crack tip [73].

5.4.1 Experiment

The dimensions of the test specimen for the crack propagation test are shown in Figure 5.5 (b). We used a wider specimen so that the crack has enough distance to reach and grow at steady state before its propagation is affected by the free edge of the specimen. We loaded the specimen at a stretch rate of 0.005/s until it completely fractured. Images were acquired every 2 seconds before the crack propagation. When crack propagation started, images were taken at a higher rate of 100 fps. At this framing rate, we were able to keep track of the crack during its fast propagation. The exposure time was set to 1 ms. A longer exposure time might result in blurred

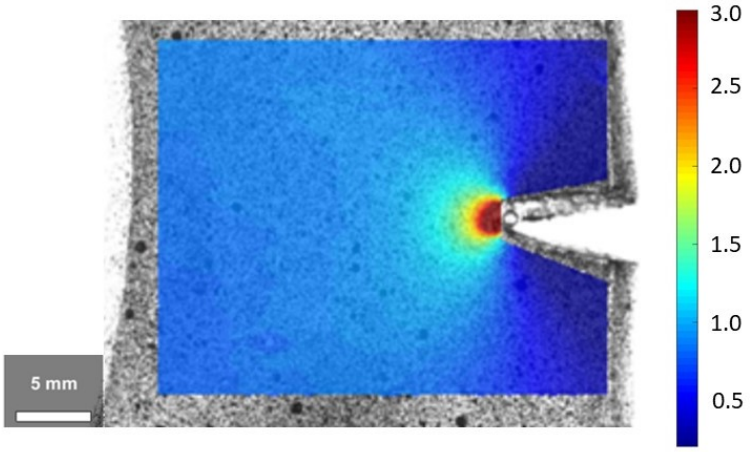

(a)

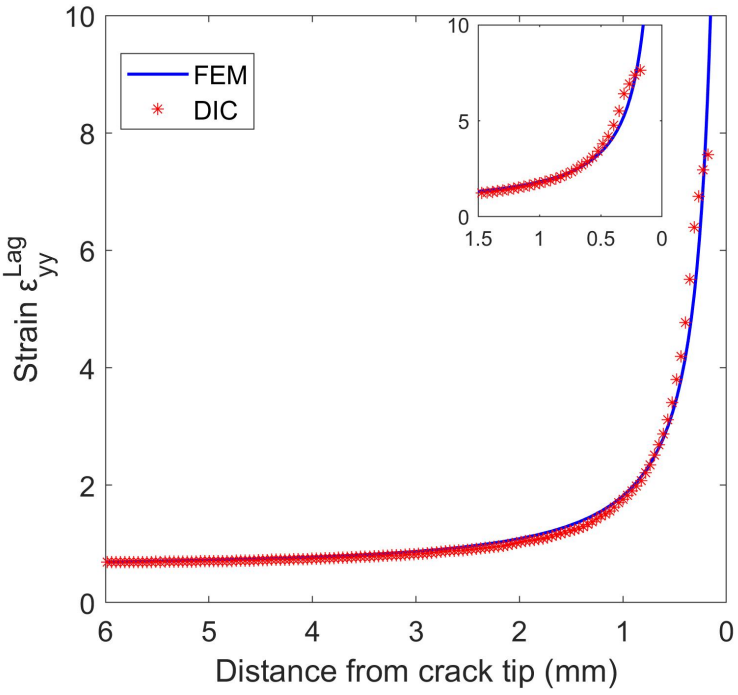

(b)

Figure 5.6: Results of the DIC strain measurement of an edge-crack specimen (a) distribution of ε_{yy}^{Lag} (b) comparison between DIC and FEM along a path (red dashed line in Figure 5.5 (a))

images, as the crack is growing at about 0.05 mm/ms, corresponding to roughly two pixels during the exposure time.

The acquired images were analyzed using Ncorr, with the following parameters: subset radius: 25 pixels, subset spacing: 1 pixel and strain radius: 2. As the specimen experienced large deformation, when processing the image at current time t, we used all the previous images taken before t. Ncorr updates the reference image based on the quality of the correlation. We performed three repeats for the crack propagation study and found that the crack propagation behavior is consistent. Here we present the results from a single test.

5.4.2 Results

We first consider how the crack shape evolves. Figure 5.7 shows the crack profile at different time steps. When the material is being loaded at a relatively slow loading rate ($\dot{\lambda} = 0.005/\text{s}$), the crack shows significant blunting behavior prior to fracture. Then a new crack nucleates at the tip of the pre-existing crack, where there is a very high stress concentration [17]. Once this new crack is initiated, it propagates rapidly and with a sharp profile. During the propagation of this new crack, the original crack remains blunt. As the gel is viscoelastic, it takes some time for it to relax to original shape upon unloading. Crack extension is plotted against time in Figure 5.8. The crack growth is approximately linear in time with a crack speed of approximately 50 mm/s. It took about 0.6 s for the crack to propagate across the specimen.

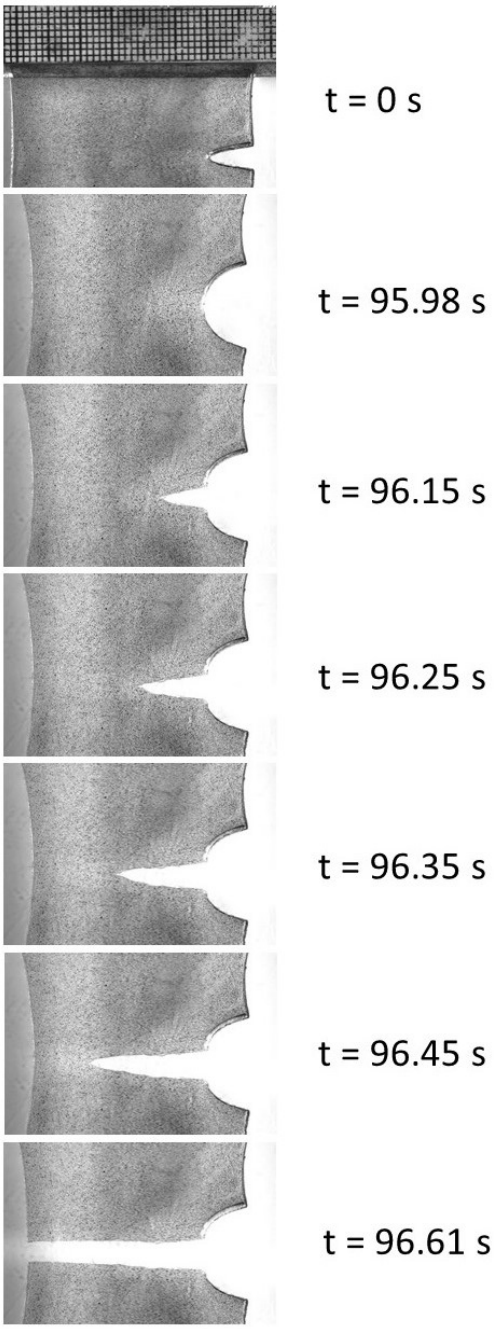

Figure 5.7: Evolution of the crack profile at different time steps. t = 95.98 s is the instant just before the crack started to grow.

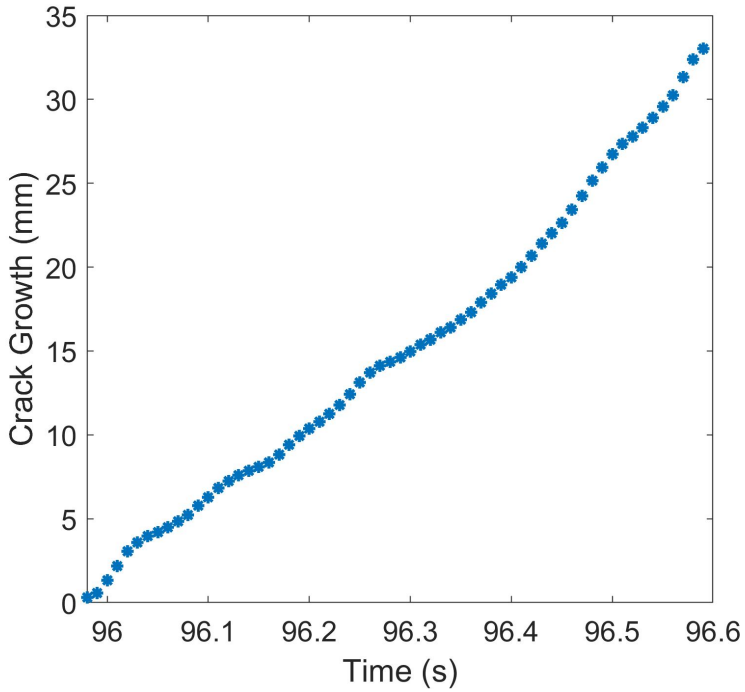

Figure 5.8: Crack growth as a function of time. The crack length is mapped back to the initial configuration. The estimated precision of the crack length measurement is 0.1 mm.

To further study the characteristics of the propagating crack, we considered the profile of the propagating crack. From Figure 5.7, it can be seen that the crack propagates in a self-similar manner, that is, the crack profile appears to be invariant with respect to the moving crack tip. To confirm this, an edge finding algorithm was used to extract the profile of the propagating crack at three different time steps, t = 96.15 s, 96.25 s and 96.35 s. The profiles were translated to a common crack tip and are shown in Figure 5.9 (a). The overlap of these profiles shows that the propagating crack grows with a self-similar shape.

We also used DIC to obtain the strain induced by the propagating crack at those

three steps. We extracted ε_{yy}^{Lag} along a horizontal line extending from the tip of the moving crack, and then translate the results from different time steps so that they have the same crack tip. The corresponding results are shown in Figure 5.9 (b). As can be seen Figure 5.9 (b), the strain ahead of a moving crack also has self-similar behavior. This further confirms that the crack propagation is steady state. In Figure 5.9 (b), we also plotted the strain ε_{yy}^{Lag} ahead of the static crack (t = 95.98 s, just before the initiation of the new crack). The strain level corresponding to the original crack is much higher and compared to the propagating crack it affects a larger region in front of the crack tip.

Using DIC, we can also track of the evolution of the strain fields. Here we examine the evolution of ε_{yy}^{Lag} for different material points during the crack propagation, as shown in 5.10 (a), with O denoting the tip of the pre-existing crack in the reference configuration. We first examine points A, B and C. Those three points lies on a line approximately 1.5 mm above the crack plane in the reference configuration, with a horizontal spacing of 5 mm between them. The strain averaged over a small region of 0.2 mm $\times$ 0.2 mm is shown in 5.10 (b). Note that the strain drops as the crack propagates past the material points. The initial stage of the strain drop was almost linear with time with a strain rate of about -1.5 s^{-1}. The strain rate slowed down after this fast initial stage. By the time the specimen was completely fractured, there was still some residual strain in those material points. The initial fast drop in strain represents the instantaneous elastic response of the viscoelastic material while

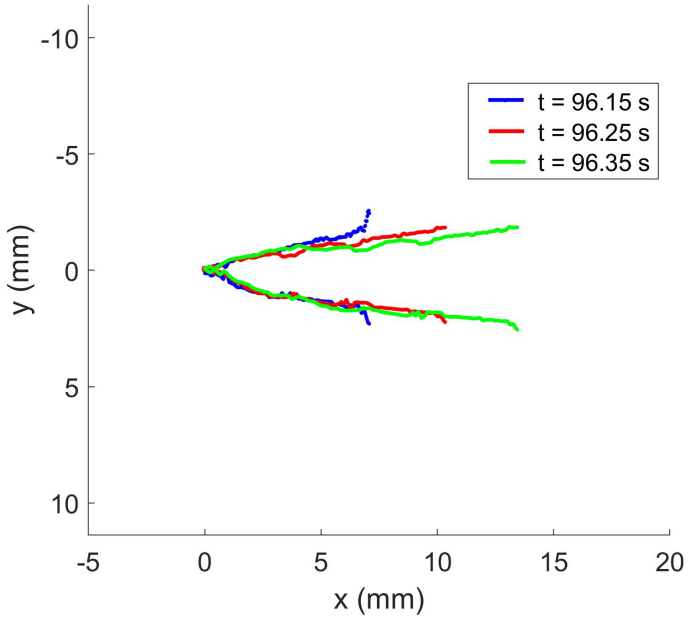

(a)

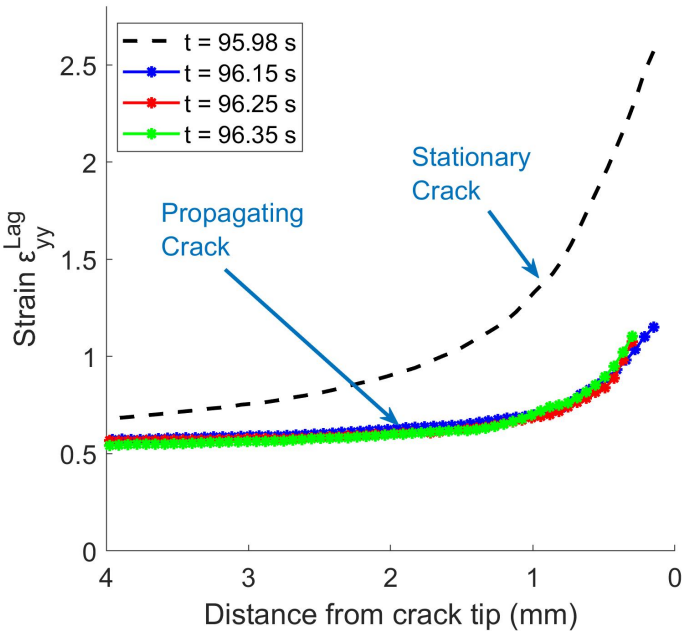

(b)

Figure 5.9: Behavior of the propagating crack: (a) the crack profile at three different time steps (b) the strain ε_{yy}^{Lag} along a path ahead of the propagating crack. The results show that the crack propagates in a self-similar manner.

the slower strain reduction represents the viscoelastic creep recovery of the hydrogel. Based on previous observations, it takes several minutes for the material to completely recover once the stress has been reduced to zero.

From Figure 5.10 (b), it is also seen that the strain history during crack propagation is similar at each of the three points. We shifted the curves corresponding to points B and C to that of point A, and those three curves mostly overlap. The amount of shift was 0.1 s and 0.2 s for point B and C respectively, which is equal to the time it took for the crack to propagate from A to B and C (the average crack speed is 50 mm/s). In other words, the material points B and C will also experience the same deformation history as A, despite a delay. This again confirms self-similarity during crack propagation.

We also examine the loading history of points located in the crack plane. We plotted the evolution of ε_{yy}^{Lag} for points O and D in Figure 5.10 (c). From Figure 5.10 (c), it can be seen that for point O, which is very close to the tip of the pre-existing crack, ε_{yy}^{Lag} increases approximately linearly with time, expect for the very early stage of loading. We fitted ε_{yy}^{Lag} vs. time (excluding the first 10 data points) and obtained a strain rate $\dot{\varepsilon}_{yy}^{Lag}$ of 0.029 s^{-1} for the stationary crack Point D lies far away from the pre-existing crack. When the specimen was being loaded, before the crack propagated, ε_{yy}^{Lag} also increased linearly with time, at a rate $\dot{\varepsilon}_{yy}^{Lag}$ of 0.0062 s^{-1}. The strain level was much lower compared to that of point O. However, the strain increased dramatically as the crack approached point D. The inset in Figure 5.10 (c) shows the details of the strain

evolution of point D when the crack was propagating. From the last two data points, we can estimate a maximum measured strain rate $\dot{\varepsilon}_{yy}^{Lag}$ of about 40 s^{-1}. This rate is much higher than the loading rate of point O. This helps explain one phenomenon: the moving crack can keep propagating even when the crack tip strain is much lower comparing to that of a static crack. In previous studies, it has been shown that this PVA dual-crosslink hydrogel is rate dependent, the higher the loading rate is, the higher the stress is [12] [14] [19]. When the material is loaded at a higher strain rate, it fractures at smaller strain compared to being loaded at a lower strain rate [28] [34]. Thus, even though the strain level in front a propagating crack is lower compared to that of a static crack, the very high strain rate induced by the rapidly propagating crack causes high stresses in the material, driving crack propagation.

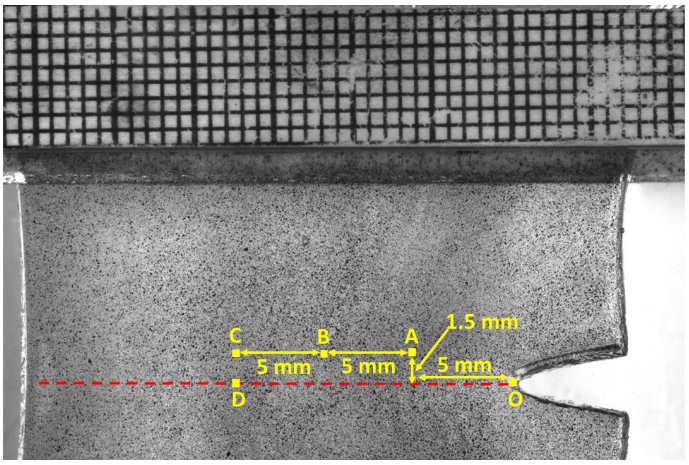
C
B
A
1.5 mm
5 mm
5 mm
5 mm
D
O

(a)

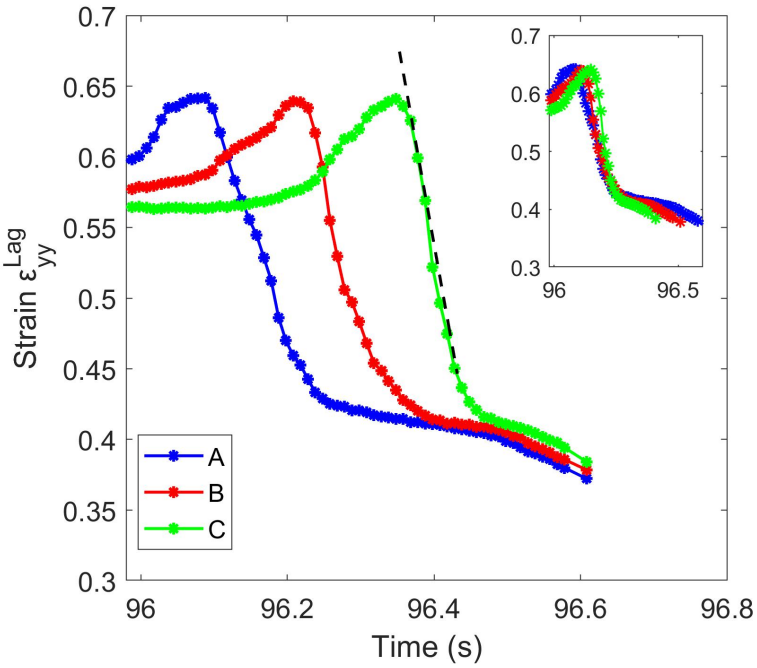
Strain ε_{yy}^{Lag}
Time (s)
A
B
C
0.7
0.65
0.6
0.55
0.5
0.45
0.4
0.35
0.3
96
96.2
96.4
96.6
96.8
0.7
0.6
0.5
0.4
0.3
96
96.5

(b)

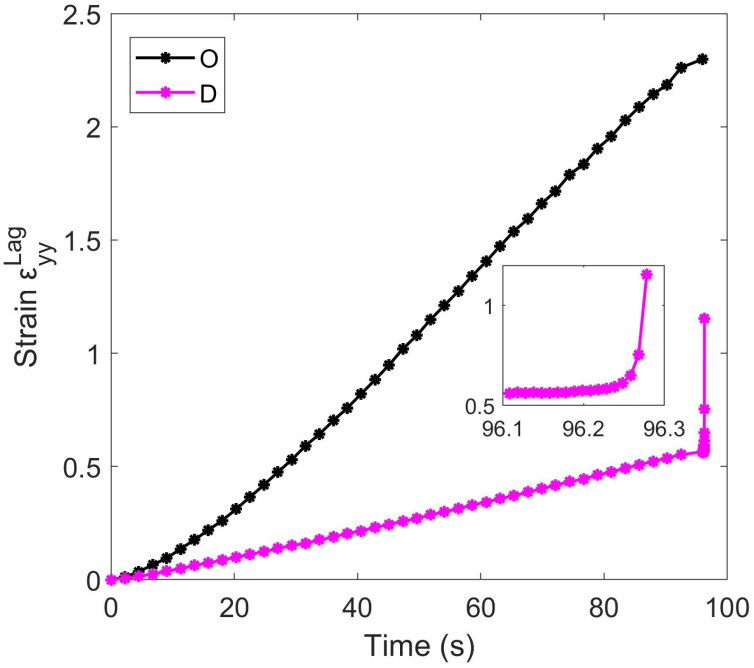

(c)

Figure 5.10: The evolution of ε_{yy}^{Lag} of different material points during the crack propagation: (a) The location of material points O, A, B, C and D on the specimen (b) The strain history of A, B and C during the crack propagation. The inset shows that the curves for B and C can be shifted to that of A, with shifts of 0.1 s and 0.2 s. (c) The strain history of O, D. The inset shows the details of ε_{yy}^{Lag} evolution as the crack approaches point D

5.5 Conclusion

In this study, we applied 2D digital image correlation (DIC) to study crack propagation behavior of a PVA dual-crosslink hydrogel. We performed DIC when the specimen was immersed in oil. Practical issues such as the preparation of the speckle pattern and the methods to validate the system accuracy were discussed. We carefully established the accuracy of DIC in measuring the crack tip strain, even when

immersed in oil. By using small values for subset size, subset spacing and strain radius, DIC can accurately capture the high-strain gradient near the crack tip. After validating the accuracy of DIC, we applied it to study crack propagation. A new crack initiated in at the tip of the existing, blunted crack, and then propagated rapidly. We compared the strain in front of the propagating crack at different time steps, and also checked the deformation history of selected material points. The results show that the deformation fields are invariant with respect to an observer moving with the crack tip. This indicates that the crack propagation reaches steady state. The results also show that the strain level ahead of a propagating crack is lower than that ahead of crack tip crack. However, the strain rate is much higher. This is in agreement with previous studies which showed the fracture of this PVA hydrogel is rate dependent, the higher the strain rate is, the smaller the failure strain is. Besides examining the crack propagation, there are other potential applications using DIC on such materials. DIC can provide the full deformation history of the material. In theory, if an effective constitutive model exists, one should be able to obtain the stress history of each individual material point. Once the stress and strain histories are available, it's possible to further study the energy flow during the loading and crack propagation, and thus calculate an effective fracture toughness for such nonlinear materials, as discussed in [74]. In practice, it's very challenging, as it requires a good constitutive model as well as an efficient numerical simulation.

CHAPTER 6

A CRACK TIP STRESS BASED, KINETIC FRACTURE MODEL

6.1 Introduction

To facilitate applications of hydrogels, their fracture behavior needs to be better understood. Assessing the potential for a hydrogel component to fail under load requires a model for the fracture of the hydrogel under a given loading history. Furthermore, understanding of the fracture mechanism of the material can provide insight into approaches to designing hydrogel systems with higher toughness. There have been a lot of studies on the fracture of hydrogels. Baumberger et al. [27] studied the rate dependent fracture energy in alginate and gelation hydrogels. They reported that thermally activated "unzipping" of the noncovalent cross-link zones results in slow crack propagation, prevailing against the toughening effect of viscous solvent drag during chain pull-out. Lefranc et al. [75] fitted the crack opening profile of elastic agar gels with a modified Williams series. The stress intensity factor and

the energy release rate were computed based on the fitting parameters. Goldman et al. [67] studied the dynamic fracture of an elastomer gel. They derived analytical and semi-analytical solutions for the near-tip deformation fields and energy release rates. Mayumi et al. [28] performed experiments on Poly (vinyl alcohol) hydrogels with a single edge notch. The researchers provided a method to separate the energy dissipated during loading from that dissipated during crack propagation. Karobi et al. [29] studied creep rupture of Polyampholyte (PA) hydrogels. They found that the introduction of chemical crosslinks in addition to the physical crosslinks modifies the material's resistance to creep flow. The moderately chemically crosslinked PA gels show better creep resistance compared to lightly chemically crosslinked and uncrosslinked PA gels. Sun et al. [18] studied the fracture of a tough and self-healing PA hydrogel. They proposed that the tearing energy of the PA hydrogel is dominated by the bulk viscoelastic energy dissipation in front of the crack tip. Mishra et al. [30] investigated the fracture of a thermoplastic elastomer gel. They found that these gels fail by a thermally activated process. The energy release rate required to propagate a crack is found to be a function of crack-tip velocity. Recently, the fatigue fracture of different types of hydrogels was systematically studied by Tang et al. [31] Bai et al. [32] [33] and W. Zhang et al. [76] and N. Zhang et al. [77].

Predicting the fracture of novel hydrogels containing transient crosslinks and exhibiting complicated, rate-dependent behavior remains a challenge. Two of the major aspects of understanding fracture in these materials are the crack tip stress and de-

formation fields and the physics of bond failure. Details of the crack tip fields are complicated by the rate-dependent material behavior and large deformation at the crack tip. The complicated constitutive behavior is already a modelling challenge even in homogeneous deformation fields. Complete, analytical solutions of the crack tip fields in hydrogels are not available, thus numerical simulations are required to quantitatively study the crack tip fields. Applying the complex constitutive models in numerical simulations poses further challenges. In addition, a fracture criterion applicable to a broad range of hydrogels under different loading conditions is not yet available. While several researchers have been able to adopt models such as that developed Lake and Thomas [78] to explain the fracture behavior of gels and to obtain a measure of fracture toughness [8] [28] [31] [79] [73], the complexity of the localized stress near the crack tip has not yet been fully addressed. In order to use a crack tip stress based method to predict the failure of a cracked component, a failure criterion that relates the crack tip fields to the onset of fracture is necessary.

In this work, we study the Mode I fracture of a Poly (vinyl alcohol) (PVA) dual-crosslinked hydrogel. In prior work, we have developed a constitutive model that accurately captures the response of this material under different temperatures and loading rates [13] [14] [19]. We have also developed a numerical scheme that allows the application of our constitutive model in a finite element code allowing us to simulate the deformation of a specimen in any geometry, including with an existing crack [16] [17]. With this model, we are able to accurately predict the stress and deformation

fields near the crack tip. Those tools allow us to quantitatively analyze the stress and deformation fields at the tip of a pre-existing crack. However, the constitutive equations model only the deformation and do not address final failure of the gel where the covalent chemical bonds start to fail.

Thus, in this study, we utilize both experimental and numerical tools to study the Mode I fracture of a PVA dual-crosslink hydrogel. The goal of this study is to develop a predictive failure criterion for such materials. The hydrogel specimens are loaded to failure under both constant nominal stress (creep) and constant stretch rate loading conditions. The experiments are simulated using finite element analysis using a constitutive model of the gel developed in our previous work. The stress fields near the crack tip are analyzed, providing us with a means to interpret the experimental results. Based on the interpretation of the experimental results, we propose that a submicrocrack based, thermally activated failure criterion be adopted to predict failure of our hydrogel.

Such models have their origin in the work of Tobolsky and Eyring who modeled creep rupture failure of polymer threads [80]. In their model bond breaking is assumed to be thermally activated with the breaking rate proportional to $\exp(f\lambda/2NkT)$, where f is the stress on a thread, λ is a length scale, N is the number of bonds per area, T is temperature and k is Boltzmann's constant. Coleman expanded on this model to study the strength distribution of fibers under constant stress, monotonically increasing stress and cyclic loading. The model is able to accurately predict the time

to failure under constant stress loading (creep rupture time) and the distribution of strength under constant stress rate tests [81]. Zhurkov and Korsukov proposed a similar approach and elucidated the physics behind these models [82]. Reviews of these kinetic failure models are given by Henderson et al. [83] and Vanel et al. [84]. Similar to the above kinetic bond breaking models, Hui et al. introduced a rate dependent cohesive zone model. In this model the breaking rate for polymer chains ahead of the tip of a growing crack is proportional to $\exp\left(-(E_a - F\lambda)/kT\right)$ where E_a is the activation energy of bond dissociation, F is the force on a polymer chain and λ is a characteristic activation length. With this model they were able to predict the dependence of energy release rate on crack speed [85]. In this paper we will adapt the approach of Hansen [86].

6.2 Experiment

We performed Mode I fracture tests on hydrogel specimens under two types of loading conditions: constant nominal stress (creep) and constant stretch rate. The specimen was 12 mm in width, 2 mm in thickness, and 28 mm in gauge length (the length between two grips). A 4 mm edge crack was cut using a razor blade. The geometry of the test specimen is sketched in Figure 6.1. For the constant nominal stress tests, the specimen with an edge crack was loaded under a constant nominal stress until fracture. Here the nominal stress is defined by the applied force F divided by the uncracked cross-sectional area, A_0 (12 mm $\times$ 2 mm). Five different nominal stress

levels were applied: 2.8 kPa, 3.4 kPa, 4 kPa, 4.75 kPa and 5.5 kPa. The PID control system ramped the load up to the target value in 10 seconds and then held the load constant within ±0.2% for the duration of the test. For each load level, the tests were repeated three or four times.

For the constant stretch rate tests, specimens with the same geometry were loaded to failure under different constant stretch rates $\dot{\lambda}$. Here the stretch rate $\dot{\lambda}$ is defined as the change of length per unit time, $\dot{l}$, divided by the original gauge length l_0, i.e., $\dot{\lambda} = \dot{l}/l_0$. The specimens were loaded to failure under four different stretch rates, 0.0003/s, 0.001/s, 0.003/s and 0.01/s. For each stretch rate, the tests were repeated three or four times.

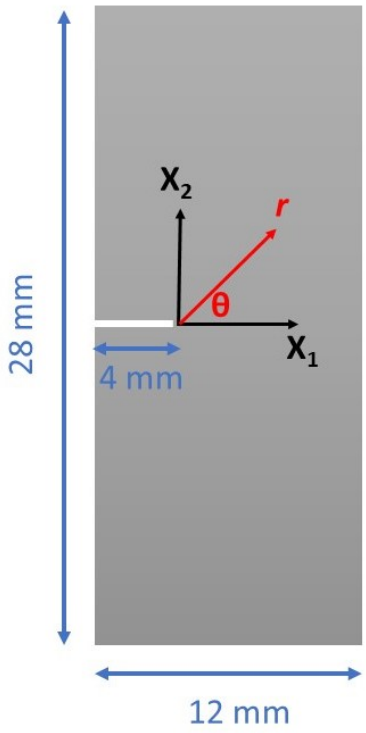

Figure 6.1: Sketch of the geometry of a test specimen. 2 mm thick

6.3 Finite Element Calculation of Crack Tip Fields

To apply the kinetic failure model the state of stress at the crack tip must be known. Finite element analysis (FEA) is used to find the amplitude of the singular crack tip stress fields. The simulation was performed by Guo. The constitutive model used in the FEA is based on a model for the dynamic formation and breaking of the transient bonds in the gel [13] [16]. The total strain energy of the PVA gel is the sum of the strain energies carried by the chains connected by chemical and physical crosslinks. The chemical crosslinks do not break; the physical crosslinks can break and

heal independently of the loading condition, and this breaking and healing kinetics reaches dynamic equilibrium. A physical crosslink reforms at zero stress and loses all its strain energy immediately after it breaks. So, its strain energy is characterized by its deformation from the time of reformation to the current time. This constitutive model is completely determined by four independent material parameters, which are fit using data from a relaxation test. The material parameters used in the simulation are

$$\mu\rho = 2.3710 \text{ kPa}, \mu\bar{\gamma}_\infty = 6.2267 \text{ kPa/s}, \alpha_B = 1.6076, t_B = 1.3339 \text{ s}$$

We implemented this constitutive model as a user material (UMAT) in ABAQUS with the fitted material parameters. Testing the prediction of the 3D and plane-stress UMATs against experiments, we find that the calculated displacement and stress fields agree well with our asymptotic analysis, and that the crack opening profiles and strain fields compare well with experimental data [16] [17].

Using symmetry, half of the specimen shown in Figure 6.1 was modelled. As discussed in [16], plane stress assumptions work well with thin sheet samples, thus we use the plane stress UMAT in all simulations. Mesh convergence is checked by comparing calculations using a neo-Hookean material model against the asymptotic fields of a neo-Hookean solid. All simulations are carried out using quadratic plane stress elements in static steps. In order to properly capture the stress dominance near the crack tip, the mesh is refined near crack tip, with the smallest element size of 0.0002 mm.

From the FEM results, the logarithmic strain tensor $\boldsymbol{\varepsilon}^L$ and Cauchy stress $\boldsymbol{\tau}$ in front of the crack were extracted. The nominal (PK-I) stresses $\boldsymbol{\sigma}$ were calculated by

$$\boldsymbol{\sigma} = \boldsymbol{\tau}\boldsymbol{F}^{-\boldsymbol{T}} \tag{6.1}$$

where

$$\boldsymbol{F} = \boldsymbol{V}\boldsymbol{R} = \boldsymbol{V} = \exp\left(\boldsymbol{\varepsilon}^{\boldsymbol{L}}\right) \tag{6.2}$$

where $\boldsymbol{F}$ is the deformation gradient, $\boldsymbol{V}$ and $\boldsymbol{R}$ are the left stretch tensor and rotation tensor, respectively. Because X_1 and X_2 are the principal directions along the crack face, $\boldsymbol{R} = \boldsymbol{I}$, the identity tensor (this is only true along the crack plane). The far field stress, p, is calculated by the total force acting on the top surface, P, acting in X_2 direction, divided by the width of the specimen. The total force P is obtained by constraining all nodes on the top surface to one reference point and extracting the reaction force on that reference point. In constant nominal stress simulations, a constant load, P , is applied as boundary condition. In the constant stretch rate simulations, the displacement on the top surface, which is linearly increasing with time, is prescribed as the boundary condition.

6.4 Results

6.4.1 Experimental Results

The stress vs. stretch curves for edge cracked samples under constant stretch rates are shown in Figure 6.2 (a). The PVA dual-crosslink hydrogel clearly shows rate-dependent behavior. The material is stiffer as the loading rate increases. This rate dependence results from the breaking and reforming of the physical crosslinks. The hydrogel specimens fractured at different nominal stresses and stretch ratios depending on the stretch rates. The higher the stretch rate, the smaller the stretch ratio at which the specimen fractured. We observe that once crack growth initiates from the tip of the existing crack, it propagates rapidly ($\approx$ 100 mm/s), causing complete failure in less than 0.1 s.

The results for the constant stress tests are shown in Figure 6.2 (b). As creep occurs the stretch increases with time. This behavior is because the physical crosslinks break and reform during loading. When a physical crosslink breaks, the polymer chain that attaches to it is relaxed and it does not carry any stress. Due to this relaxation mechanism, the specimen stretches even while the nominal stress is held constant.

For all the nominal stress levels tested in this study, the specimen eventually fractured. The failure time vs. applied nominal stress is plotted in Figure 6.3. The variations in measured time to failure at each load level are likely due to variations in the crack tip shape of the pre-cut crack. Such dispersion is also observed in the creep

fracture tests of other polymers [86] and indeed arises in many fracture experiments. It can be seen that the log of time to failure t_f is approximately linear with the applied nominal stress. This indicates that the failure time and the nominal stress follow an exponential relation. Similar behavior was also observed by Karobi et al. in the fracture of Polyampholyte (PA) hydrogels under tensile loading [29] and by Skrzeszewska when loading a TR_4T gel under shear [87]. This exponential relation between fracture time and applied stress suggests that the experimental results can be explained by a thermally activated fracture model.

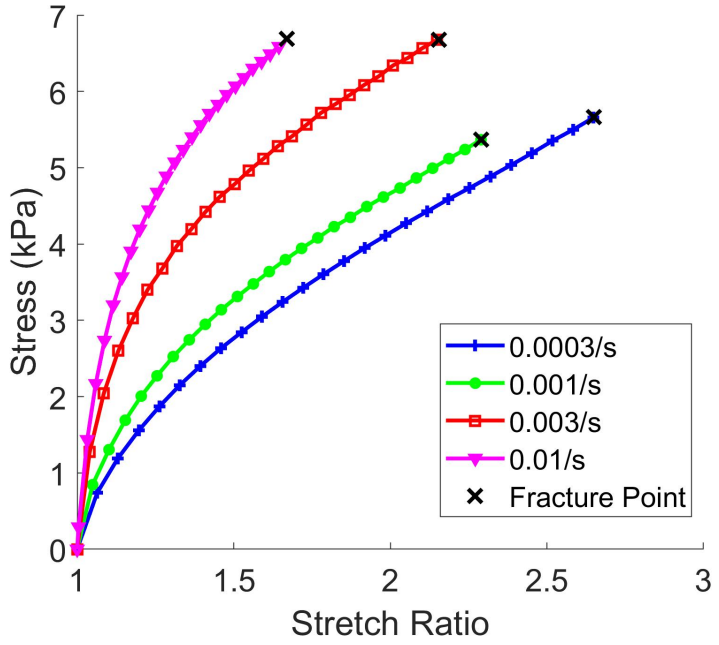

(a)

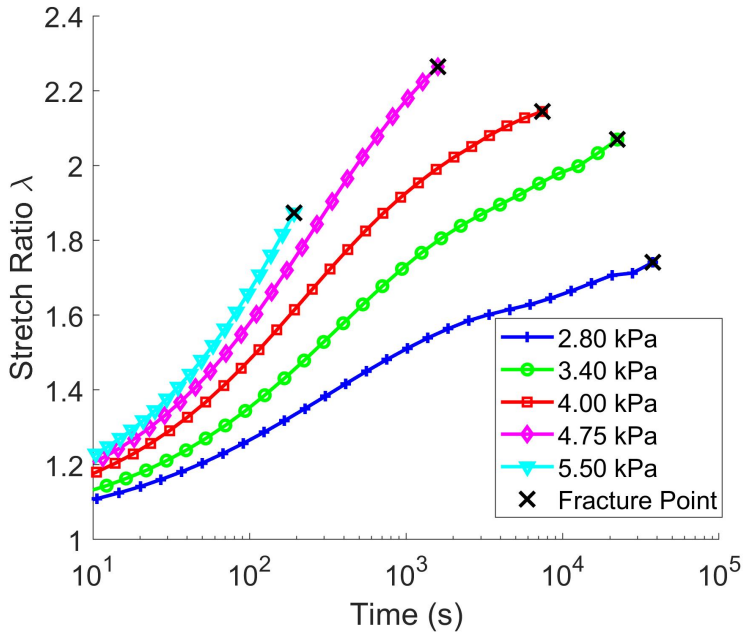

(b)

Figure 6.2: Experimental results for edge cracked PVA hydrogel specimens: (a) Stress vs. stretch under constant stretch rates. (b) Stretch vs. time under constant applied nominal stress. Each curve represents the average of 3 or 4 tests. All the repeats are included in Appendix A.1

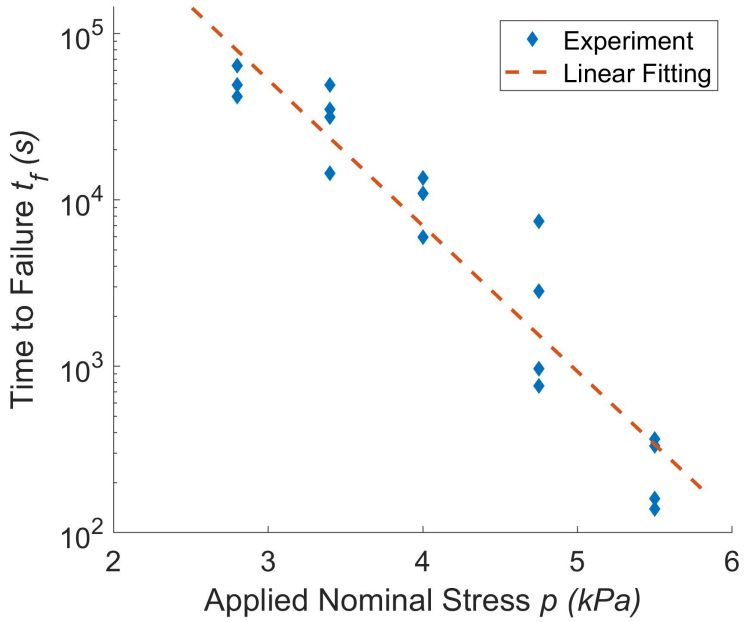

Figure 6.3: The time to failure for different stress levels in the constant stress (creep) tests

6.4.2 Finite Element Results

As a first check of the accuracy of the FEM simulations, we compare the predicted and measured stretch vs. time in the creep fracture experiments and stress vs. stretch in the constant stretch rate fracture experiments. The comparison between FEM and experiments for two stretch rates of the constant stretch rate tests and two stress levels for constant stress tests are shown in Figure 6.4 and 6.5. It can be seen that there is a good agreement between the FEM prediction and experimental results. The agreement is equally good for other tests, which are not shown here.

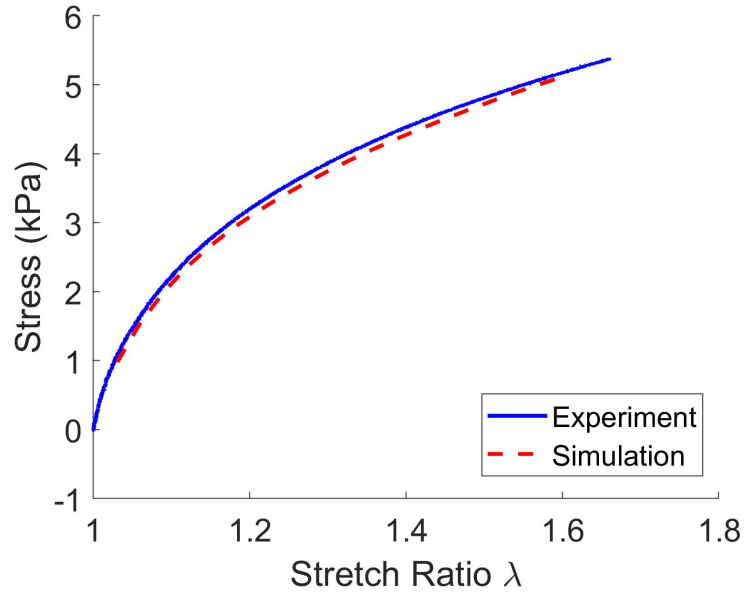

(a)

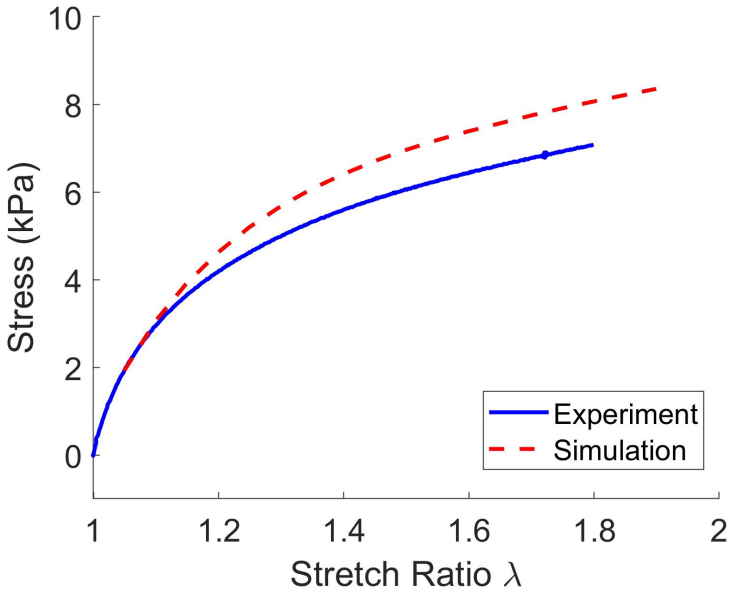

(b)

Figure 6.4: Comparison between the FEM simulation vs. the experimental results of stress vs. stretch for the constant rate tests (a) 0.003/s (b) 0.01/s

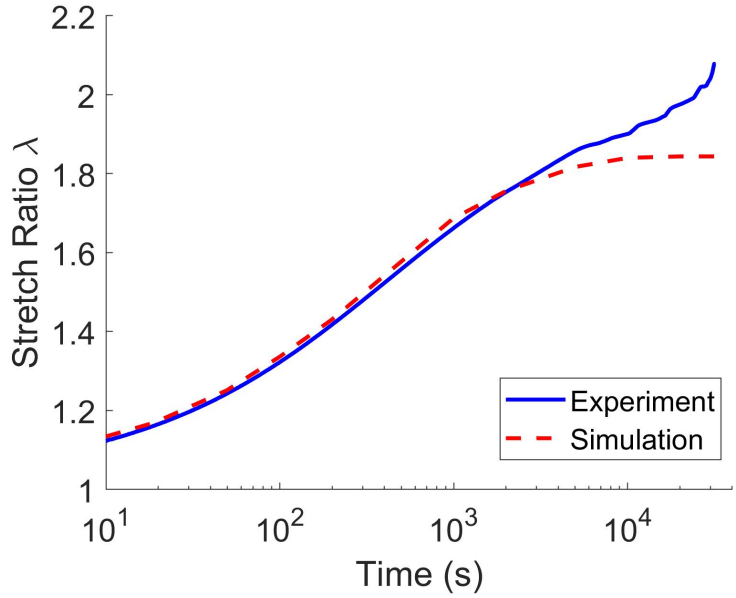

(a)

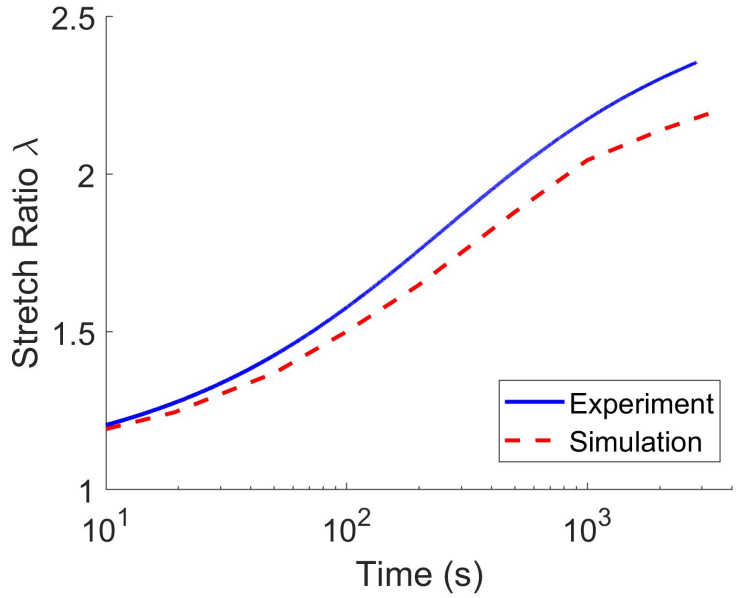

(b)

Figure 6.5: Comparison between the FEM simulation vs. the experimental results of stretch vs. time for the constant stress tests (a) 3.40 kPa (b) 4.75 kPa

After the simulation has been validated against the overall experimental results, we

investigated the stress fields near the crack tip. For our constitutive model, all the chains are assumed to be Gaussian, and a Neo-Hookean model is used for the strain energy. Based on the asymptotic results from [88], the nominal stress (PK-I stress) in the primary loading direction near the crack tip should inversely scale with the square root of the distance to the crack tip, that is

$$\sigma_{22} = \bar{B} r^{-1/2} \tag{6.3}$$

where r is the distance from the crack tip in the undeformed reference configuration and $\bar{B}$ is a scaling factor (denoted as the stress amplitude in the following text). Here we are interested in the nominal (PK-I) stress for the following reason. When the material is under load, consider a reference area A_0 inside the material subject to a total force of F. Assume that there are N_0 polymer chains penetrating this area, sharing the force F. We assume incompressibility. Under the applied force, the area A_0 becomes A in the current configuration. For large stretches this current area A might be quite different than A_0. However, the number of chains penetrating this area should, on average, remain the same. Because this PVA hydrogel contains mostly water, the fraction of polymer chains is relatively low and there's relatively a large amount of free space between the polymer chains, the change of area primarily comes from the change of the free space around the polymer chains. So, the force F is still shared by the same number of bonds N_0, as in the reference area A_0. In this sense, the change of area is not expected to significantly alter the average load

carried by each polymer chain. Thus, the nominal (PK-I) stress, which refers back to the reference area, is used in our failure model.

From the simulations of the tests, we extracted the stress values on a line extending from the crack tip on ($\theta = 0$, $r > 0$) and fit the results to a $r^{-1/2}$ distribution. As Figure 6.6 shows, for all of the stress levels used in the creep tests, the FEM results can be accurately fit to the $r^{-1/2}$ distribution in the region very close to the crack tip where the asymptotic field should dominate.

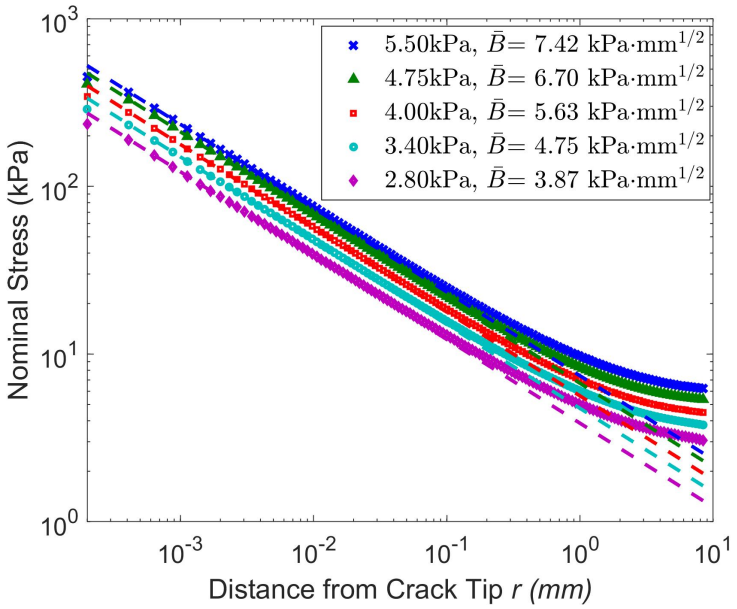

Figure 6.6: The nominal stresses for creep tests from finite element simulation and corresponding $r^{-1/2}$ fitting

The stress amplitudes $\bar{B}$ in the figure were obtained directly from the fitting. Here the stress amplitude $\bar{B}$ is similar to the stress intensity factor K_I in Linear Elastic Fracture Mechanics (LEFM). In LEFM, for a given specimen, K_I scales linearly with the far-field applied stress p. In other words, the ratio K_I/p should be a constant

for a given specimen in LEFM. In the hydrogel, since the material is non-linear, and the specimen undergoes large deformation, we don't expect that $\bar{B}$ will scale linearly with the far-field applied nominal stress p. To study how the scaling changes with deformation, the ratio $\bar{B}/p$ was calculated at different stretch levels and is plotted in Figure 6.7 for the different loads. From Figure 6.7, it can be seen that the ratio $\bar{B}/p$ is not constant. For a stretch level greater than 1.3, $\bar{B}/p$ increases approximately linearly with the stretch ratio. Note that $\bar{B}/p$ results for stretch ratios smaller than 1.3 are not shown. This is because, at small deformations, the region of dominance of the asymptotic stress field solution is too small for the FE simulation to capture without using computationally costly extremely fine meshing. All of the failures observed in the experiments occurred at stretch ratio of 1.5 or higher.

From Figure 6.7, it can also be seen that the slopes of those lines are approximately the same, which means for all the cases shown here, the rates at which $\bar{B}/p$ increases with stretch ratio λ are approximately the same. For each individual test in Figure 6.7, we fit the data with a linear fit, and obtain an average slope of $0.28 \pm 0.05\ \sqrt{mm}$ per stretch.

For the creep tests, it is also informative to look at the variation of $\bar{B}/p$ with respect to time, as shown in Figure 6.8. From Figure 6.8, it can be seen that except for the load level of 5.5 kPa in which the specimen fractured at about 300 seconds, $\bar{B}/p$ varies little for most of the test duration. For those tests, the time to failure ranges from about 4,000 seconds to about 50,000 seconds, but the factors $\bar{B}/p$ after 1,000

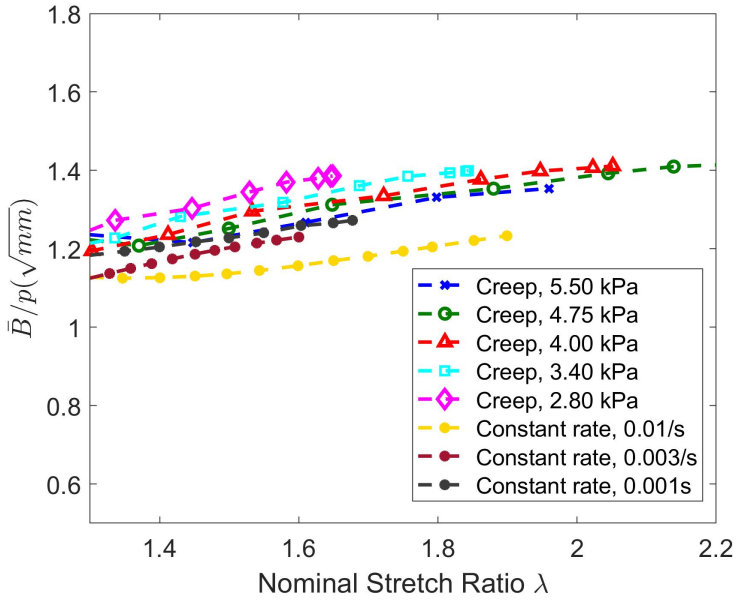

Figure 6.7: The variation of $\bar{B}/p$ with respect to stretch ratio for the constant stress tests and constant rate tests

seconds are nearly constant. Thus, we can conclude that for those tests the $\bar{B}/p$ ratio can be approximated as constant for the duration of the experiment.

6.5 Analysis of Creep and Constant Stretch Rate Experiments

In uniaxial creep test of polymer specimens, one often observed a linear relation between the log of time to failure versus the applied nominal stress. This suggests a thermally activated fracture process [29] [87] [30].

The fracture of the PVA hydrogel is due to the breaking of the covalent bonds. For a specimen with an edge crack, stress is highly localized near the crack tip and thus

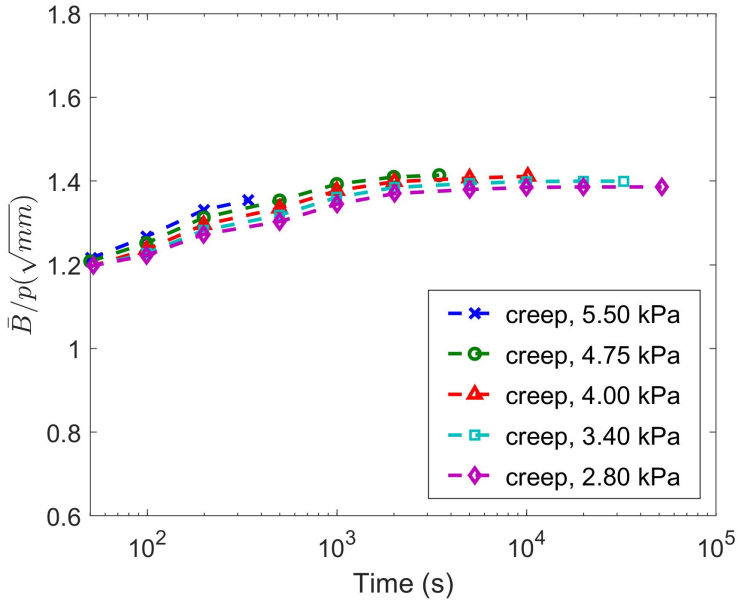

Figure 6.8: The variation of $\bar{B}/p$ with respect to time for the constant stress tests

the bonds very close to the crack tip will break most rapidly and will nucleate an unstable crack. The breaking of chemical bonds forms a small damage zone near the crack tip. Once there are enough broken bonds in this zone, the material will become unstable and fail instantaneously. This is akin to what Zhurkov and Korsukov argued [82], writing that *"The mechanism of fracture of polymers may be divided into three stages: (1) excitation of bonds under the action of mechanical stress, (2) scission of the excited overstressed bonds by thermal fluctuations, and (3) formation of submicrocracks and their coalescence into larger cracks."*

Under constant stress loading, the time to failure for thermally activated fracture is governed by the classic durability equation [82]:

$$t_f = \tau_0 \exp\left(\frac{U - \gamma\sigma}{kT}\right) \tag{6.4}$$

where t_f is the time to failure, $\tau_0 \approx 10^{-13}$ s is the characteristic oscillation time of atoms in a solid, U is the activation energy of fracture, γ is a material parameter, characterizing the activation volume of bond rupture, σ is the applied stress, k is the Boltzmann constant ($1.38 \times 10^{-23} J \cdot K^{-1}$), and T is the absolute temperature. Based on this classic theory, Hansen and Baker proposed a rate dependent kinetic theory of fracture for polymers [86] which was able to predict the relation between time to failure and applied stress for PMMA under both constant stress loading and constant stress rate loading. They hypothesized that the total submicrocrack accumulation at failure for a given material is, to a good approximation, independent of the mechanical loading condition (stress rate, stress history etc.), which was also experimentally validated in [82]. They proposed a crack damage state variable $n(t)$ which characterizes the level of damage (bond breaking). Evolution of the damage state variable, $n(t)$, can be written in the form of a differential equation:

$$\frac{dn}{dt} = -K_b n + n_0 K_b, n(0) = 0 \tag{6.5}$$

Here $n(t) = 0$ corresponds to no damage (initial state). $n(t) = 1$ indicates that damage has reached a critical level, resulting in failure of the material under load. The value, $n_0 = 1.58$ is derived by matching the above model to the durability equation (6.4). K_b is the material breaking rate written as:

$$K_b = \frac{1}{\tau_0} \exp\left(-\frac{U - \gamma\sigma}{kT}\right) \tag{6.6}$$

The differential equation (6.5) developed by Hansen and Baker expands the applicability of the classic durability equation (6.4) to cases which have more complex loading history, that is, σ in (6.6) need not be constant.

For constant nominal stress tests, the solution to (6.5) has closed form:

$$n(t) = n_0(1 - \exp(-K_b t)) \tag{6.7}$$

Assuming that at t_f, the time of failure, $n(t = t_f) = 1$, then (6.7) can be written as:

$$\ln t_f = -\frac{\gamma}{kT}\sigma + \frac{U}{kT} + \ln \tau_0 \tag{6.8}$$

Equation (6.8) can also be directly obtained from (6.4), and can be applied to predict creep failure of uncracked polymer specimens under uniform, constant applied stress. However, in our fracture tests, the test specimen has an edge crack in it and thus the stress is not uniform, but highly concentrated near the crack tip. To take this into account, we use the crack tip stress. From asymptotic analysis and the finite element simulation, we know that in the region very close to the crack tip, the nominal stress, σ_{22}, in the primary loading direction is singular and can be written as $\sigma_{22} = \bar{B}/\sqrt{r}$, where $\bar{B}$ is the stress amplitude factor similar to the stress intensity factor in linear elastic fracture mechanics. Note that in a region very close to the crack tip, where active bond failure is taking place the stress may deviate from the $1/\sqrt{r}$ singularity if the material response deviates from the neo-Hookean assumption.

In place of σ in equation (6.8) we use the crack tip stress value calculated at a distance r_c from the crack tip. Equivalently one can think of this as the stress averaged over a distance r_c from the crack tip. Denoting this stress value as σ_c we have

$$\sigma_c = \frac{\bar{B}}{\sqrt{r_c}} \tag{6.9}$$

The distance r_c can be thought of as representing the molecular size scale of bond rupture [89], [90]. With σ in equation (6.8) replaced by σ_c from equation (6.9), for the creep rupture tests the failure time is

$$\ln t_f = -\frac{\gamma}{kT}\frac{\bar{B}}{\sqrt{r_c}} + \frac{U}{kT} + \ln \tau_0 \tag{6.10}$$

In previous section, we have shown that for the creep tests, the ratio $\bar{B}/p$ for the creep tests did not vary significantly during the tests and this ratio is almost independent of the applied stress (see Figure 6.8). Thus, we approximate $\bar{B}/p$ as a constant,

$$\bar{B}/p = C_B \tag{6.11}$$

Here C_B is the scale coefficient which we assume to be constant for all the constant stress (creep) tests. From the previous results in Figure 6.8, $C_B \approx 1.4\sqrt{mm}$ for all creep tests. Substitute (6.11) into (6.10) and rearrange the equation to obtain the relation between the time to failure t_f and the applied nominal stress p for a specimen containing a pre-crack:

Parameter	Lower bound of 95% confidence interval	Upper bound
U (J)	1.85×10^{-19}	1.97×10^{-19}
$\gamma/\sqrt{r_c}$ ($m^{5/2}$)	1.54×10^{-22}	2.17×10^{-22}

Table 6.1: Summary of material parameters from fitting of constant stress tests

$$\ln t_f = -\frac{\gamma}{kT}\frac{C_B}{\sqrt{r_c}}p + \frac{U}{kT} + \ln \tau_0 \tag{6.12}$$

From (6.12) it can be seen that with C_B constant, the log of time to failure will still be linearly proportional to the applied far-field nominal stress, even when a pre-crack exists. This is consistent with what is observed in the experimental results from creep tests, Figure 6.3.

We performed a linear fitting of $\ln t_f$ and the applied nominal stress p. With the slope and intercept from the fitting, the activation energy U and the material parameter $\gamma/\sqrt{r_c}$ can be obtained. Since there is scatter in the measured failure time t_f for each applied stress level, we take the values that lie in the 95% confidence interval. The corresponding values are listed in Table 6.1.

The above shows that by combining the nominal stress field near the crack tip with a submicrocrack based, thermally activated failure criterion, we are able to relate the time to failure of the hydrogel specimens under creep tests to the applied nominal stress. To test the applicability of this failure criterion to other situations, we use the model parameters obtained from the creep tests to predict the failure of hydrogel specimens under *constant stretch rate* tests. For the constant stretch rate tests, a closed form solution of (6.5) is not available thus the model is integrated numerically.

Equations (6.5) and (6.6) can be written in a discrete form, with the crack tip stress taken into account:

$$\frac{n(t_{i+1}) - n(t_i)}{\Delta t} = -K_{bi} n(t_i) + n_0 K_{bi} \tag{6.13}$$

$$K_{bi} = \frac{1}{\tau_0} \exp\left(-\frac{U - \frac{\gamma C_B}{\sqrt{r_c}} p_i}{kT}\right) \tag{6.14}$$

Here the subscript i denotes the i_{th} time step. The nominal stress history p_i for the constant stretch rate tests are available from our experimental data. C_B and $\gamma/\sqrt{r_c}$ are introduced to take into account the existence of a sharp crack, as discussed before. The material parameters U and $\gamma/\sqrt{r_c}$ were obtained from the constant nominal stress tests and are applied directly to the constant stretch rate tests. For the constant stretch rate loading, from Figure 6.4, C_B scales approximately linearly with the stretch ratio λ. Thus, from the results of Figure 6.4, for each constant stretch rate test, we performed a linear fit between C_B and λ. In this way C_B at a given stretch ratio can be estimated. We did not perform a finite element simulation for the stretch rate 0.0003/s, but from the trend in Figure 6.4, it is reasonable approximation that C_B vs. λ for 0.0003/s is close to that of the rate 0.001/s.

All the quantities in (6.13) and (6.14) are known from the creep tests and FEM calculations, thus we can integrate those equations to calculate the evolution of $n(t)$. The predicted failure time for the constant stretch rate tests is the time calculated

corresponding to $n(t) = 1$. The predictions of the failure theory are compared with the experimental results in Figure 6.9. It can be seen that this failure criterion gives a good prediction of fracture under constant stretch rate loading. The agreement between the model prediction and experiments is very good for the loading rates of 0.0003/s, 0.001/s and 0.003/s. The prediction is less good for 0.01/s. One reason is that, for the creep tests, the average stretch rates are on the order of 0.0001/s to 0.001/s, which is much slower than the fastest loading rate for the constant stretch rate test, 0.01/s. At a relatively faster stretch rate, say 0.01/s, a relatively large portion of the physical crosslinks are still connected and may affect the accumulation of submicrocracks. This may indicate that the failure criterion has some limitations when predicting the failure of specimens at high loading rates.

Previously, we have obtained the parameters U and $\gamma/\sqrt{r_c}$. U is the activation energy of bond failure, and is a material dependent quantity. Converting units, the activation energy for the PVA gel is 111 to 118 kJ/mole, close to the values of 117 to 125 kJ/mole reported by Hansen and Baker [86] for PMMA and 113 to 125 kJ/mole for HDPE, LDPE and PP [90].

The parameter $\gamma/\sqrt{r_c}$ requires some explanation. Here γ is the activation volume of fracture and r_c is a distance used to compute the crack tip stresses. We have no means to directly measure γ or r_c. However, one way to interpret this is to relate the activation volume to the distance r_c, i.e. $\gamma \sim {r_c}^3$. In that case $\gamma/\sqrt{r_c}$ is reduced to ${r_c}^{2.5}$. Then based on the previous fitting, we deduce a characteristic activation length

$\gamma^{1/3}$ of 2.1 nm. Reported values of $\gamma^{1/3}$ for dense polymers range from about 0.1 to 17 nm [86] [89] [90]. The activation volume can be thought of as representing the molecular size scale of bond breaking. Dijkstra [89] states it in words as: *"activation volume ≈ chain cross-section × bond length perpendicular to the cross-section × elongation at break."*

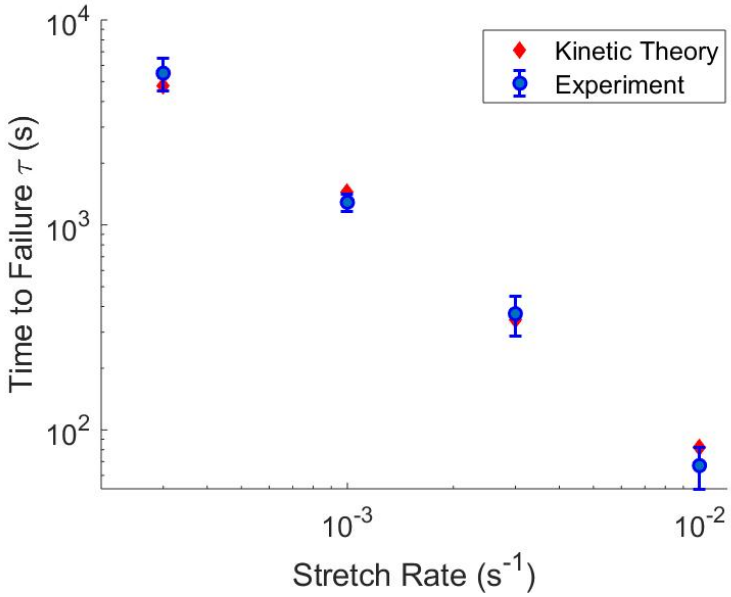

Figure 6.9: Comparison between the failure time predicted by the submicrocrack based theory and experimental results at constant stretch rates. For the model predictions, the error bars are based on the 95% confidence interval of the material fitting parameters

6.6 Conclusion

In this study, we utilized experiments and finite element simulations to study the Mode I fracture of a PVA dual-crosslink hydrogel under creep and constant stretch rate loadings. The goal of this study is to propose a practical failure criterion for

such materials. From the experimental results, it is shown that for the creep tests, the time to failure and applied stress follow an exponential relationship. For the constant stretch rate tests, the specimens failed at different stresses and stretches for different loading rates. Using a constitutive model and a numerical scheme we developed in our previous work, we obtained the stress fields near the crack tip with finite element simulation. By utilizing a concept of stress at a characteristic distance, we established the connection between the nominal stress amplitude, $\bar{B}$, near the crack tip and the far field applied stress. Combining the nominal stress amplitude and a kinetic bond breaking model, we fit the exponential relation between time to failure and the applied stress levels observed in creep tests. With material parameters obtained from fitting of the creep tests, we are able to accurately predict fracture during constant stretch rate tests using the same failure criterion. Future research could include further testing of the validity of this criterion by applying it under cyclic loading, at varying temperatures and to different hydrogels.

Appendix A

APPENDIX

A.1 Experimental Results for Chapter 6

All the repeats for the constant stress tests and constant stretch rate tests are shown in Figure A.1 and Figure A.2 respectively.

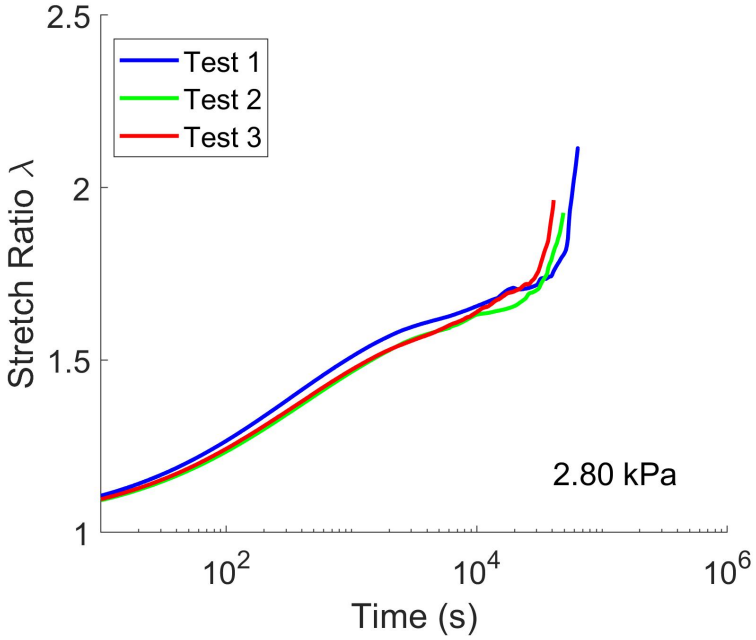
Test 1
Test 2
Test 3
2.80 kPa
Stretch Ratio λ
Time (s)
2.5
2
1.5
1
10^2
10^4
10^6

(a)

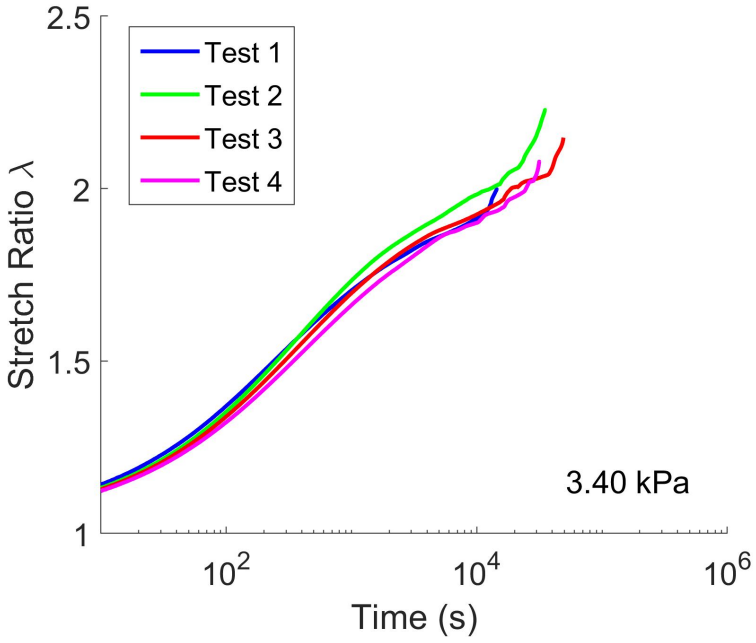
Test 1
Test 2
Test 3
Test 4
3.40 kPa
Stretch Ratio λ
Time (s)
2.5
2
1.5
1
10^2
10^4
10^6

(b)

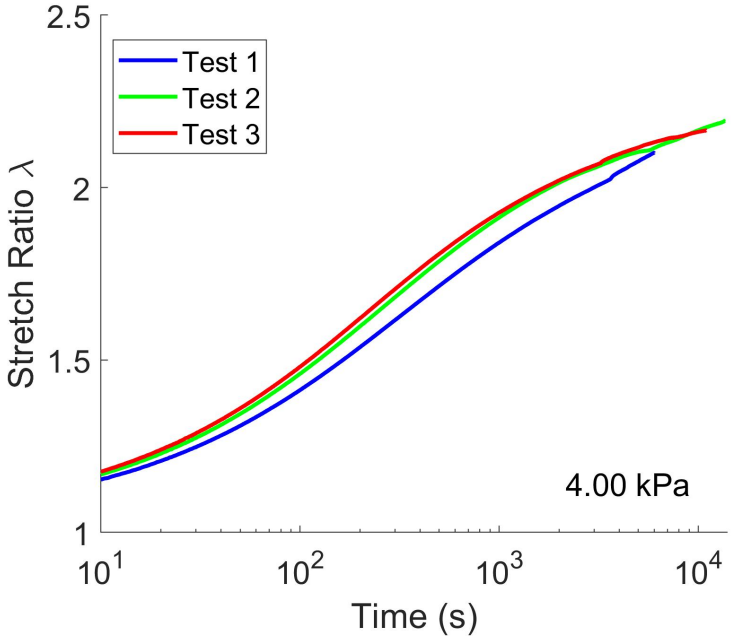
Test 1
Test 2
Test 3
Stretch Ratio λ
Time (s)
4.00 kPa
2.5
2
1.5
1
10^1
10^2
10^3
10^4

(c)

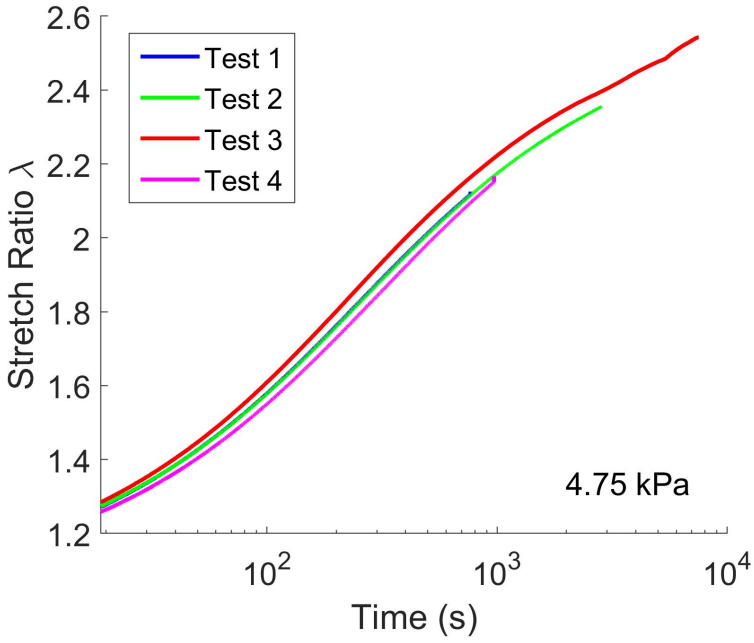
Test 1
Test 2
Test 3
Test 4
Stretch Ratio λ
Time (s)
4.75 kPa
2.6
2.4
2.2
2
1.8
1.6
1.4
1.2
10^2
10^3
10^4

(d)

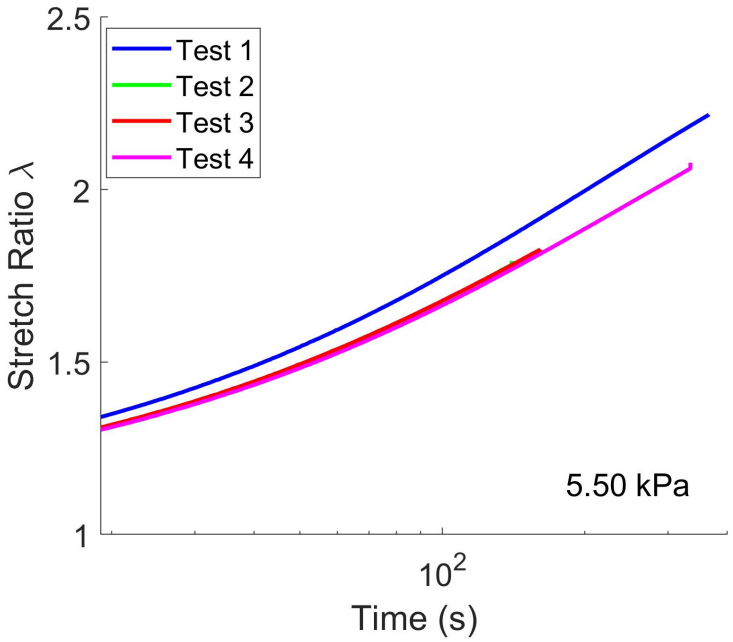

(e)

Figure A.1: Experimental results of constant stress tests: (a) 2.80 kPa (b) 3.40 kPa (c) 4.00 kPa (d) 4.75 kPa (e) 5.50 kPa

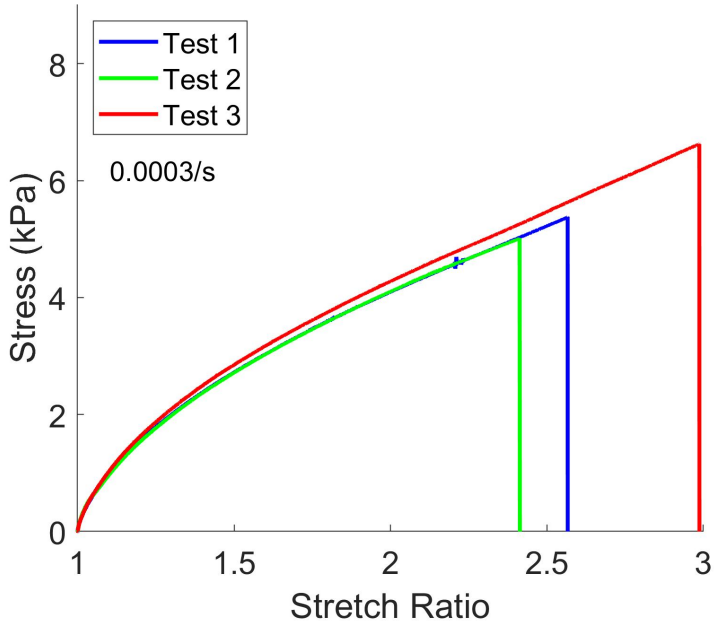

(a)

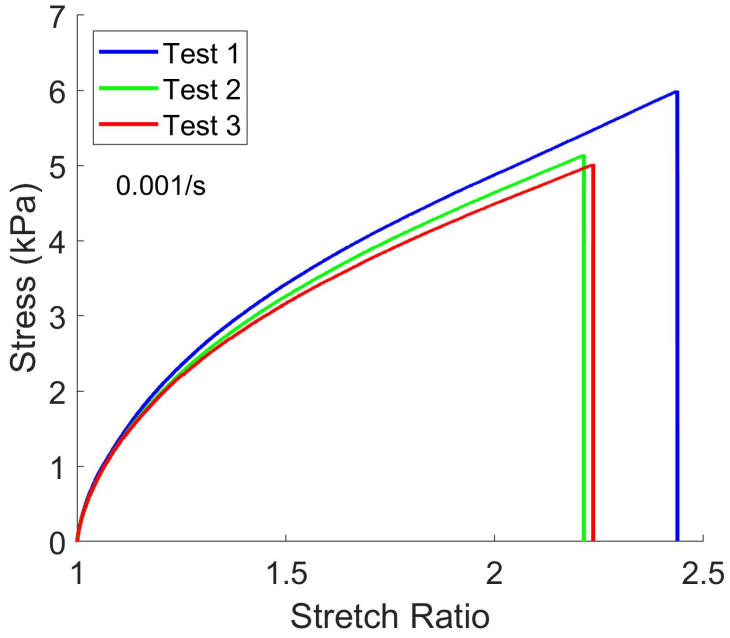
Test 1
Test 2
Test 3
0.001/s
Stress (kPa)
Stretch Ratio
0
1
2
3
4
5
6
7
1
1.5
2
2.5

(b)

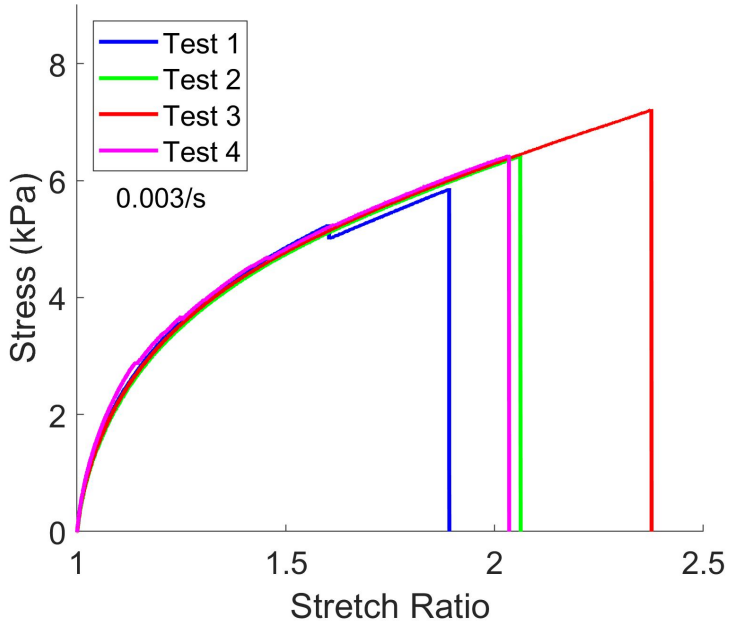
Test 1
Test 2
Test 3
Test 4
0.003/s
Stress (kPa)
Stretch Ratio
0
2
4
6
8
1
1.5
2
2.5

(c)

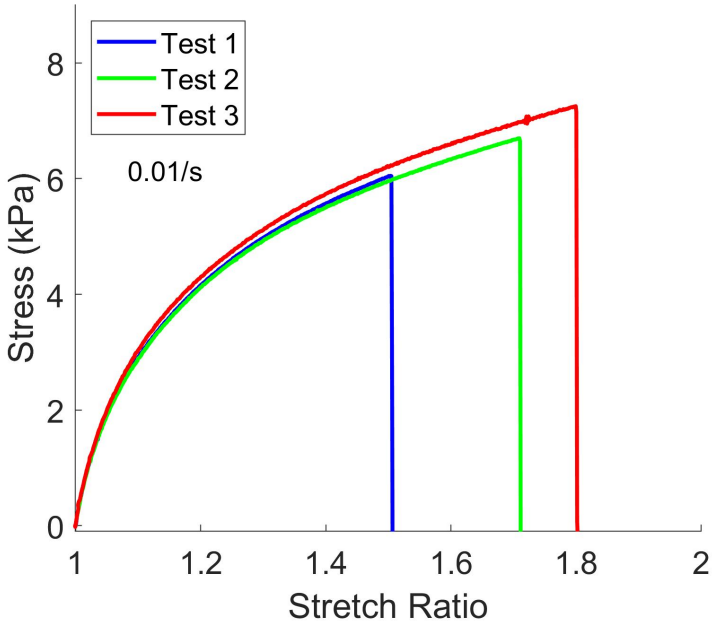

(d)

Figure A.2: Experimental results of constant stretch rate tests: (a) 0.0003/s (b) 0.001/s (c) 0.003/s (d) 0.01/s

A.2 Comments on the Crack Propagation Speed

In Chapter 5, we immersed the hydrogel specimen in oil for the crack propagation test. We noticed that if the specimen was tested in the air, the crack propagation speed was much higher compared to that tested in the oil. It is still not clear what causes this difference. One hypothesis is that when tested in the air, the drying near the crack tip affects the stretch at fracture. When the crack is propagating at much different stretch levels, the energy stored in the system can be quite different. This leads to different crack growth behaviors.

Even when we tested the specimen in the oil, the crack speed data show significant scatter. In our preliminary experiments, we loaded specimens (18 mm width, 28 mm gauge length, 2mm thickness and 4 mm edge crack. These specimens are much narrower compared to those in Chapter 5) to fracture at different stretch rates of 0.003/s, 0.03/s, and 0.3/s, with 3 or 4 repeats at each loading rate. The corresponding crack propagation speeds are 110 $\pm$ 40 mm/s, 109 $\pm$ 6 mm/s and 126 $\pm$ 55 mm/s, as shown in Figure A.3. It can be seen that the stand deviations for 0.003/s and 0.3/s are quite large. We were not able to get a very consistent crack speed even we used specimens with nominally same geometry under same loading rates. We think the scatter could be due to the details near the pre-cut crack, as we could not make exactly identical cracks. The stress near the crack tip could be very sensitive to the details at micro-scale. For most of our crack propagation tests, the crack growth

speed is in the range of 40 to 200 mm/s.

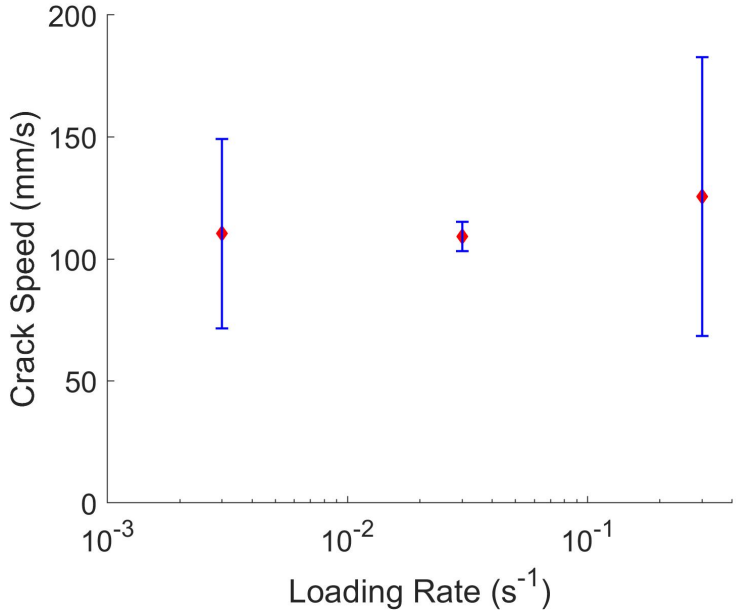

Figure A.3: Crack propagation speed at different loading rates. Here the speed is mapped to the undeformed configuration

In [28], the researchers reported that when they loaded this PVA hydrogel under slow loading rates, the crack grew at very slow speed. The corresponding crack growth speed for loading rates of 0.0003/s and 0.001/s are approximately 0.07 mm/s and 12 mm/s respectively. We never observed such slow crack growth in our tests, even at the loading rates of 0.0003/s and 0.001/s. One thing needs to be pointed out is that, in [28], instead of directly observing the crack growth, the researchers estimated the crack speed by using the drop in the load cell signal. The time period during the load drop was considered as the crack growth period. Then the crack speed was estimated by diving the specimen length by this estimated time. We compared the time estimated by this method with that directly observed using a high speed

camera for three tests, as shown in Table A.1. It can be clearly seen that there's some inconsistency between those two methods.

Test #	Time estimated from load drop (s)	from direct observation (s)
1	0.0458	0.1175
2	0.1583	0.1978
3	0.0458	0.1080

Table A.1: Comparison between the crack propagation time estimated using load signal drop and direct observation using a camera

A.3 Cracked Specimen under Cyclic Loading

We also tried to study whether this PVA hydrogel shows fatigue crack growth behavior. Specimens with an edge crack were cyclically loaded to a large number of cycles to see whether the crack shows incremental growth.

There are two types of loading conditions. The first is displacement control. Here we loaded the specimen to a certain stretch ratio under a certain loading rate then unloaded. We also allowed different resting periods between cycles. We tried different loading rates, stretch ratios and resting periods. However, we did not observe any fatigue crack growth in our material, even when the specimen was loaded to a maximum of 10^4 cycles. There were one or two experiments where the specimen did fracture after a large number of cycles of loading. However, this fracture can not be consistently duplicated. In addition, even when the specimen was immersed in oil

for a relatively long time period, slow drying could also happen. The property of the gel might also change. Thus it is difficult to say whether the fracture was due to the cyclic loading or the weakening of the material. Besides the displacement control, we also applied cyclic loading using a stress control. The specimen was loaded to a certain applied stress level and then unloaded to zero stress. Because this material can relax, in order to reach the same stress level, the stretch increased slightly after each cycle. A typical result from the stress - control cyclic loading is shown in Figure A.4. At some relatively high stress levels, We did see the material fracture under this type of loading, but it does not correspond to the fatigue crack growth behavior. It should be pointed out that for the above mentioned experiments, we used a narrower specimen (12 mm width, 4 mm edge crack) compared to the specimen in Chapter 5.

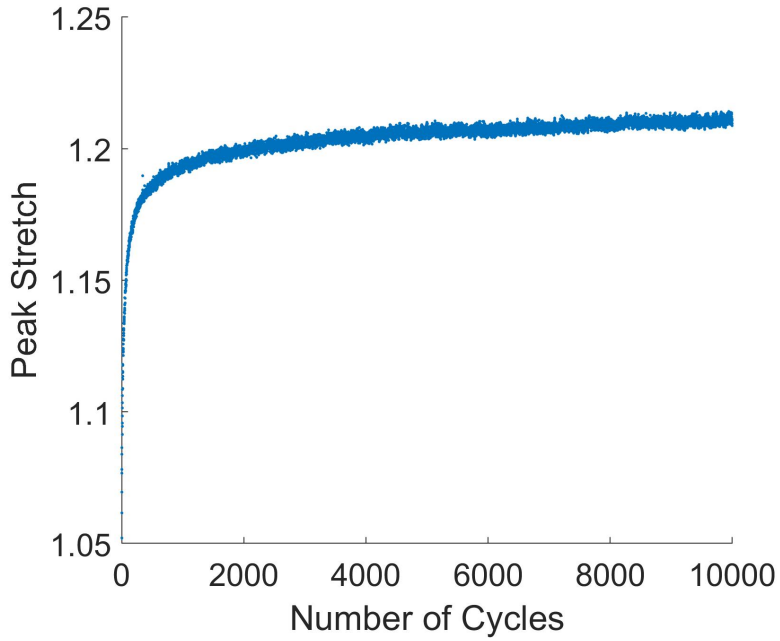

Figure A.4: A typical result from the stress - control cyclic tests. Here the peak stretch in each cycle is plotted against the number of cycles. The applied stress was 3000 Pa and the stretch rate was 0.03/s, with no resting period between cycles.

A.4 Hydrogel Cutting Tests

We also performed cutting tests on the hydrogel specimen. The experimental setup is shown in Figure A.5. The specimens of 12.5 mm thickness were cut by single edge razor blade at six different speeds: 0.1 mm/s, 0.3 mm/s, 1 mm/s, 2 mm/s, 5 mm/s and 10 mm/s. We performed 3 repeats for each cutting rates. Each individual razor blade was used for at most 6 cuts.

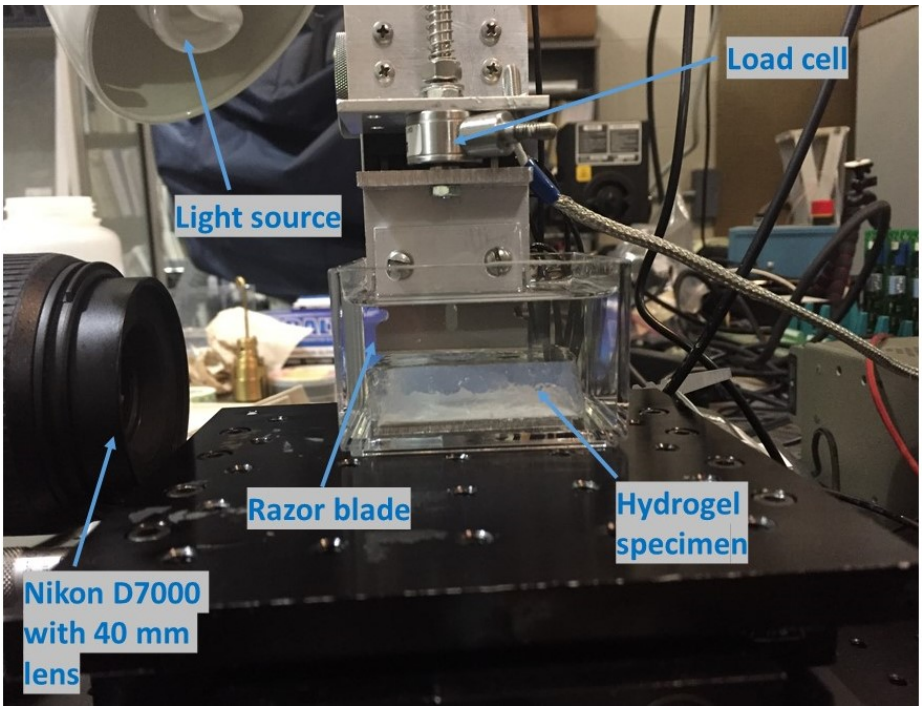

Figure A.5: Experimental Setup for cutting tests.

All the experimental results are shown in Figure A.6. It can be seen that the tests within each cutting rate are quite consistent. The cutting response is also rate dependent. For those relatively slow cutting rates from 0.1 mm/s to 1 mm/s, the material was pushed by the razor but the razor did not penetrate the surface of the specimen. For those higher cutting rates from 2 mm/s to 10 mm/s, the razor did penetrate the specimen as indicated by the force vs. displacement data. To further show the rate dependent cutting behavior, we picked one test from each individual cutting rate and plotted them in Figure A.7.

We also examined the post-cut specimen. Figure A.8 shows the specimen after being cut under 0.3 mm/s and 10 mm/s. As can be seen in Figure A.8 , the specimen

completely recovered after being cut under 0.3 mm/s and no sign of indentation was left. This is consistent with the force vs. displacement curve in Figure A.6 (b) that the razor blade did not penetrate the surface of the specimen. While the post-cut site for 10 mm/s rate clearly shows that the surface of the specimen was penetrated by the razor blade. Despite the relatively low fracture toughness under tension, this material has a relatively strong resistance to cutting. When being cut under slow loading rates, the material was pushed by the razor to a depth of almost the thickness of the specimen, without being penetrated. It should be noted that in this case, the razor was pushed down without slicing in the tangential direction. Adding a shear force changes the stress state and could lead to a different response under cutting, as discussed in [91]. For this material, based on our observation, slicing can make cutting much easier. This idea was not formally studied in this thesis, though.

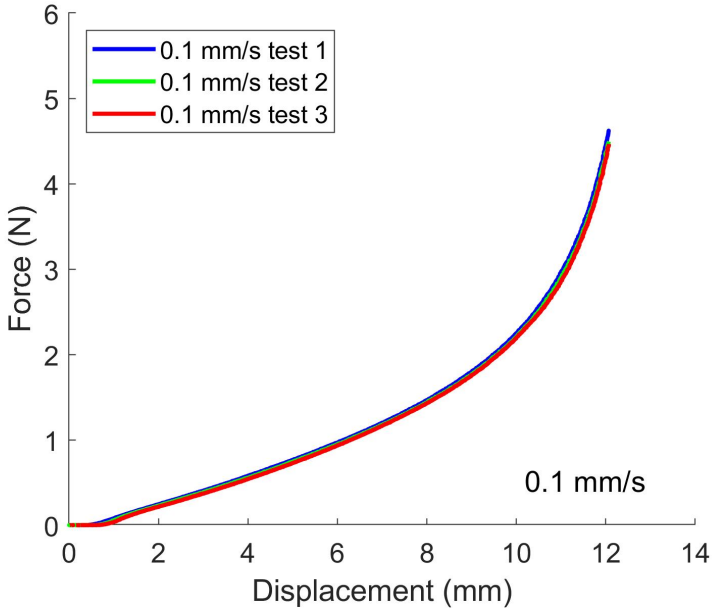
0.1 mm/s test 1
0.1 mm/s test 2
0.1 mm/s test 3
Force (N)
Displacement (mm)
0.1 mm/s
0
1
2
3
4
5
6
0
2
4
6
8
10
12
14

(a)

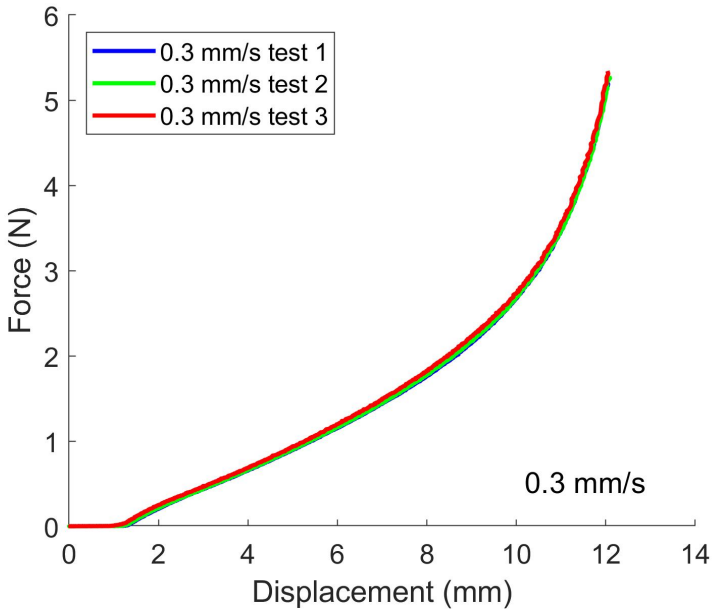
0.3 mm/s test 1
0.3 mm/s test 2
0.3 mm/s test 3
Force (N)
Displacement (mm)
0.3 mm/s
0
1
2
3
4
5
6
0
2
4
6
8
10
12
14

(b)

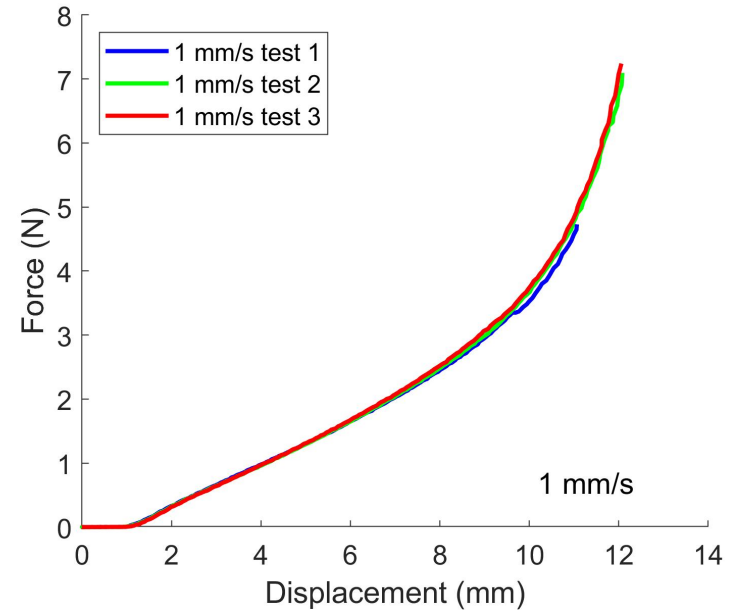
1 mm/s test 1
1 mm/s test 2
1 mm/s test 3
Force (N)
Displacement (mm)
1 mm/s
0
1
2
3
4
5
6
7
8
0
2
4
6
8
10
12
14

(c)

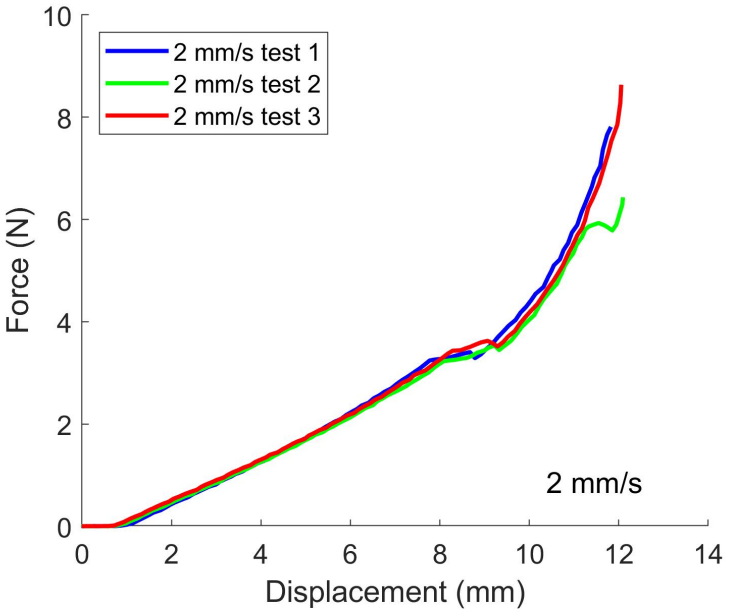
2 mm/s test 1
2 mm/s test 2
2 mm/s test 3
Force (N)
Displacement (mm)
2 mm/s
0
2
4
6
8
10
0
2
4
6
8
10
12
14

(d)

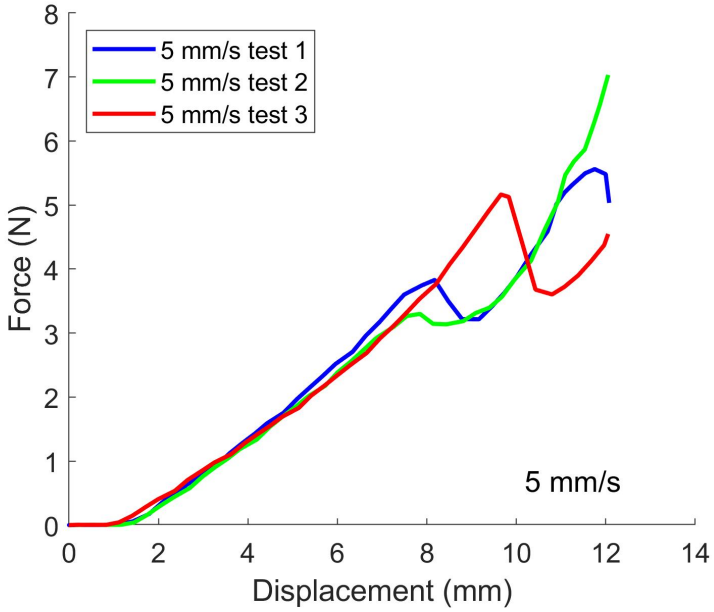

(e)

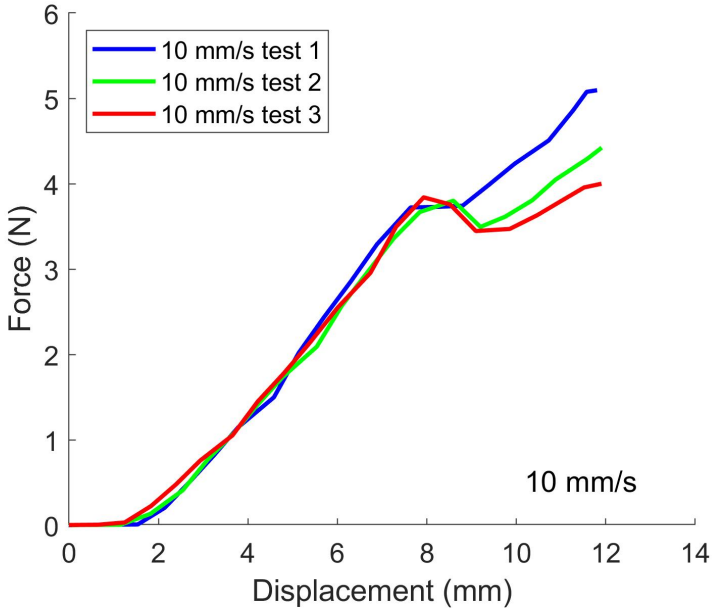

(f)

Figure A.6: Experimental results of cutting tests: (a) 0.1 mm/s (b) 0.3 mm/s (c) 1 mm/s (d) 2 mm/s (e) 5 mm/s (f) 10 mm/s

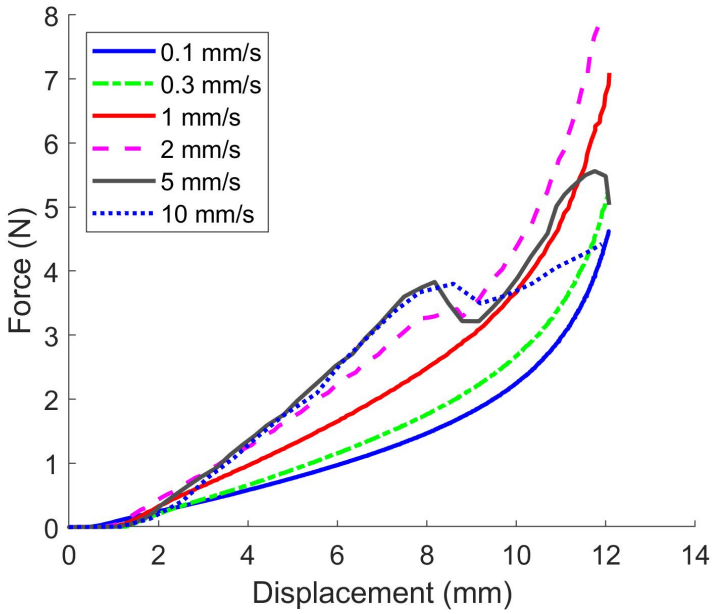

Figure A.7: Comparison between cutting tests at different rates.

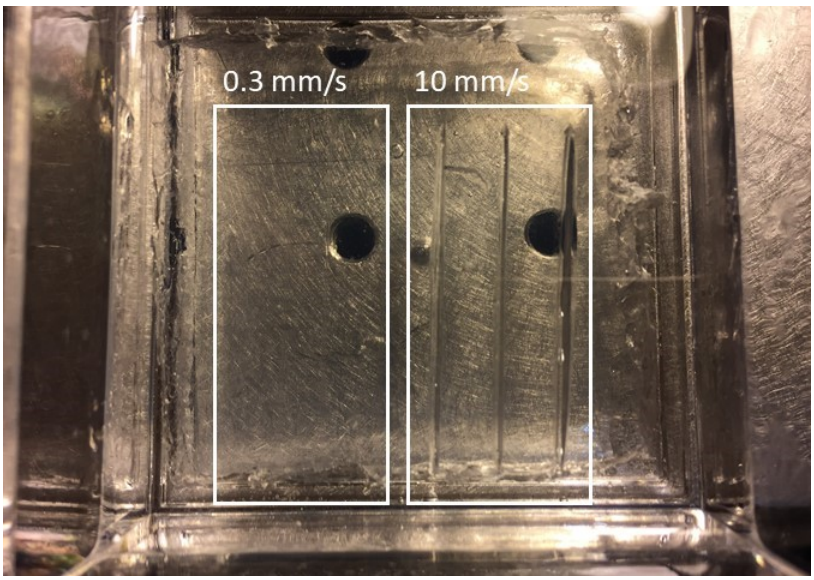

Figure A.8: A post-cut specimen

Bibliography

[1] Kuen Yong Lee and David J. Mooney. "Hydrogels for Tissue Engineering". en. In: *Chemical Reviews* 101.7 (July 2001), pp. 1869–1880. ISSN: 0009-2665, 1520-6890. DOI: 10.1021/cr000108x.

[2] Catherine K Kuo and Peter X Ma. "Ionically Crosslinked Alginate Hydrogels as Scaffolds for Tissue Engineering: Part 1. Structure, Gelation Rate and Mechanical Properties". In: *Biomaterials* 22.6 (Mar. 2001), pp. 511–521. ISSN: 0142-9612. DOI: 10.1016/S0142-9612(00)00201-5.

[3] Hyuck Joon Kwon et al. "Polyelectrolyte Hydrogels for Replacement and Regeneration of Biological Tissues". en. In: *Macromolecular Research* 22.3 (Mar. 2014), pp. 227–235. ISSN: 1598-5032, 2092-7673. DOI: 10.1007/s13233-014-2045-6.

[4] Yong Qiu and Kinam Park. "Environment-Sensitive Hydrogels for Drug Delivery". In: *Advanced Drug Delivery Reviews*. Triggering in Drug Delivery Systems 53.3 (Dec. 2001), pp. 321–339. ISSN: 0169-409X. DOI: 10.1016/S0169-409X(01)00203-4.

[5] Yuan Liu et al. "Recent developments in tough hydrogels for biomedical applications". In: *Gels* 4.2 (2018), p. 46.

[6] Kazutoshi Haraguchi and Toru Takehisa. "Nanocomposite hydrogels: a unique organic–inorganic network structure with extraordinary mechanical, optical, and swelling/de-swelling properties". In: *Advanced materials* 14.16 (2002), pp. 1120–1124.

[7] J.P. Gong et al. "Double-Network Hydrogels with Extremely High Mechanical Strength". en. In: *Advanced Materials* 15.14 (July 2003), pp. 1155–1158. ISSN: 09359648, 15214095. DOI: 10.1002/adma.200304907.

[8] Rebecca E. Webber et al. "Large Strain Hysteresis and Mullins Effect of Tough Double-Network Hydrogels". en. In: *Macromolecules* 40.8 (Apr. 2007), pp. 2919–2927. ISSN: 0024-9297, 1520-5835. DOI: 10.1021/ma062924y.

[9] Kevin J. Henderson et al. “Ionically Cross-Linked Triblock Copolymer Hydrogels with High Strength”. en. In: *Macromolecules* 43.14 (July 2010), pp. 6193–6201. ISSN: 0024-9297, 1520-5835. DOI: 10.1021/ma100963m.

[10] Jeong-Yun Sun et al. “Highly stretchable and tough hydrogels”. In: *Nature* 489.7414 (2012), p. 133.

[11] Tao Lin Sun et al. “Physical Hydrogels Composed of Polyampholytes Demonstrate High Toughness and Viscoelasticity”. en. In: *Nature Materials* 12.10 (Oct. 2013), pp. 932–937. ISSN: 1476-1122, 1476-4660. DOI: 10.1038/nmat3713.

[12] Koichi Mayumi et al. “Stress–Strain Relationship of Highly Stretchable Dual Cross-Link Gels: Separability of Strain and Time Effect”. In: *ACS Macro Letters* 2.12 (Dec. 2013), pp. 1065–1068. DOI: 10.1021/mz4005106.

[13] Rong Long et al. “Time Dependent Behavior of a Dual Cross-Link Self-Healing Gel: Theory and Experiments”. en. In: *Macromolecules* 47.20 (Oct. 2014), pp. 7243–7250. ISSN: 0024-9297, 1520-5835. DOI: 10.1021/ma501290h.

[14] Jingyi Guo et al. “Mechanics of a Dual Cross-Link Gel with Dynamic Bonds: Steady State Kinetics and Large Deformation Effects”. en. In: *Macromolecules* 49.9 (May 2016), pp. 3497–3507. ISSN: 0024-9297, 1520-5835. DOI: 10.1021/acs.macromol.6b00421.

[15] Rong Long et al. “Rheology of a Dual Crosslink Self-Healing Gel: Theory and Measurement Using Parallel-Plate Torsional Rheometry”. In: *Journal of Rheology* 59.3 (Mar. 2015), pp. 643–665. ISSN: 0148-6055. DOI: 10.1122/1.4915275.

[16] Jingyi Guo et al. “Fracture Mechanics of a Self-Healing Hydrogel with Covalent and Physical Crosslinks: A Numerical Study”. en. In: *Journal of the Mechanics and Physics of Solids* (Mar. 2018). ISSN: 00225096. DOI: 10.1016/j.jmps.2018.03.009.

[17] Jingyi Guo et al. “The stress field near the tip of a plane stress crack in a gel consisting of chemical and physical cross-links”. In: (2019).

[18] Tao Lin Sun et al. “Bulk Energy Dissipation Mechanism for the Fracture of Tough and Self-Healing Hydrogels”. In: *Macromolecules* 50.7 (Apr. 2017), pp. 2923–2931. ISSN: 0024-9297. DOI: 10.1021/acs.macromol.7b00162.

[19] Mincong Liu et al. “Time-Temperature Equivalence in a PVA Dual Cross-Link Self-Healing Hydrogel”. In: *Journal of Rheology* 62.4 (July 2018), pp. 991–1000. ISSN: 0148-6055. DOI: 10.1122/1.5029466.

[20] H.J. Kwon et al. “Application of Digital Image Correlation Method to Biogel”. en. In: *Polymer Engineering & Science* 50.8 (Aug. 2010), pp. 1585–1593. ISSN: 00323888. DOI: 10.1002/pen.21636.

[21] Aviad Sasson et al. “Hyperelastic Mechanical Behavior of Chitosan Hydrogels for Nucleus Pulposus Replacement—Experimental Testing and Constitutive Modeling”. In: *Journal of the Mechanical Behavior of Biomedical Materials* 8 (Apr. 2012), pp. 143–153. ISSN: 1751-6161. DOI: 10.1016/j.jmbbm.2011.12.008.

[22] Alexander Leibinger et al. “Soft Tissue Phantoms for Realistic Needle Insertion: A Comparative Study”. en. In: *Annals of Biomedical Engineering* 44.8 (Aug. 2016), pp. 2442–2452. ISSN: 1573-9686. DOI: 10.1007/s10439-015-1523-0.

[23] Y. Hong et al. “Localized Tissue Surrogate Deformation Due to Controlled Single Bubble Cavitation”. en. In: *Experimental Mechanics* 56.1 (Jan. 2016), pp. 97–109. ISSN: 1741-2765. DOI: 10.1007/s11340-015-0024-2.

[24] Kyle Christensen et al. “Effects of Printing-Induced Interfaces on Localized Strain within 3D Printed Hydrogel Structures”. In: *Materials Science and Engineering: C* 89 (Aug. 2018), pp. 65–74. ISSN: 0928-4931. DOI: 10.1016/j.msec.2018.03.014.

[25] Céline Samira Wyss et al. “Cyclic Loading of a Cellulose/Hydrogel Composite Increases Its Fracture Strength”. In: *Extreme Mechanics Letters* 24 (Oct. 2018), pp. 66–74. ISSN: 2352-4316. DOI: 10.1016/j.eml.2018.09.002.

[26] M Liu et al. “Application of Digital Image Correlation (DIC) to the Measurement of Strain Concentration of a PVA Dual-Crosslink Hydrogel Under Large Deformation”. In: *Experimental Mechanics* (2019), pp. 1–12.

[27] T. Baumberger and O. Ronsin. “From Thermally Activated to Viscosity Controlled Fracture of Biopolymer Hydrogels”. en. In: *The Journal of Chemical Physics* 130.6 (Feb. 2009), p. 061102. ISSN: 0021-9606, 1089-7690. DOI: 10.1063/1.3078267.

[28] Koichi Mayumi et al. “Fracture of Dual Crosslink Gels with Permanent and Transient Crosslinks”. en. In: *Extreme Mechanics Letters* 6 (Mar. 2016), pp. 52–59. ISSN: 23524316. DOI: 10.1016/j.eml.2015.12.002.

[29] Sadia Nazneen Karobi et al. “Creep Behavior and Delayed Fracture of Tough Polyampholyte Hydrogels by Tensile Test”. en. In: *Macromolecules* 49.15 (Aug. 2016), pp. 5630–5636. ISSN: 0024-9297, 1520-5835. DOI: 10.1021/acs.macromol.6b01016.

[30] Satish Mishra et al. “Investigation of Failure Behavior of a Thermoplastic Elastomer Gel”. en. In: *Soft Matter* 14.39 (2018), pp. 7958–7969. ISSN: 1744-683X, 1744-6848. DOI: 10.1039/C8SM01397G.

[31] Jingda Tang et al. “Fatigue Fracture of Hydrogels”. In: *Extreme Mechanics Letters*. Filling Gaps in Material Property Space: IUTAM Symposium 10 (Jan. 2017), pp. 24–31. ISSN: 2352-4316. DOI: 10.1016/j.eml.2016.09.010.

[32] Ruobing Bai et al. “Fatigue Fracture of Tough Hydrogels”. en. In: *Extreme Mechanics Letters* 15 (Sept. 2017), pp. 91–96. ISSN: 23524316. DOI: 10.1016/j.eml.2017.07.002.

[33] Ruobing Bai et al. “Fatigue Fracture of Self-Recovery Hydrogels”. en. In: *ACS Macro Letters* 7.3 (Mar. 2018), pp. 312–317. ISSN: 2161-1653, 2161-1653. DOI: 10.1021/acsmacrolett.8b00045.

[34] Mincong Liu et al. “Crack tip stress based kinetic fracture model of a PVA dual-crosslink hydrogel”. In: *Extreme Mechanics Letters* 29 (2019), p. 100457.

[35] https://www.tek.com/keithley-kickstart. Accessed: 2019-05-30.

[36] John Dealy and Don Plazek. “Time-Temperature Superposition -A Users Guide”. In: *Rheology Bulletin* 78.2 (2009), pp. 16–31.

[37] Ray K. Schultz and Raymond R. Myers. “The Chemorheology of Poly(Vinyl Alcohol)-Borate Gels”. In: *Macromolecules* 2 (May 1969), pp. 281–285. DOI: 10.1021/ma60009a014.

[38] Tetsuharu Narita and Tsutomu Indei. “Microrheological Study of Physical Gelation in Living Polymeric Networks”. In: *Macromolecules* 49.12 (June 2016), pp. 4634–4646. ISSN: 0024-9297. DOI: 10.1021/acs.macromol.6b00745.

[39] Bing Pan et al. “Two-Dimensional Digital Image Correlation for in-Plane Displacement and Strain Measurement: A Review”. en. In: *Measurement Science and Technology* 20.6 (June 2009), p. 062001. ISSN: 0957-0233, 1361-6501. DOI: 10.1088/0957-0233/20/6/062001.

[40] Sze-Wei Khoo, Saravanan Karuppanan, and Ching-Seong Tan. “A Review of Surface Deformation and Strain Measurement Using Two-Dimensional Digital Image Correlation”. en. In: *Metrology and Measurement Systems* 23.3 (Sept. 2016), pp. 461–480. ISSN: 2300-1941. DOI: 10.1515/mms-2016-0028.

[41] Michael A Sutton, Jean Jose Orteu, and Hubert Schreier. *Image correlation for shape, motion and deformation measurements: basic concepts, theory and applications*. Springer Science & Business Media, 2009.

[42] H. Haddadi and S. Belhabib. “Use of Rigid-Body Motion for the Investigation and Estimation of the Measurement Errors Related to Digital Image Correlation Technique”. en. In: *Optics and Lasers in Engineering* 46.2 (Feb. 2008), pp. 185–196. ISSN: 01438166. DOI: 10.1016/j.optlaseng.2007.05.008.

[43] Bing Pan et al. “Systematic Errors in Two-Dimensional Digital Image Correlation Due to Lens Distortion”. en. In: *Optics and Lasers in Engineering* 51.2 (Feb. 2013), pp. 140–147. ISSN: 01438166. DOI: 10.1016/j.optlaseng.2012.08.012.

[44] M.A. Sutton et al. "The Effect of Out-of-Plane Motion on 2D and 3D Digital Image Correlation Measurements". en. In: *Optics and Lasers in Engineering* 46.10 (Oct. 2008), pp. 746–757. ISSN: 01438166. DOI: 10.1016/j.optlaseng.2008.05.005.

[45] M. Jerabek, Z. Major, and R.W. Lang. "Strain Determination of Polymeric Materials Using Digital Image Correlation". en. In: *Polymer Testing* 29.3 (May 2010), pp. 407–416. ISSN: 01429418. DOI: 10.1016/j.polymertesting.2010.01.005.

[46] Neil A. Hoult et al. "Experimental Accuracy of Two Dimensional Strain Measurements Using Digital Image Correlation". en. In: *Engineering Structures* 46 (Jan. 2013), pp. 718–726. ISSN: 01410296. DOI: 10.1016/j.engstruct.2012.08.018.

[47] C. P. Goh et al. "Single-Step Scanner-Based Digital Image Correlation (SB-DIC) Method for Large Deformation Mapping in Rubber". In: *Optics and Lasers in Engineering* 88 (Jan. 2017), pp. 167–177. ISSN: 0143-8166. DOI: 10.1016/j.optlaseng.2016.08.011.

[48] Kevin M. Moerman et al. "Digital Image Correlation and Finite Element Modelling as a Method to Determine Mechanical Properties of Human Soft Tissue in Vivo". In: *Journal of Biomechanics* 42.8 (May 2009), pp. 1150–1153. ISSN: 0021-9290. DOI: 10.1016/j.jbiomech.2009.02.016.

[49] Caleb R. Horst et al. "Measuring the Modulus of Silicone Hydrogel Contact Lenses:" en. In: *Optometry and Vision Science* 89.10 (Oct. 2012), pp. 1468–1476. ISSN: 1040-5488. DOI: 10.1097/OPX.0b013e3182691454.

[50] Michael PM Dicker et al. "Modelling and Analysis of pH Responsive Hydrogels for the Development of Biomimetic Photo-Actuating Structures". en. In: *MRS Proceedings* 1718 (2015). ISSN: 1946-4274. DOI: 10.1557/opl.2015.20.

[51] G. Subhash et al. "Concentration Dependence of Tensile Behavior in Agarose Gel Using Digital Image Correlation". en. In: *Experimental Mechanics* 51.2 (Feb. 2011), pp. 255–262. ISSN: 0014-4851, 1741-2765. DOI: 10.1007/s11340-010-9354-2.

[52] Kimberley Mac Donald and Guruswami Ravichandran. "An Experimental Method to Induce and Measure Crack Propagation in Brittle Polymers with Heterogeneities". en. In: *Fracture, Fatigue, Failure and Damage Evolution, Volume 6*. Ed. by Jay Carroll et al. Conference Proceedings of the Society for Experimental Mechanics Series. Springer International Publishing, 2019, pp. 21–23. ISBN: 978-3-319-95879-8.

[53] Awatef M. Alshehri et al. "Magnetic Nanoparticle-Loaded Alginate Beads for Local Micro-Actuation of in Vitro Tissue Constructs". In: *Colloids and Surfaces B: Biointerfaces* 159 (Nov. 2017), pp. 945–955. ISSN: 0927-7765. DOI: 10.1016/j.colsurfb.2017.08.062.

[54] A. J. Skulborstad et al. “Polarized Image Correlation for Large Deformation Fiber Kinematics”. en. In: *Experimental Mechanics* 53.8 (Oct. 2013), pp. 1405–1413. ISSN: 1741-2765. DOI: 10.1007/s11340-013-9751-4.

[55] A Hijazi, A Friedl, and C J Kähler. “Influence of Camera’s Optical Axis Non-Perpendicularity on Measurement Accuracy of Two-Dimensional Digital Image Correlation”. en. In: 5.4 (2011), p. 10.

[56] J. Blaber, B. Adair, and A. Antoniou. “Ncorr: Open-Source 2D Digital Image Correlation Matlab Software”. en. In: *Experimental Mechanics* 55.6 (July 2015), pp. 1105–1122. ISSN: 0014-4851, 1741-2765. DOI: 10.1007/s11340-015-0009-1.

[57] Bing Pan. “Reliability-Guided Digital Image Correlation for Image Deformation Measurement”. en. In: *Applied Optics* 48.8 (Mar. 2009), p. 1535. ISSN: 0003-6935, 1539-4522. DOI: 10.1364/AO.48.001535.

[58] Bing Pan, Wu Dafang, and Xia Yong. “Incremental Calculation for Large Deformation Measurement Using Reliability-Guided Digital Image Correlation”. en. In: *Optics and Lasers in Engineering* 50.4 (Apr. 2012), pp. 586–592. ISSN: 01438166. DOI: 10.1016/j.optlaseng.2011.05.005.

[59] Y.L. Dong and B. Pan. “A Review of Speckle Pattern Fabrication and Assessment for Digital Image Correlation”. en. In: *Experimental Mechanics* 57.8 (Oct. 2017), pp. 1161–1181. ISSN: 1741-2765. DOI: 10.1007/s11340-017-0283-1.

[60] G. Crammond, S.W. Boyd, and J.M. Dulieu-Barton. “Speckle Pattern Quality Assessment for Digital Image Correlation”. en. In: *Optics and Lasers in Engineering* 51.12 (Dec. 2013), pp. 1368–1378. ISSN: 01438166. DOI: 10.1016/j.optlaseng.2013.03.014.

[61] Tao Hua et al. “Evaluation of the Quality of a Speckle Pattern in the Digital Image Correlation Method by Mean Subset Fluctuation”. In: *Optics & Laser Technology* 43.1 (Feb. 2011), pp. 9–13. ISSN: 0030-3992. DOI: 10.1016/j.optlastec.2010.04.010.

[62] D. Lecompte et al. “Quality Assessment of Speckle Patterns for Digital Image Correlation”. en. In: *Optics and Lasers in Engineering* 44.11 (Nov. 2006), pp. 1132–1145. ISSN: 01438166. DOI: 10.1016/j.optlaseng.2005.10.004.

[63] Jihyuk Park et al. “Assessment of Speckle-Pattern Quality in Digital Image Correlation Based on Gray Intensity and Speckle Morphology”. In: *Optics and Lasers in Engineering* 91 (Apr. 2017), pp. 62–72. ISSN: 0143-8166. DOI: 10.1016/j.optlaseng.2016.11.001.

[64] Bing Pan, Zixing Lu, and Huimin Xie. “Mean Intensity Gradient: An Effective Global Parameter for Quality Assessment of the Speckle Patterns Used in Digital Image Correlation”. In: *Optics and Lasers in Engineering* 48.4 (Apr. 2010), pp. 469–477. ISSN: 0143-8166. DOI: 10.1016/j.optlaseng.2009.08.010.

[65] Bing Pan et al. “Study on Subset Size Selection in Digital Image Correlation for Speckle Patterns”. en. In: *Optics Express* 16.10 (May 2008), p. 7037. ISSN: 1094-4087. DOI: 10.1364/OE.16.007037.

[66] Sun Yaofeng and John H. L. Pang. “Study of Optimal Subset Size in Digital Image Correlation of Speckle Pattern Images”. In: *Optics and Lasers in Engineering* 45.9 (Sept. 2007), pp. 967–974. ISSN: 0143-8166. DOI: 10.1016/j.optlaseng.2007.01.012.

[67] T. Goldman Boué et al. “Failing Softly: A Fracture Theory of Highly-Deformable Materials”. en. In: *Soft Matter* 11.19 (2015), pp. 3812–3821. ISSN: 1744-683X, 1744-6848. DOI: 10.1039/C5SM00496A.

[68] F Pizzocolo, JM Huyghe, and K Ito. “Mode I crack propagation in hydrogels is step wise”. In: *Engineering Fracture Mechanics* 97 (2013), pp. 72–79.

[69] Feng Luo et al. “Crack blunting and advancing behaviors of tough and self-healing polyampholyte hydrogel”. In: *Macromolecules* 47.17 (2014), pp. 6037–6046.

[70] P. Lava et al. “Impact of Lens Distortions on Strain Measurements Obtained with 2D Digital Image Correlation”. en. In: *Optics and Lasers in Engineering* 51.5 (May 2013), pp. 576–584. ISSN: 01438166. DOI: 10.1016/j.optlaseng.2012.12.009.

[71] Satoru Yoneyama et al. “Lens distortion correction for digital image correlation by measuring rigid body displacement”. In: *Optical engineering* 45.2 (2006), p. 023602.

[72] Michael A Sutton and Christopher McFadden. “Development of a methodology for non-contacting strain measurements in fluid environments using computer vision”. In: *Optics and Lasers in Engineering* 32.4 (1999), pp. 367–377.

[73] Rong Long and Chung-Yuen Hui. “Fracture Toughness of Hydrogels: Measurement and Interpretation”. en. In: *Soft Matter* 12.39 (2016), pp. 8069–8086. ISSN: 1744-683X, 1744-6848. DOI: 10.1039/C6SM01694D.

[74] Yuan Qi et al. “Mapping the nonlinear crack tip deformation field in soft elastomer with a particle tracking method”. In: *Journal of the Mechanics and Physics of Solids* 125 (2019), pp. 326–346.

[75] Maxime Lefranc and Elisabeth Bouchaud. “Mode I Fracture of a Biopolymer Gel: Rate-Dependent Dissipation and Large Deformations Disentangled”. In: *Extreme Mechanics Letters* 1 (Dec. 2014), pp. 97–103. ISSN: 2352-4316. DOI: 10.1016/j.eml.2014.11.004.

[76] Wenlei Zhang et al. “Fatigue of Double-Network Hydrogels”. en. In: *Engineering Fracture Mechanics* 187 (Jan. 2018), pp. 74–93. ISSN: 00137944. DOI: 10.1016/j.engfracmech.2017.10.018.

[77] Ni Zhang et al. “Effects of Temperature on the Fracture and Fatigue Damage of Temperature Sensitive Hydrogels”. en. In: *RSC Advances* 8.54 (Aug. 2018), pp. 31048–31054. ISSN: 2046-2069. DOI: 10.1039/C8RA06518G.

[78] G. J. Lake and A. G. Thomas. “The Strength of Highly Elastic Materials”. en. In: *Proceedings of the royal society A* 300.1460 (Aug. 1967), pp. 108–119.

[79] Jun Cui et al. “Mechanical Properties of End-Linked PEG/PDMS Hydrogels”. en. In: *Macromolecules* 45.15 (Aug. 2012), pp. 6104–6110. ISSN: 0024-9297, 1520-5835. DOI: 10.1021/ma300593g.

[80] Arthur Tobolsky and Henry Eyring. “Mechanical Properties of Polymeric Materials”. In: *The Journal of Chemical Physics* 11.3 (Mar. 1943), pp. 125–134. ISSN: 0021-9606. DOI: 10.1063/1.1723812.

[81] Bernard D. Coleman. “Time Dependence of Mechanical Breakdown Phenomena”. en. In: *Journal of Applied Physics* 27.8 (Aug. 1956), pp. 862–866. ISSN: 0021-8979, 1089-7550. DOI: 10.1063/1.1722504.

[82] S. N. Zhurkov and V. E. Korsukov. “Atomic Mechanism of Fracture of Solid Polymers”. en. In: *Journal of Polymer Science: Polymer Physics Edition* 12.2 (Feb. 1974), pp. 385–398. ISSN: 00981273, 15429385. DOI: 10.1002/pol.1974.180120211.

[83] C.B. Henderson, P.H. Graham, and C.N. Robinson. “A Comparison of Reaction Rate Models for the Fracture of Solids”. en. In: *International Journal of Fracture Mechanics* 6.1 (Mar. 1970). ISSN: 0020-7268, 1573-2673. DOI: 10.1007/BF00183657.

[84] Loïc Vanel et al. “Time-Dependent Rupture and Slow Crack Growth: Elastic and Viscoplastic Dynamics”. en. In: *Journal of Physics D: Applied Physics* 42.21 (Nov. 2009), p. 214007. ISSN: 0022-3727, 1361-6463. DOI: 10.1088/0022-3727/42/21/214007.

[85] Chung-Yuen Hui et al. “Failure of Elastomeric Polymers Due to Rate Dependent Bond Rupture”. en. In: *Langmuir* 20.14 (July 2004), pp. 6052–6064. ISSN: 0743-7463, 1520-5827. DOI: 10.1021/la0356607.

[86] Andrew C Hansen. “A Rate Dependent Kinetic Theory of Fracture for Polymers”. en. In: *International Journal of Fracture* 44.3 (Aug. 1990), pp. 221–231.

[87] Paulina J. Skrzeszewska et al. “Fracture and Self-Healing in a Well-Defined Self-Assembled Polymer Network”. en. In: *Macromolecules* 43.7 (Apr. 2010), pp. 3542–3548. ISSN: 0024-9297, 1520-5835. DOI: 10.1021/ma1000173.

[88] Rong Long and Chung-Yuen Hui. “Crack Tip Fields in Soft Elastic Solids Subjected to Large Quasi-Static Deformation — A Review”. en. In: *Extreme Mechanics Letters* 4 (Sept. 2015), pp. 131–155. ISSN: 23524316. DOI: 10.1016/j.eml.2015.06.002.

[89] D. J. Dijkstra, J. C. M. Torfs, and A. J. Pennings. "Temperature-Dependent Fracture Mechanisms in Ultra-High Strength Polyethylene Fibers". en. In: *Colloid & Polymer Science* 267.10 (Oct. 1989), pp. 866–875. ISSN: 0303-402X, 1435-1536. DOI: 10.1007/BF01410334.

[90] H. H. Kausch von Schmeling, S. R. Moghe, and C. C. Hsiao. "Influence of Reforming Processes on the Fracture Strength of Solids". en. In: *Journal of Applied Physics* 38.1 (Jan. 1967), pp. 201–204. ISSN: 0021-8979, 1089-7550. DOI: 10.1063/1.1708955.

[91] E Reyssat et al. "Slicing softly with shear". In: *Physical review letters* 109.24 (2012), p. 244301.